BAM
Bundesanstalt für
Materialforschung
und -prüfung

Sicherheit in Technik und Chemie

Oded Sobol

Hydrogen Assisted Cracking and Transport Studied by ToF-SIMS and Data Fusion with HR-SEM

BAM-Dissertationsreihe | Band 160

M.Sc. Oded Sobol

Hydrogen Assisted Cracking and Transport Studied by ToF-SIMS and Data Fusion with HR-SEM

BAM-Dissertationsreihe · Band 160
Berlin 2018

Die vorliegende Arbeit entstand an der Bundesanstalt für Materialforschung und -prüfung (BAM).

Impressum

Hydrogen Assisted Cracking and Transport Studied by ToF-SIMS and Data Fusion with HR-SEM

2018

Herausgeber:
Bundesanstalt für Materialforschung und -prüfung (BAM)
Unter den Eichen 87
12205 Berlin
Telefon: +49 30 8104-0
Telefax: +49 30 8104-72222
E-Mail: info@bam.de
Internet: www.bam.de

Layout: BAM-Referat Z.8

ISSN 1613-4249

Die BAM ist eine Bundesoberbehörde im Geschäftsbereich
des Bundesministeriums für Wirtschaft und Energie.

Hydrogen Assisted Cracking and Transport Studied by ToF-SIMS and Data Fusion with HR-SEM

Dissertation

zur Erlangung des akademischen Grades

Doktoringenieur

(Dr.-Ing.)

von M.Sc. Oded Sobol

geb. am 27.11.1983 in Haifa

genehmigt durch die Fakultät für Maschinenbau

der Otto-von-Guericke-Universität Magdeburg

Gutachter:

Prof. Dr.-Ing. habil. Thomas Böllinghaus

Prof. Dr. rer. nat. Wolfgang Unger

Prof. Dan Eliezer

Promotionskolloquium am 14.02.2018

Abstract

For almost 150 years it is known that hydrogen has a deleterious effect on the mechanical properties of metallic components. Nowadays, the problem of hydrogen assisted degradation is highly relevant in energy related fields due to the massive use of steel as a structural component in these applications and its sensitivity to hydrogen. Since the discovery of hydrogen assisted cracking (HAC), researchers studied intensively and suggested possible explanations and mechanisms in order to define how hydrogen is affecting the material. In general, it is considered that hydrogen changes the mechanical properties more in terms of ductility (deformation capacities) than in strength (load capacities). Hydrogen concentration is one of three crucial factors in the degradation process, together with the microstructure of the material and the internal/external mechanical load. The relatively high concentration of hydrogen resulting in this loss of ductility can originate during production or before service (e.g. welding processes) and during service (i.e. catholically protected systems to eliminate corrosion processes in sour environments).

In parallel to the theoretical work, tremendous efforts were, and are still, invested in searching for a proper method to elucidate, map and quantify the hydrogen in the microstructure, which is the basis for this work. For steels, the focus is mainly on the observations of diffusion processes and the interaction of hydrogen with the microstructure in regions with high local stresses/strains (for example around evolving cracks). The challenge for reaching this goal arises from the fact that accurate indication of hydrogen by means of position, unlike heavier atoms, can be made only by mass spectrometry or by interaction with another element (e.g. silver decoration, special coating and resonant nuclear reaction by nitrogen). In addition to this, the difficulty recording the hydrogen behavior while it rapidly diffuses through the material, leaving only the unpredicted failure, should be taken into account.

Although using powerful characterization methods, models and computational simulations, the key to defining the mechanisms behind HAC is still under debate and not fully understood. The relationship between material and hydrogen is determined by three factors, i.e., the material structure and microstructure – determining the physical properties, the mechanical load applied on the material and the hydrogen concentration. It is well known that in order to have a complete definition of HAC these three factors must be examined locally with the minimal scale and the maximal resolution reachable. The major gap is the lack in such a characterization method or a technique by which one has the

ability to detect and observe the hydrogen in the metallic microstructure. The commonly used techniques nowadays are capable of characterization of the microstructure without the ability to observe the hydrogen distribution. Global hydrogen concentration and localized hydrogen observation are possible by some techniques which are incapable of indicating a change in the structure or microstructure therefore a comprehensive overview can be gained only by combining several methods.

In the presented research, secondary ion mass spectrometry (SIMS) was adopted as the main tool to detect and locally map the hydrogen distribution in two types of duplex stainless steel grades: EN 1.4462 (standard 2205 duplex stainless steel) and EN 1.4162 (2101 lean duplex stainless steel). The term duplex stainless steel (DSS) refers to the austenitic-ferritic microstructure of the steel where the combination of physical and mechanical properties of the two phases is achieved. The DSS was selected as a case study for this work due to the wide use of this grade in many energy applications and the lack of knowledge on hydrogen behavior in two-phase containing microstructures. ToF-SIMS was exploited in-situ and ex-situ in three experimental approaches during or following an electrochemical charging procedure. This type of hydrogen charging was selected as it simulated a procedure of cathodic protection of most sub-water oil and gas extraction and delivery systems. The experimental procedures were:

1. Ex-situ charging followed by ToF-SIMS imaging for basic understanding of hydrogen distribution.
2. Ex-situ charging followed by in-situ mechanical loading to obtain information on hydrogen behavior around a propagating crack.
3. In-situ permeation of hydrogen through a steel membrane inside the ToF-SIMS to obtain information on diffusion behavior of hydrogen in a two-phase microstructure.

The comprehensive view of the effect of hydrogen on steel was gained by using supplementary methods, such as high resolution scanning electron microscopy (HR-SEM), focused ion beam (FIB) and electron back-scattered diffraction (EBSD).

The state of the art in this work lies in applying both: in-situ experimental approaches and data treatment of the ToF-SIMS raw data. The data treatment includes the combination of data from several sources (data fusion).

The results for the ex-situ charging followed by static sample imaging and data fusion showed that when the analyzed surface is directly exposed to the electrolyte the degradation is pronounced differently in the ferrite, austenite and interface. The degradation

mechanisms in the ferrite and austenite were reflected by the formation of cracks on the surface of both, where a high concentration of hydrogen was obtained. This result supports the assumption that hydrogen is attracted to highly deformed regions. The advantage of using in-situ charging/permeation in comparison to ex-situ charging is that the effect of hydrogen on the ferrite and austenite phases when the hydrogen is evolving from within the microstructure is realized, in comparison to when the analyzed surface is initially exposed directly to the electrolyte. In both experiments the ferrite was observed as a fast diffusion path for the hydrogen. The faster diffusion of hydrogen through the ferrite is expected due to the higher diffusion coefficient, however, a direct proof for the diffusion sequence in this scale was never shown.

Most significant results were achieved by the ‘core’ experiments of this research. These experiments included the design of a novel dynamic mechanical loading device to apply an external load during SIMS imaging of a hydrogen precharged-notched sample. For the first time it was shown that plastic deformation induced by applying a mechanical load is resulting in a redistribution of hydrogen locally around the notch

Acknowledgments

I am dedicating this work to my adorable family. My one and only brother, Ohad, for being with me every step of the way from the moment I was born, for helping me in every decision, for always supporting me and for being my closest friend. To my parents, for the endless love they gave us, the honesty, education and tolerance. To my mom, Yvonne, who keeps taking care to make her dreams come true only by making her children's dreams come true, for being our lioness. Finally, to my dad, Saul, who passed away just when I started this incredible journey in the academic world, but is treasured in my heart every moment.

I would like to thank my supervisors Prof. Thomas Böllinghaus, Prof. Dan Eliezer and Prof. Wolfgang Unger for all their generous support, guidance, advice and constant encouragement throughout my research. I am very grateful to Prof. Karl-Heinrich Grote and Dr. Reinhard Fietz for their part in the examination process and the defense committee.

I am very thankful for the assistance of all the people from Departments 6 and 9. To Jeanette Pannicke and Manuela Fochler for their incredible assistance with administrative tasks. To Dr. Tobias Mente, Dr. Michael Rhode, Dr. Gerald Holzlechner and Mr. Thomas Wirth for sharing their infinite knowledge with me, always being there to help me with every problem I had and being so patient with my questions. To the greatest colleagues I had the chance to spend time with: Andreas Lippitz, Jörg Radnik, Dan Hodoroaba, Thomas Schaupp, Jörg Steger, Dirk Schröpfer, Alp Taparli, Beate Pfretzschner, Enrico Steppan, Anja Hermann, Marit Kjaervik, Thomas Heinrich, Markus Rennhak, Volker Hirthammer, Thomas Titscher, Peter Otto, Sebastian Zorn and Philip Huschke.

I would like to express my deep appreciation to Michael, Tobias and Gerald together with Steve Werner, Andreas Röhsler, Maren Erdmann, Roberto Souza, Maria Madigan, Maximillian Thomas, Thora Falkenreck, Ben Steffens, Vitaliy Kindrachuk, Daniel Werner and Lena Barnefske for the endless support, for taking care of me and especially for making sure that I'm starting and finishing my day with a smile, for being my best friends.

Last but not least I would like to thank Franka Straub who showed me the way after building the foundation for this research, for helping in my first steps of my Ph.D.

"The wings are only for decoration, the reason we are calling them angels is because of their good hearts."

Berlin, February 2018

Contents

Abstract V

Acknowledgments IX

1 Introduction 1

2 Literature survey 5

2.1 Stainless steels and duplex stainless steels 5

2.2 Microstructure, properties and production of duplex stainless steels 8

2.3 Hydrogen failure cases in duplex stainless steels 19

2.3.1 Cracking of cold worked pipe 19

2.3.2 Cracking in offshore production piping 20

2.3.3 Cracking of seam welded pipes 21

2.4 Hydrogen assisted cracking and degradation of steels 22

2.4.1 Hydrogen adsorption and absorption 24

2.4.2 Hydrogen diffusion and mobility 25

2.4.3 Hydrogen trapping 29

2.4.4 Hydrogen assisted cracking (HAC) 30

2.4.5 Hydrogen assisted cracking mechanisms 33

2.4.5.1 Adsorption induced dislocation emission (AIDE) 34

2.4.5.2 Hydrogen enhanced de-cohesion (HEDE) 35

2.4.5.3 Hydrogen enhanced localized plasticity (HELP) 35

2.4.5.4 High hydrogen pressure bubble or void 36

2.4.5.5 Hydrogen- and strain-induced phase transformation 37

2.4.5.6 Hydrogen induced reduction in surface energy (Adsorption theory) 38

2.4.5.7 Hydride theory 39

2.5 Hydrogen isotopes – properties and uses 40

2.6 Methods for characterization of hydrogen related degradation (macro- quantitative and microscale methods) 44

2.6.1 Conventional macroscale quantitative methods 44

2.6.2 In-direct observations of hydrogen assisted cracking 45

2.6.3 Direct observations and mapping of hydrogen distribution – hydrogen sensitive methods 49

2.6.4 Direct observations and mapping of hydrogen distribution by Time-of-Flight Secondary Ion Mass Spectrometry 53

3 Objectives of the study 59

3.1 Statement of the problem 59

3.2 Special objectives 61

4 Experimental 65
4.1 Tested materials – composition and state 65
4.2 Detection and analysis 67
4.2.1 Time-of-Flight Secondary ion mass spectrometry (ToF-SIMS) 67
4.2.1.1 Modes of operation 68
4.2.1.2 Sputtering ions for surface contamination removal and ion yield enhancement (dual gun) 71
4.2.2 Application specific sample holders and sample preparation 74
4.2.2.1 Ex-situ – static analyses 74
4.2.2.2 In-situ –mechanical loading experiments 76
4.2.2.3 In-situ – deuterium permeation experiments 80
4.2.3 Scanning electron microscopy (SEM) 81
4.2.4 Electron back-scattered diffraction (EBSD) 83
4.2.5 Focus ion beam milling (FIB) 84
4.3 Procedures 86
4.3.1 External deuterium cathodic charging 86
4.3.2 ToF-SIMS experimental steps and mass interpretation 88
4.3.2.1 Ex-situ charged samples 88
4.3.2.2 In-situ mechanical loading 90
4.3.2.3 In-situ permeation experiments 93
4.3.3 Data treatment and data fusion 95
4.3.3.1 Multivariate data analysis (MVA) and principal component analysis (PCA) 95
4.3.4 Data Fusion 98

5 Results and discussion 101
5.1 Ex-situ static experiments 101
5.1.1 Standard duplex 2205 101
5.1.1.1 Deuterium distribution in ferrite and austenite 101
5.1.1.2 Deuterium induced twinning and cracking in the ferrite 102
5.1.1.3 Deuterium induced twinning, phase transformation and cracking in the austenite 105
5.1.2 Lean duplex 2101 111
5.2 In-situ permeation experiments 118
5.3 In-situ mechanical loading experiments 125

6 Conclusions 131

7 Perspectives 135

8 Abbreviations 137

9 List of figures 139

10 List of tables **146**

11 References **147**

List of Publications **163**

Curriculum Vitae **164**

1 Introduction

The change in the physical properties of steels by exposure to acidic solutions was first discovered by Johnson[1] in 1874. In his work the change in mechanical properties of iron samples were examined after embedding the samples in different concentrations of hydrochloric and sulphuric acids. Since his discovery, the assisted degradation of materials caused by the exposure to hydrogen is studied intensely. Steels are frequently used as structural materials especially in engineering related fields and therefore, the threat of hydrogen degradation of all engineering alloys, specifically steel, might result in an unpredicted catastrophic failure by means of money and human lives. The exposure to any hydrogen-containing environment during manufacturing process and service must be considered due to the severe influence and the need to determine the life expectancy of an engineering structure. [2, 3] In general terms, hydrogen assisted degradation can be defined by the reduction of ductility (i.e. the ability to withstand deformation) rather than the reduction of strength (i.e. the ability to withstand physical load). However, hydrogen assisted cracking (HAC) and degradation of the properties are the results of very complicated processes and reliable lifetime prediction is often very difficult, if not impossible.[4, 5]

The environmental and mechanical aspects are only one side of the issue. The additional aspect addresses the wide range of physical properties within the material itself. One example of a hydrogen assisted cracking failure case is shown in Figure 1-1. The complicated interactions between the different aspects of hydrogen assisted cracking have resulted in an enormous number of publications that in some cases present controversial findings.[5, 6] Nowadays, the knowledge and understanding of hydrogen assisted degradation processes in low alloyed steels is well founded however, these materials are rarely used in risky applications and sensitive environments due to progress in the development of steel manufacturing. On the other hand, new materials are characterized by better durability and sustainability, not only in terms of load capacities and corrosion resistance but also in terms of susceptibility to hydrogen assisted cracking. The use of high alloyed steels and stainless steels, that in some cases contain complicated microstructures (i.e. welded components, DSSs, etc.), provide, in some cases, good solutions for energy applications due to the growing demand for better corrosion resistance or higher yield strengths. However, in this case, new problems regarding HAC are arising and new mechanisms should be considered.

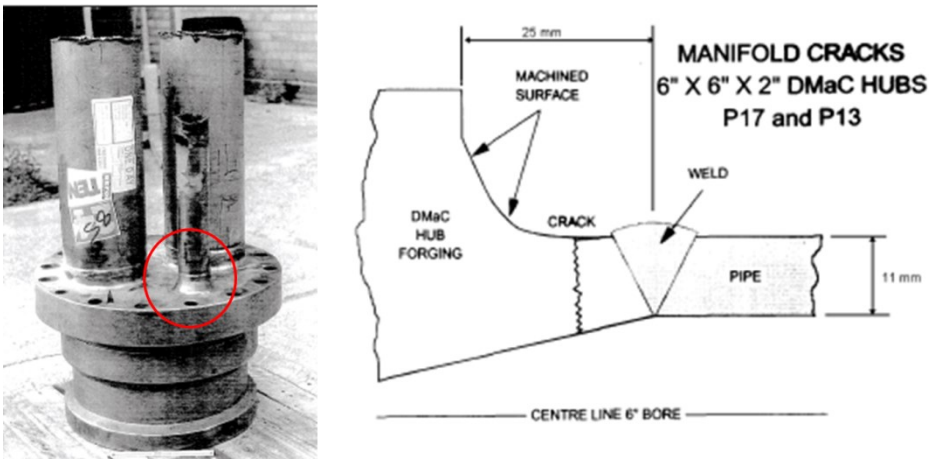

Figure 1-1: Example of a failure in a hub with welded pipe connectors from the BP Amoco Foinaven Field.[7] The component, made of a 2507 DSS, failed during service on the hub side close to the weld (marked with a red circle). The failure was a result of stress concentration in the connection between the hub and the pipe. The microstructure of coarse elongated grains oriented through the wall thickness enabled easy access of hydrogen.

A large number of theories have been provided to explain the interaction of hydrogen with the metallic lattice since the 1940's. However in recent years there is agreement on the responsible metallurgical mechanisms of HAC in steels, namely the Hydrogen Enhanced DEcohesion (HEDE) and the Hydrogen Enhanced Localized Plasticity (HELP) mechanisms. Nevertheless there is still a debate regarding the dominance of these mechanisms and relevance of other mechanisms in more complicated microstructures where the degradation process remains unclear. The main gap in this case is the compatibility of a mechanism with the observed phenomenon. The solution lies in both simulating and experimental validation. During recent decades, a large amount of analytical approaches and numerical models have been developed. These models are mainly used for simulation of hydrogen distribution and HAC in simple microstructures where many influencing factors are not considered properly. This problem is nowadays being considered by many researchers in this field and the development of new models is targeted on overcoming this gap.[8, 9] The main advantages of using these models are the reduction of efforts that are invested in experimental approaches and the ability to go deep into details that cannot be gained by conventional approaches (e.g. localized hydrogen distribution in scales of phase boundaries, grains and grain boundaries).

The conventional approaches for the detection and quantification of hydrogen are limited mainly by the obtainable resolution to localize the hydrogen in the microstructure. The concentration is calculated by the detection of the hydrogen after it is extracted from a charged specimen by thermal activation. To calculate the diffusion and permeation electrochemical permeation techniques enable the calculation of the hydrogen effective diffusion coefficient in accordance with the time it takes for hydrogen to permeate through a metal membrane.

The scientific community has defined the lack of information on hydrogen distribution in the microscale as one of the major gaps to reaching better understanding of the HAC phenomena and the validation of the suggested models. In recent years many groups worldwide are investing great efforts to obtain this information by a rather small number of advanced methods. The following literature survey is focused on the recent achievements that were obtained in the previous years with the advanced methods. Special attention is given to three methods which vary in obtainable resolution and limitations: neutron tomography (NT), secondary ion mass spectrometry (SIMS) and atom probe tomography (APT). These methods differentiate mainly by the ability to apply in-situ experiments. Noteworthy is that the better the spatial resolution, the more complicated the experimental setup becomes. These complications are expressed mainly by the sample geometry and the need to use a hydrogen tracer – deuterium (^{2}H, D). The later stems from the inability to distinguish hydrogen in the specimen from background hydrogen (adsorbed and absorbed during sample preparation, transfer and analysis). Despite the minor differences in diffusivity and permeation of the isotopes, publications based on both APT and SIMS show the ability to achieve reliable results by the use of deuterium. This is emphasized here not only in the available literature but also in the experimental part that is based on several trials.

The present work is targeted to elucidate the deuterium behavior in austenitic-ferritic DSSs under the consideration that deuterium behaves in many ways similar to hydrogen. Since hydrogen uptake depends upon how hydrogen is initially delivered to the material, the dissociation and diffusion through the microstructure and the interaction under applied mechanical load, the research was based on developing three novel experimental approaches to observe the uptake and interaction of hydrogen with the microstructure. The following approaches were developed here particularly to gain a better insight into these processes: 1. Elucidation of hydrogen distribution after electrochemical charging; 2. ToF-SIMS in-situ permeation and 3. ToF-SIMS in-situ mechanical loading.

Chemo-metric and high resolution structural characterization techniques were integrated with computational multivariate data analysis (MVA) and data fusion for the first time in this field to improve the data interpretability. The experimental approaches were applied to a two phase microstructure.

The deuterium was delivered in all experiments by cathodic reaction to imitate the process that takes place in aggressive environments such as in offshore applications. The dissociation and diffusion were analyzed in-situ and ex-situ to characterize in detail the occurring evolution of deuterium at the surface of each phase with and without the exposure to the aggressive medium. The ex-situ approach enabled establishment of the fundamentals for the advanced in-situ mechanical loading experiments. Subsequently, these experiments have shown a clear enrichment of deuterium in the microstructure under different loading conditions.

The main objectives of this work are the following:

- To explore the possibilities of Time-of-Flight Secondary Ion Mass Spectrometry (ToF-SIMS) for investigating hydrogen assisted degradation.
- To gain a better insight on the underlying mechanisms behind hydrogen assisted degradation in a two phase microstructure.
- To develop an in-situ approach to study the hydrogen distribution in the microstructure during the diffusion of hydrogen.
- To develop an in-situ approach to study the hydrogen distribution in the microstructure during exposure to an external mechanical load.

The examinations by these approaches should lead to further understanding of the hydrogen transport phenomenon and further development of the existing models for HAC mechanisms.

2 Literature survey

2.1 Stainless steels and duplex stainless steels

Stainless Fe-Cr-Alloys steels (with Fe<<90%) contain at least 10.5% Cr. Few stainless steels contain more than 30% Cr or less than 50% Fe. Stainless steels achieve their stainless characteristics through the formation of a thin and adherent chromium-rich oxide surface film. This chromium oxide layer is developed in the presence of oxygen. The selection of stainless steels for a specific application can stem from many different parameters such as corrosion resistance, fabrication characteristics, mechanical durability, desired properties in specific environments and temperature ranges, weldability and production cost. It can be claimed that in the past the corrosion resistance and mechanical properties were the most important factors in selecting a grade for a given application. However, nowadays, production costs and environmental implications are becoming more and more relevant. Stainless steels and in particular DSSs are often used in aggressive mediums where the combination of mechanical properties and corrosion resistance are required (as shown in Figure 2-1). The following chapter describes the evolution of stainless steels and particularly the development of duplex stainless steels.

Figure 2-1: Standard 2205 duplex stainless steel continuous sulphate pulp digester and impregnation tower in Sodra Cell Mönsteras, Sweden.

In addition to Cr, stainless steels were alloyed with Ni in Europe, US and East Asia, whereas in Africa they were alloyed with Mn instead of Ni to stabilize the austenitic phase. Since the early beginning of stainless steels, many other elements, additional to the main alloying elements (Cr, Ni or Mn), were added to those alloys. The addition of other elements is made in order to improve particular characteristics such as yield strength, stabilization of some phases over others, formation of different hardening mechanisms, weldability improvement, etc. Among the wide variety of alloying elements the most common are: molybdenum, copper, titanium, aluminum, silicon, niobium, nitrogen and sulfur. Carbon is normally present in amounts ranging from less than 0.03% to over 1.0% in certain martensitic stainless steels grades.[3, 10]

The development of stainless steels started at the beginning of the twentieth century in the United Kingdom and Germany. Due to production and refinement technologies the stainless steel contained relatively high carbon levels (above 0.08wt%) which resulted in high sensitivity to grain boundary embrittlement due to sensitization of the Cr with C.[11] The initial grades were the ferritic and martensitic grades. Since the 1920s stainless steels were commercially available from different producers such as Thyssen, Krupp, Vereinigte Deutsche Metallwerke AG (VDM) and Böhler in germany, Allegheny, Armco, Carpenter, Crucible, Firth-Sterling, Jessop, Ludlum, Republic and Rustless in the U.S. Nevertheless, relatively modest tonnages of stainless steel were produced at the beginning of the 20th century. Since this time, annual production has risen steadily. The production of austenitic grades was developed a few years later. [10]

At the same time the austenitic grades were being developed in the late 1930's the development of duplex stainless steels (DSS) had already started. This grade has a more complicated microstructure, where more than one phase exists in a significant amount. The first DSSs were experimentally produced in several countries across Europe and the U.S. The first record of such an alloy was made by Bain and Griffith in 1927 whereas the first commercial DSS was produced by Avesta Jernverk in Sweden and called 453E. This alloy contained 25% Cr and 5% Ni. Within less than a decade similar types of DSSs were developed and used commercially in autoclaves and valves in some industries.[11] These grades were developed to reduce the intergranular corrosion problems in early high-carbon austenitic stainless steels and are known today as Uranus 50.

The UR50 grade that was developed in France in 1936 with 20-35% ferrite (UNS S32404) contained 0.1 wt.-%t of nitrogen and 2.5 wt.-% of Mo and was commercially available in various forms for the oil refinement, food processing, pulp and paper, and pharmaceutical industries. These steels were produced in induction furnaces allowing accurate alloying

additions. The use of low pressure furnaces ensured carbon removal, rudimentary de-oxidation and restricted nitrogen ingress. Nevertheless, plate products remained sensitive to edge cracks.[12]

Another crucial factor in the development of low nickel alloys such as DSSs was the obtaining of raw materials, in particular nickel during the 1950s. During this time civil wars raged in Africa and Asia- one of the prime sources of nickel. Additionally, Cold War politics played a role because Eastern-bloc nations were also prime sources of this element. This led to the development of a series of austenitic stainless grades from the AISI 200 series in which manganese and nitrogen are partially substituted for nickel (and also known as austenite stabilizers). These elements were found to be also beneficial for the production of lean DSSs for the same reason.[10]

During the development of DSSs it was realized that the combination of ferrite and austenite had better resistance to chloride stress-corrosion cracking than a fully austenitic microstructure. Therefore many companies were heading towards exploiting and using DSS over austenitic steels. After the Second World War the 3RE60 grade, with good resistance to chloride stress corrosion cracking (SCC), and the AISI 329 were used extensively for heat exchanger tubing for nitric-acid service. Both wrought and cast DSSs have been used for a variety of process industry applications including vessels, heat exchangers and pumps. These alloys were classified as first-generation DSSs providing good performance with lower nickel content but were limited in the as-welded condition due to the formation of ferrite and a lower corrosion resistance. This problem limited the first-generation of DSSs for use only in a number of applications where a minimum amount of welds are required, if any at all.

The major progress in the development of DSSs compared to austenitic grades came in 1970 when the lack of nickel resulted in higher costs of the latter. Another cause for the progress in the development of DSSs was the expanded activity in the offshore oil and gas industry, which demanded materials that can function properly in aggressive environments. The progress was expressed by better production techniques (such as the introduction of the vacuum and argon oxygen decarburization processes). These techniques enabled a more accurate nitrogen content and a lower contaminations content, including carbon. These together with other processes that were introduced in the 70’s have contributed to lower production costs and higher quality. From 1970 onwards, the development of DSSs is focused on the addition of nitrogen and the reduction of carbon content in order to improve corrosion resistance and weldability and achieve high temperature stability of the dual microstructure by stabilizing the austenitic phase.

2.2 Microstructure, properties and production of duplex stainless steels

There are four groups of dual-phase microstructures. The four groups are shown in Figure 2-2 and can be categorized according to the following microstructures:

1. Dual microstructure where the volumes of the phases are equal and each phase consist of one or more grains. In this case there are γ/γ and δ/δ grain boundaries and γ/δ phase boundaries.

2. Dispersion microstructure where the second phase is nucleating in the first phase resulting in δ/δ grain boundaries and γ/δ phase boundaries.

3. Segregation/net microstructure where the second phase is nucleating on the grain boundaries of the first phase. This microstructure consists of δ/δ grain boundaries and γ/δ phase boundaries.

4. Dual-phase microstructure where the second phase is nucleating independently at the grain boundary of the primary phase. This microstructure consists of δ/δ grain boundaries and γ/δ phase boundaries.

It should be noted that only wrought alloys acquire a two phase 'sandwich' microstructure and are therefore called ''duplex stainless steels''. However, this term was also adopted to cast microstructures as well despite the fact that cast DSS has a dispersion microstructure.

In DSSs, both ferrite and austenite are formed in approximately equal proportions. In general, a DSS microstructure consists of ~70 wt.-% iron and 30 wt.-% alloying elements, therefore DSS is also counted as a high alloyed steel. The ratio between δ-ferrite and γ-austenite is controlled by many factors, the primary ones being the alloy components and the cooling rate.[3, 11] The resultant microstructure can be predicted by the Schaeffler diagram which was published in the early 1950's. The Schaeffler diagram is based on the relationship between the elements that stabilize the ferritic phase (bcc) or the austenitic phase (fcc).[13] The contribution of Cr refers not only to the formation of the passive oxide film but mainly to the stability of the ferritic phase. N and Ni, on the other side are contributing to the stability of the austenitic phase.

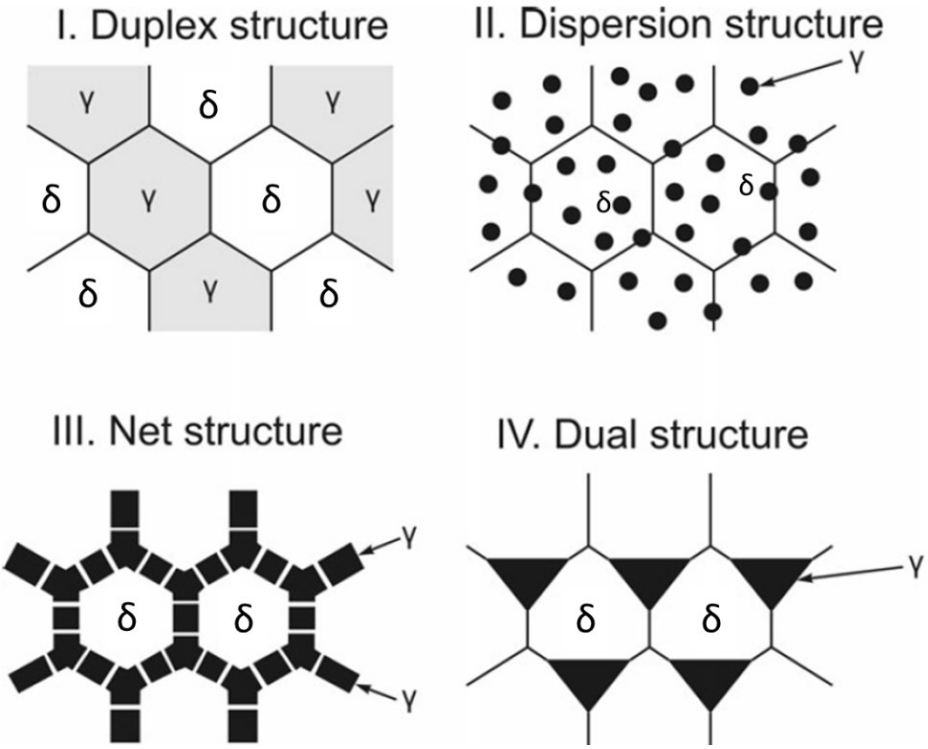

Figure 2-2: The four classifications of dual-phase microstructures.[13]

N has the strongest influence on the stability of the austenitic phase and is defined as the strongest stabilizer however; its solubility in the material is limited. Ogawa and Koseki have shown the high sensitivity of the volume fraction of austenite with even small N additions.[14] In addition to these elements there are a few other elements which are defined as strong phase-specific stabilizers. Mo, Si, Nb, Ti are defined as ferrite stabilizers whereas C, N, Mn and Cu are defined as austenite stabilizers. These elements are taken into account as Ni- or Cr- equivalents. The formula on which the Schaeffler diagram is based on was modified into a more accurate form from 1970 to the present.[15, 16] One example for this modification is shown in Eq. 2 suggested by DeLong in 1974.

The addition of alloying elements in steels suppress the martensitic transformation and based on the amount of phase-specific stabilizers, an austenitic phase (in case of high content of austenite stabilizers – Ni_{eq}) or a ferritic phase (in case of high content of ferrite stabilizers – Cr_{eq}) will be formed. Schaeffler and DeLong diagrams were expended and revised by the Welding Research Council (WRC) in 1988.[17] In this diagram the influence

of Mn was excluded from the Ni_{eq} equation. The diagram was further improved by Kotecki and Siewert [18] in 1992 (Figure 2-3) where the contribution of Cu was included in the Ni_{eq} calculations.

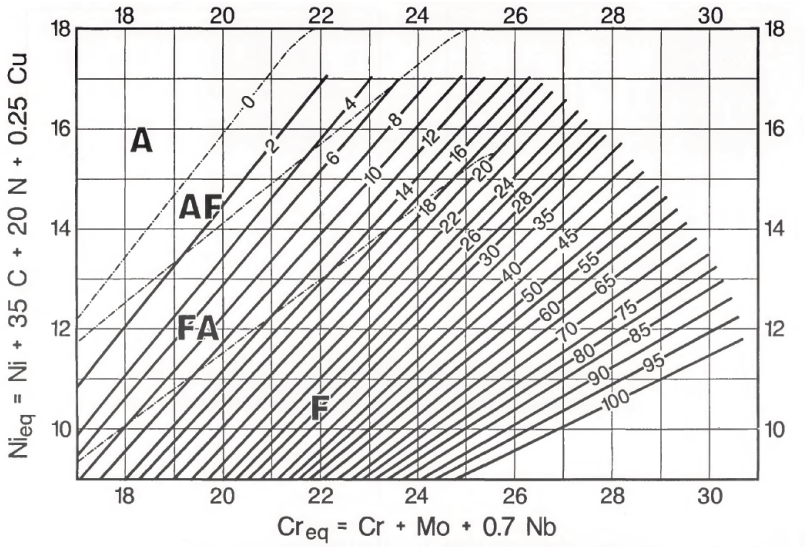

Figure 2-3: WRC-1992 diagram. The ferrite number (FN) prediction is only accurate for (weld) compositions that fall within the bounds of the iso-FN lines (0-100) that are drawn on the diagram. The limits of the diagram were determined by the database.[17, 18]

The chemical composition is also a crucial factor in the solidification process, especially in high alloyed steels such as DSS. Hammer[15], who offered one of the modifications to the Schaeffler diagram, has developed a thermodynamically based mathematical model to predict the primary crystallized phase. The model was improved by Ogawa[19] in 1984 and shown in equations 1-3:

$$\emptyset = Ni_{eq} - 0.75Cr_{eq} + 0.257 \quad (1)$$

Where

$$Ni_{eq} = Ni + 0.31Mn + 22C + 14.2N + Cu \quad (2)$$

$$Cr_{eq} = Cr + 1.37Mo + 1.5Si + 2Nb + 3Ti \quad (3)$$

according to the following ranges:

Φ<<0: Primary solidification of ferrite

Φ>>0: Primary solidification of austenite

Φ≈0: Solidification of ferrite and austenite

As mentioned before, the nature of the solidification process is controlled by chemical composition. The solidification process can occur in two ways.[11] The first path is based on a high content of ferrite stabilizers. In this case the liquid steel will solidify as δ ferrite. On further cooling, diffusion controlled inter- and intragranular precipitation of austenite will take place in the ferritic matrix (δ→δ+γ).

The second solidification path is called the 'flip-flop' solidification. This process can occur only by using a very slow cooling rate with a high amount of austenite-stabilizers (especially C and N). In this case solidification begins, similar to the previous process, with the solidification of δ ferrite. The liquid steel is then enriched with austenite stabilizers shifting the equilibrium and promoting the formation of γ austenite. The formation of austenite leads to ferrite-stabilizers melting, resulting again in ferrite solidification. This crystallization process results in the formation of δ dendrites with a γ interdendritic phase until solidification is complete. Here, further cooling results in a higher ratio of the austenitic phase due to:

I) Grain growth of the austenite grains and

II) Transformation of the ferrite into austenite (δ→δ+γ).

The increasing volume of the austenitic phase is shown in Figure 2-4a as a function of temperature. The Quasi-binary section through the Fe–Cr–Ni diagram at 70 wt.-% Fe (high alloyed steels), the DSS main alloying composition and the overview of phases formed as a function of temperature are shown in Figure 2-4b. It is noteworthy that there are distinct differences in microstructure between the austenite that is formed from liquid steel and that which is formed during the solid-state diffusion driven process.

The optimal microstructure of a DSS has a 50:50 ferrite: austenite ratio. However, the actual ratio between the phases varies between 40:60 and 60:40. The underlying reason for equal proportions of the two phases is the achievement of optimal mechanical and corrosion properties. In order to achieve equal proportions it is necessary to apply heat treatment. This treatment usually includes a hot rolling process which results in a preferred orientation of the microstructure. The heat treatment also includes an annealing process which allows for the optimal phase ratio and a homogenized, precipitation-free microstructure. The heat treatment is carried out at temperatures above 1,000°C and is finished by water quenching. Due to the high content of alloying elements slow cooling, and heating below 1000°C many phases might precipitate into the matrix. In most cases these

phases are undesired (such as χ phase and Cr_2N).[20] Therefore quenching ensures a precipitation-free microstructure.

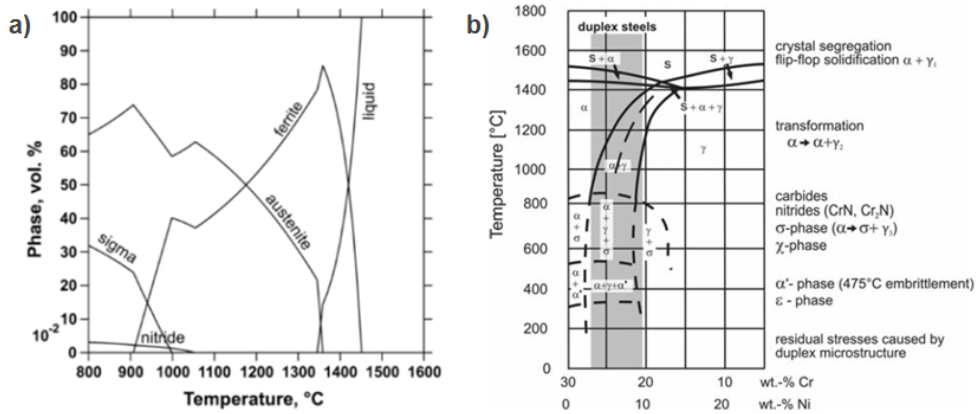

Figure 2-4: a) the formation of different phases during the solidification of the DSS alloy melt as a function of temperature and b) the Quasi-binary section through the Fe–Cr–Ni diagram at 70 wt.-% Fe.[13, 20]

The distribution of alloying elements is not only dependent on the respective solubility limits of elements but also on the heat treatment temperature and duration, and on the cooling rate. Interstitial elements (e.g. C and N) have much higher solubility in the fcc. These elements can occupy the octahedral and tetrahedral interstitial sites within the crystal lattice of the austenite. The distribution of other alloying elements follows the principle of the solubilities that were shown by Berns et al. [21].

The interstitial elements C and N, and the austenite stabilizing elements such as Ni, Cu, and Mn concentrate in the austenite phase, while ferrite is enriched with Mo and Cr. During formation and growth, the austenitic phase consumes the fcc-stabilizing elements such as Ni and Cu from ferrite by their diffusion into the fcc lattice and therefore the ferritic phase becomes enriched in Cr and Mo. Similar to the solidification process, the volume fraction of ferrite decreases at lower heat treatment temperatures. The slow cooling clearly promotes significant element segregation.

The heat treatment is followed by a rolling process in order to overcome the grain growth that is obtained during the solidification process. The deformation of the rolling process and the subsequent recrystallization result in grain refinement. In this way, the material acquires its typical ‘sandwich’ structure, resulting in a large increase in strength and toughness

according to the Hall–Petch principle[22]. The grain growth is hindered during deformation and heat treatment. Since grain growth is driven by diffusion, the austenite phase coarsens slowly; the ferritic grains tend to coalesce because of the rapid diffusion processes in the bcc lattice.

The properties of ferrite–austenite steel combine high strength with high ductility and outstanding corrosion-resistant properties[13, 23]. The major advantage of this alloy is that it has better mechanical properties than fully ferritic or fully austenitic alloys. Table 1 shows the comparison between the a ferritic-, austenitic- and DSS in main alloying elements, the yield strength and the ultimate tensile strength. As mentioned before, the production process typically consists of thermo-mechanical treatments. The typical microstructures of the ferritic, austenitic and DSSs are compared in Figure 2-5. Figure 2-6 shows a 3D sectioning of a typical DSS microstructure where the 'sandwich' microstructure is visible.

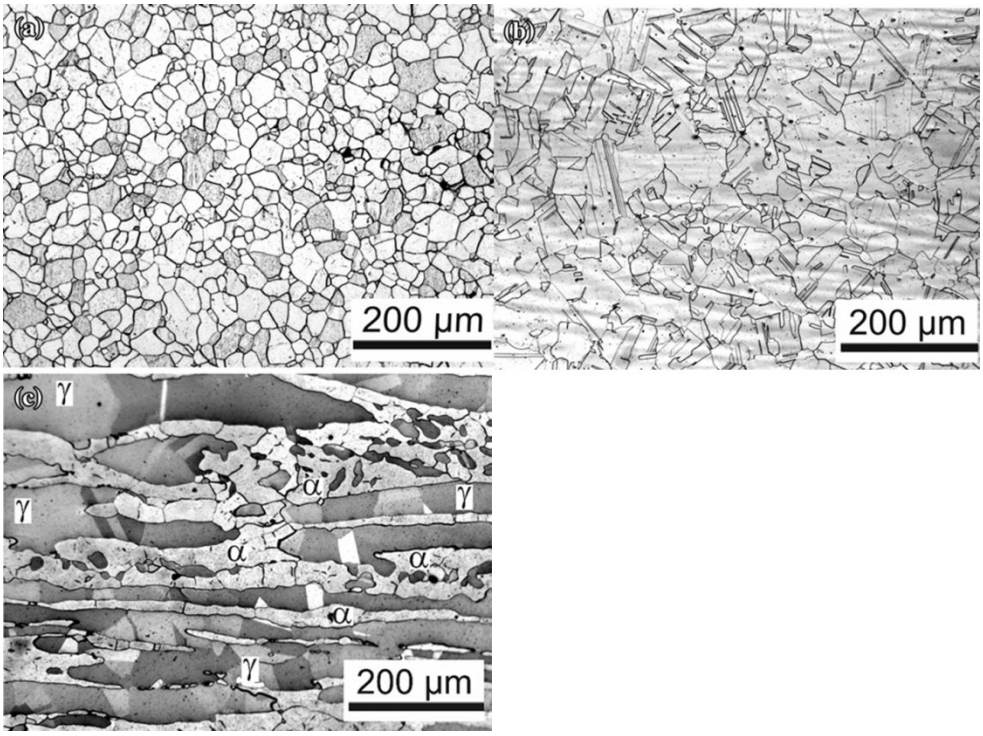

Figure 2-5: Microstructural comparison of a) ferritic, b) austenitic, and c) ferritic–austenitic DSSs. The DSS has its unique 'sandwich' microstructure. Etchant: aqua regia/V2Apickle (ferrite, austenite) and Beraha II reagent (duplex)[13]

Table 1: Basic composition in wt.-% and mechanical properties of three types of stainless steels

Structure	C	Cr	Ni	DIN	0.2 % YS $Rp_{0.2}$, (MPa)	UTS Rp_m (MPa)
Ferrite	<0.1	13-30	<.01	1.4015	345	540
Austenite	<0.1	17-26	7-26	1.4301	190	450
DSS	<0.1/0.4	24-28	4-7	1.4462	450	700

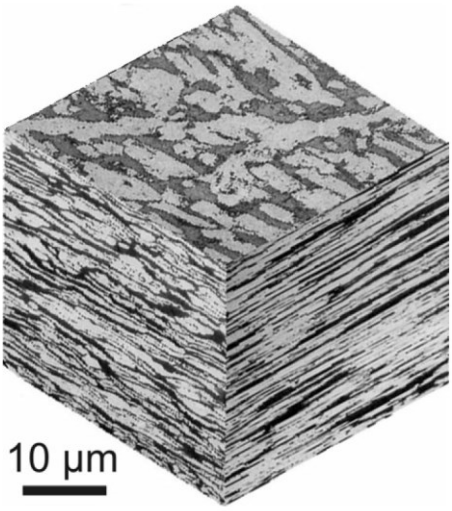

Figure 2-6: A 3D sectioning of typical DSS after thermo-mechanical treatment. The 'sandwich' microstructure is obtained parallel and normal to the rolling direction.[20, 24]

The DSS receives its unique properties mainly by chemical composition. The second generation of the DSS, which gains more interest from the scientific and industrial communities can be divided into several classifications, however the only criterion that has a consensus among all communities is the steel's corrosion resistance. The desired mechanical properties, and mainly the corrosion resistance of stainless steels, are obtained by optimizing the balance of the important alloying elements. The primary elements which contribute to the resistance of steel against localized corrosion (especially pitting corrosion) are Cr, Mo, N, and W. However W is used less frequently then the other elements (W is mainly used in super DSSs).

Based on the content of these elements it is possible to classify the stainless steels by their corrosion resistance. This classification is called the pitting resistance equivalent number (PREN) and it is calculated as the following (all elements are in wt.-%):

$$PREN = Cr + 3.3(Mo + 0.5W) + 16N \quad (4)$$

According to this classification there are five grades in the DSS class:

1. Lean duplex stainless steel – with a Mo content of 0.1-1.0 wt.-%, lowest content of Ni (~1.0-2.0) and the addition of Mn to stabilize the austenitic phase.
2. Mo-containing lean duplex stainless steel – with a Mo content of 1.0-2.0 wt.-%, lowest content of Ni (~1.0-2.0) and the addition of Mn to stabilize the austenitic phase.
3. Standard duplex stainless steel (DSS) - with around 22% Cr and 3% Mo, such as 2205, the workhorse grade accounting for nearly 60% of duplex use.
4. Super duplex stainless steel (SDSS) – with approximately 25% Cr and 3% Mo, with PREN of 40-45.
5. Hyper duplex stainless steel – with the highest Cr and Mo content and PREN above 45.

In the following section the contribution of each of the main alloying elements is given. The alloying elements content of the four main grades in the DSS is given in Table 2.

Chromium

Cr must be added to steel in order to obtain the corrosion resistance of stainless steel. Cr forms the passive film giving the material its corrosion resistance but only with a content of at least 12%. The second major role of this element is stabilization of the ferrite phase, therefore DSSs normally contain 20-29% Cr. This element is beneficial for resistance to both uniform and localized corrosion. Chromium is known to increase the pitting potential, the critical pitting temperature (CPT) and the critical crevice temperature (CCT) and therefore, it decreases the pit propagation rate. Nevertheless, too high a content of Cr can form intermetallic phases that reduce the ductility, toughness and corrosion resistance.

Molybdenum

Mo is counted as a ferrite-stabilizer. Mo strongly increases corrosion resistance and improves the passivation properties.[25] Although in some studies on the corrosion properties of DSSs in elevated temperature sea water[26] it was recommended to have at least 3% of Mo. The addition of Mo to DSSs is restricted to 4% (and 7% in austenitic steels)

since it enhances the formation of intermetallic phase precipitation by widening the σ phase field.[11, 27]

Nickel

Ni is a crucial element in DSSs for the formation of a stable austenitic phase. In order to keep the ferrite between 40-60% and to balance the austenite after solution annealing Ni is added. In DSS, the amount of Ni depends primarily on the chromium content. In the case of excess Ni content, the austenite level will be much higher than the desired ratio. Additionally, a high Ni-content accelerates α' formation, which is a brittle intermetallic phase, in the ferrite. In contrast, low nickel levels can result in the formation of a high amount of ferrite and therefore lead to a decrease in toughness. However, nickel has a positive effect on impact toughness at low temperatures. The influence of Ni on the corrosion properties of the material is still under debate. Pitting corrosion tests have shown that Ni can have a negative[28] or positive[11] influence.

Nitrogen

N is regarded as the most significant element to stabilize austenite and has a strong influence on several properties. Nitrogen has been reported to increase the stability of DSS alloys against the precipitation of intermetallic phases and to reduce the elemental partitioning of chromium and molybdenum between ferrite and austenite. The reason for the increase in stability arises from the occupation of interstitial sites (as well as carbon) in the solid solution in both ferrite and austenite. The addition of nitrogen is preferred, whereas carbon is undesirable in stainless steel due to the risk of sensitization. The use of nitrogen hinders the formation of intermetallic phases.[29]

Nitrogen has a strong influence on the passivity of stainless steels and is favorable for enhancing the corrosion properties.[28] Nitrogen significantly increases the strength of DSSs, but may also improve the ductility and toughness of the alloy.[30] Nevertheless, the amount of nitrogen that can be added is rather limited due to the risk of severe N_2 out-gassing or porosity during solidification when the solubility limit is reached for nitrogen.[11]

Manganese

Mn is also defined as an austenite-stabilizer. In lean DSS, Mn is used to compensate for the lack of Ni. According to the Schaeffler diagram Mn must be added in double the amount to obtain the same effect like Ni. The main advantage of Mn is that it increases the solubility of nitrogen. It was shown that Mn additions in excess of 3% and 6% increase the nitrogen levels to 0.1% and 0.23% respectively.[31] It has been reported that manganese itself may

have a negative effect on pitting resistance, but combined additions of nitrogen and manganese override this effect.[32] Replacing nickel with manganese and nitrogen is clearly reflected by the price of the material since the nickel price has fluctuated significantly in recent years.

Copper

This element is added to few of DSSs (mainly the SDSS such as 2507, S32750) for improving corrosion resistance in some mediums. The addition of Cu to DSSs, however, is limited to about 2% due to the fact that higher levels reduce hot ductility and can lead to precipitation hardening.

Carbon, Sulphur and phosphorus

The carbon content of most wrought DSSs is limited to 0.03%, mainly to eliminate precipitation of Cr-rich carbides which can act as initiation sites for pitting corrosion and intergranular cracking. S and P contents are controlled, although not eliminated since the presence of S is important for some weld applications.

Table 2: Typical ranges of alloying elements of the different grades in the DSS given in wt.-%.[11, 12, 27]

	Lean DSS	Standard DSS	SDSS	Hyper duplex stainless steel
EN No.	1.4162	1.4462	1.4410	
UNS no.	S32101	S32205	S32750	S32707
C	≤ 0.4	≤ 0.03	≤ 0.03	≤ 0.03
Cr	21-22	22-23	24-26	26-29
Ni	1.35-1.7	4.5-6.5	6-8	5.5-9.5
Mo	0.1-0.8	3.0-3.5	3-5	4-5
N	0.20-0.25	0.14-0.20	0.24-0.32	0.3-0.5
Mn	4-6	≤ 2.0	≤ 1.2	≤ 1.5
Cu	0.1-0.8		≤ 0.5	≤ 1.0
PREN	25	35	43	49

Due to the high content of the austenitic phase in DSS, the subject of deformation-induced martensitic transformation must be described in details in this work. Although deformation induced martensite can be considered as a positive character for the material (e.g. in automotive industry[33]) in the context of hydrogen assisted cracking it is mainly considered to cause a multitude of problems.[34]

Due to the desire in the recent years to reduce the Ni content, many scientific efforts are dedicated to understand better the nature of metastable austenitic stainless steels. The formation of induced martensite is connected directly to shear bands that are resulted by overlapping of stacking faults on 111 planes in the austenite.[3] Additionally to the induced martensite, also twinning or stacking fault bundles are resulted by different overlapping of those stacking faults. Specifically twins are formed when the stacking faults overlap on successive 111 planes, whereas the ε-martensite is generated if the overlapping of stacking faults occurs on alternate 111 planes.[3, 35]

When the phase transformation takes place it is generally accepted that ε martensite may act as nucleation sites of α' by describing the transformation relation.[36] However, there are still some argues about the transformation routes. Both transformation paths: γ→ ε→ α' and γ→ α' are symmetrically possible even in the same material.[37] However, in the first path the ε-martensite acts as an intermediate phase of α'.[38] It was recently shown that dislocations pile-ups are nucleation sites for α' embryos.[39] The formation of new martensitic embryos is suppressed when reaching a certain density of existing nucleated embryos. Despite that, the ones that already formed would develop further (described as 'stepwise transformation behavior'). In some cases it was shown that the route of the induced martensite transformation depends on the deformation temperature.[40] Regions of intersections between mechanical twins and shear bands or intersections between ε martensite and slip bands, twins or grain boundaries were also suggested by researchers as nucleation sites for α'.[40, 41]

There are many factors that influence the martensitic transformation in metastable stainless steels such as orientation of external loads[42, 43], deformation temperature[40] and grain size.[39, 44] For instance, Raman et al. [45] showed that coarser grains are contributing to higher amounts of α'. The influence of the temperature at which the material is deformed is mainly expressed by the transformation route and kinetics[40] and the influence of the strain rate was shown by Mirzadeh et al. [46]. In this work it was shown that increasing strain rate is resulting in smaller amounts of α'. Fukuda et al. [47] even showed that this type of phase transformation can be facilitated by applying magnetic field.

In summary, DSSs have much in common with austenitic and ferritic stainless grades with the synergy effect of both phases that are contained in the microstructure. Therefore this class has several unique advantages over the other classes. DSS has better stress corrosion cracking (SCC) resistance than most austenitic grades, greater toughness than most ferritic grades and higher strength than most grades of either type. Due to the fine-grained microstructure, nitrogen alloying and ferrite and austenite mixture, the mechanical strength of DSS is very high. This class may be used in many corrosive environments within the temperature range of approximately -50ºC to less than 300ºC. The lower nickel content is also a significant advantage by means of costs in comparison to austenitic alloys since DSSs provide similar corrosion resistance in many environments. The combination of higher strength, lower nickel content and better corrosion resistance makes DSSs an attractive alternative to austenitic grades in off-shore applications and other aggressive mediums where these properties are required, especially when the cost of nickel is high.[48, 49]

The 2205 DSS is frequently used in many offshore facilities. This grade contains 22 wt.-% of Cr and 5 wt.-% of Ni with a relatively large nitrogen content. Due to the large use of this grade it was also selected as a case study for this research. The second type of steel that was selected as a case study is the lean 2101 grade in order to observe the differences that occur only due to the different compositions (cf. Table 2).

2.3 Hydrogen failure cases in duplex stainless steels

It is very difficult to obtain information about real failure cases of DSSs with regards to hydrogen assisted degradation and cracking due to confidentiality reasons. Nevertheless, the scientific and industrial communities agree that hydrogen assisted cracking and degradation of metallic components are considered one of the highest priorities and require new experimental approaches to obtain better understanding of these phenomena. It has to be mentioned that DSS were chosen in this work in order to achieve a better understanding of hydrogen transport and cracking in a dual phase microstructure. Thus, the following chapter summarizes some published failure cases with regard to hydrogen assisted cracking. The first example is given in the introduction and shown in Figure 1-1.

2.3.1 Cracking of cold worked pipe

Marathon Oil UK Ltd (Brae field) had few cases of longitudinal cracking in 25%Cr DSS (831260) in production tubulars in the late 1980's (Figure 2-7). The tubulars failed under

excessive impact damage during removal from the frame during routine service. Although very little information was published on this case, it was concluded that the cause of failure is hydrogen degradation, caused by the galvanic couple between the DSS tubulars and the carbon steel casing. The tubulars had a yield strength in the range of 965-1103 MPa, obtained by cold work. The outcome from the conclusions was the replacement of the damaged tubulars with a lower degree of cold work tubulars. As a result, hydrogen could enter the tubulars but could not lead to cracking under these circumstances. The literature shows that steels with high strength (which can result even from cold work) have much higher sensitivity to cracking under hydrogen charging conditions.[11, 50, 51]

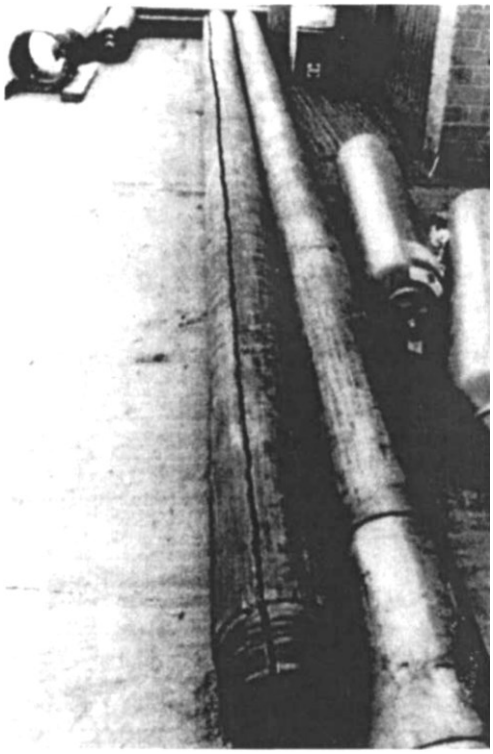

Figure 2-7: Cracked oilfield tubular (Marathon Oil UK Ltd.)[11]

2.3.2 Cracking in offshore production piping

Esso Production Malaysia Inc. (EPMI) discovered a large number of cracks in several welds during fabrication of an offshore production module made of UNS S31803 in the beginning of the 1990s. All the cracks were transverse to the weld and located mainly in the cap weld

metal (Figure 2-8). The attempts to repair the crack failed due to the formation of new cracks in adjacent areas. The cracks were detected after a time period ranging from 24 hours to a few months. The measured ferrite content in the weld metal gave typical values of 55% to 65% ferrite, however, in some regions of the weld much higher amounts of ferrite phase were revealed (up to fully ferritic regions). The fracture faces had a brittle nature (with extensive cleavage features). The welded ferrite revealed a hydrogen level of about 24 ppm H_2. It was concluded that the cracks were caused by the composition of the weld electrodes (leading to excessive ferrite contents), combined with high hydrogen levels. Based on this conclusion, EPMI removed the welds and changed the welding technique.[11, 52]

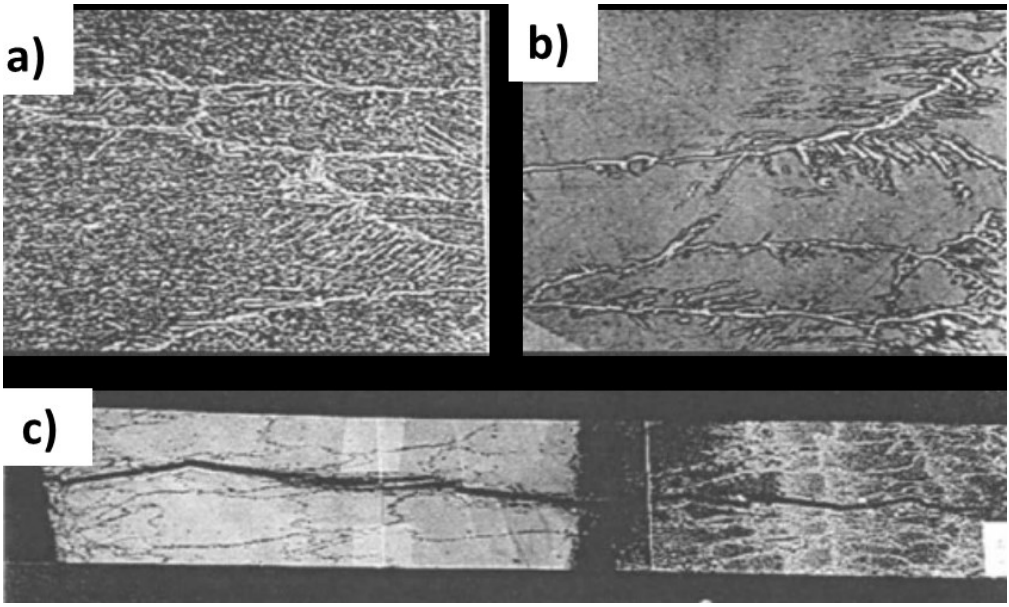

Figure 2-8: Example of (a) fill microstructure, (b) cap microstructure and (c) crack path in offshore production pipework (Exxon Production Research Company, Houston)[11]

2.3.3 Cracking of seam welded pipes

The Nederlandse Aardolie Maatschappij B.V. (NAM) experienced a major cracking problem in a seam welded pipe made of 22%Cr in 1980. All welding procedures were carried out with Ar+5% H_2 as the shielding gas, to improve the surface condition of the weld. After the welding was completed the component was tested by hydrostatic tests. After 24 hours of the material being under pressure a leak was found and within 76 hours a second leak found. The analysis of the pipes revealed that the microstructure in the root weld metals was almost completely ferritic and contained significant amounts of hydrogen. It was

concluded that the leaks were due to hydrogen cracking. As a result, it was recommended that repairs should contain heat treatment to remove the hydrogen and to re-establish the phase balance, and that hydrogen containing shielding gases should not be used.[11, 53]

2.4 Hydrogen assisted cracking and degradation of steels

The small diameter of the hydrogen ion allows it to easily occupy lattice sites in steels. The hydrogen mostly occupies interstitial sites in addition to locations and states, such as hydrides, or as gaseous hydrogen in internal surfaces or voids. The occupation of possible interstitial sites in the metal lattice differs strongly with the lattice type. Types of possible interstitial sites for hydrogen and the space distance are shown in Figure 2-9. In BCC phase (Figure 2-9 top) hydrogen is occupying mostly the T-sites[11, 54, 55] whereas in FCC phase (Figure 2-9 bottom) Hydrogen is preferably occupying the O-sites due to bigger space compared to T-sites. Despite a higher number of interstitial sites for hydrogen in a BCC lattice compared to an FCC lattice, phases with a BCC structure, like Ferritic steels, show lower hydrogen solubility compared to austenitic steels. On the other hand, BCC steels have elevated hydrogen diffusivity compared to FCC steels. In general, hydrogen solubility of austenite is approximately three orders of magnitude higher compared to ferrite and diffusivity is lower by five orders of magnitude.[56-59] In contrast to the ideal crystal, real microstructures contain large amounts of defects. These defects increase the hydrogen solubility above the lattice solubility. The defects are called trap sites. These are described in detail in chapter 2.4.3. It is essential to understand how hydrogen is adsorbed, absorbed and transported through the lattice. Hydrogen uptake is achieved in many ways. In the following chapter the three most relevant ways are explained. The most efficient method to ingress hydrogen into the bulk is by the process that contains the highest concentration of monoatomic hydrogen, resulting in the highest potential to be absorbed into the material. The source of hydrogen has a significant role in understanding the degradation mechanisms in steels, mainly due to the actual pressure of hydrogen on the surface in every process i.e. it's fugacity. The most common way for hydrogen to ingress into a metal is by the use of a liquid electrolytic medium during its dissolution in strong acids. This process is followed by evolution of molecular hydrogen gas (H_2) due to recombination of the atoms. This process is also regarded in the literature as hydrogen assisted stress corrosion cracking (HASCC). Another commonly used process to load the material with hydrogen is by using pure hydrogen gas and elevated temperature. These two methods to introduce hydrogen differ in complexity. Using an aqueous electrolyte the metal/electrolyte interface is

exposed to the presence of water dipoles in addition to other species from the use of acid (e.g. SO_4) and other substances originating, for example, from the use of recombination poison (Na^+, AsO_2^-). Another factor is homogeneity of the material. Inhomogeneity can be as a result of the existence of more than one phase, precipitates or surface quality due to polishing for example. The third process which is relevant in this context is the introduction of hydrogen during welding. Although this case is not dealt within the frame of this work, it is one of the most affecting factors in delayed cracking (i.e. cold cracking, HACC).

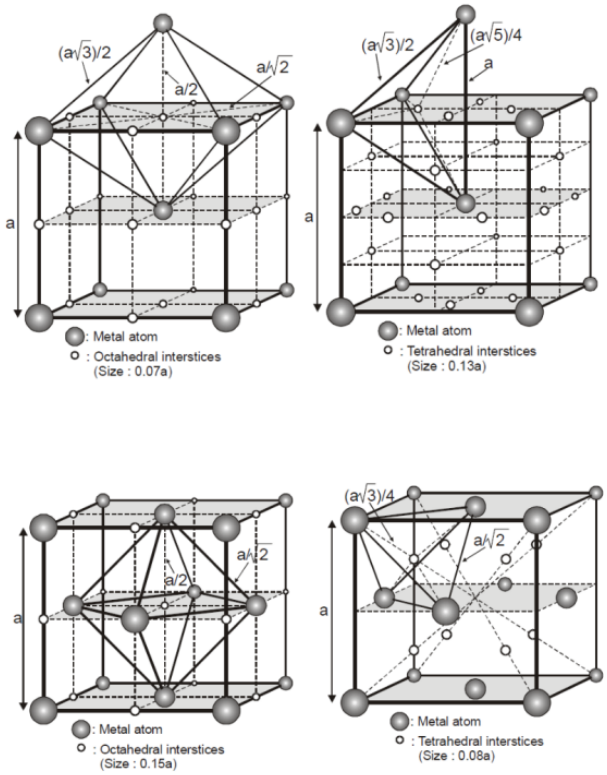

Figure 2-9: The tetrahedral (T) and octahedral (O) interstitial sites in BCC lattice (top) and in FCC lattice (bottom).[60, 61]

2.4.1 Hydrogen adsorption and absorption

Regardless of the cracking and transport mechanisms inside the material, the type of HAC is defined by the way it is entering the microstructure. Hydrogen is available in large quantities in many environments (such as in offshore facilities, gaseous hydrogen storage, acidic mediums in chemical industries). In each of these cases hydrogen is adsorbed at the steel surface and then further absorbed in the bulk material. The following chapter focuses on the mechanisms that take place only in aqueous mediums (i.e. electrochemical process). Considering the electrolyte/material interface according to The Volmer-Heyrovsky-Tafel mechanism[62] the adsorption and absorption of hydrogen occur in the following steps:

(I) the transport of H_3O^+ ions (in acid solutions) or OH^- (in alkaline solutions) in the electrolyte to the specimen surface,

(II) discharge (in acid solutions) or electrolysis of water (in alkaline solutions) and the adsorption at the specimen surface and

(IIIA) the recombination to molecular hydrogen or

(IIIB) absorption of the atomic hydrogen into the bulk material.

It is noteworthy that only atomic hydrogen is diffusible in the metal lattice. The reduction or electrolysis (II) and adsorption at the metal surface can be described in the following equations:

For acid solutions:

$$H_3O^+ + M + e^- \rightarrow H_2O + MH_{Ad} \quad (5)$$

For alkaline solutions:

$$H_2O + M + e^- \rightarrow OH^- + MH_{Ad} \quad (6)$$

where MH_{Ad} is the hydrogen atom absorbed on the metal surface.

Both previous equations are the cathodic part of the corrosion reaction of iron in acidic or strong alkaline solutions. The recombination (IIIA) of the absorbed hydrogen atoms can be described in the following equations:

For acid solutions:

$$MH_{Ad} + H_3O^+ + e^- \rightarrow H_2 + H_2O + M \quad (7)$$

For alkaline solutions:

$$MH_{Ad} + H_2O + e^- \rightarrow H_2 + OH^- + M \quad (8)$$

When hydrogen absorption (IIIB) takes place, there are many assumptions about the nature of the process. In general this process is described by a simple equation where the exchange rate (k) depends on the electrolyte conditions (composition, temperature, use of promoter, etc.):

$$H_{Ad} \rightarrow_k H_{Ab} \quad (9)$$

In other models it is assumed that hydrogen is absorbed in the bulk material of metals by release of the electron of the hydrogen atom to the metal atom (or the lattice)[54] resulting in a remaining proton in accordance with the following equation:

$$H_{Ad} \rightarrow H_{Ab}^{+} + e^{-} \quad (10)$$

The resulting adsorption and absorption of hydrogen into the material during electrochemical charging can be relatively low, therefore in many investigations a hydrogen entry promoter is used (also known as recombination poison). There are few types of promoters that are frequently used for this purpose. These salts or compounds (that are used in gaseous hydrogen charging) have the tendency to keep high amounts of ions in the electrolyte and on the metal surface, preventing the hydrogen from combining to a molecular state. The recombination poison consists typically of elements belonging to the V-A and VI-A periodic groups such as: S, P, As, Sb, Se and Te. In gaseous charging the following compounds can be used: CN, CNS and I. In many cases there is a strong reaction between these components and the specimen surface, so it is necessary to use carbon based poisons such as: CS_2, CO, CON_2H_4 and CSN_2H_4. Despite the frequent use of these promoters, there are still some arguments about the effective use of this poison and the ability to compare laboratory conditions with the use of the poison in the real conditions of an engineered component in an aggressive environment.[62, 63]

2.4.2 Hydrogen diffusion and mobility

In steels, the primary diffusion mechanism for hydrogen, under no plastic deformation of the component, is based on interstitial jumps. As mentioned before, the BCC structure is characterized by a high diffusion rate and a low solubility of hydrogen due to the low packing factor in comparison to FCC. Whereas the latter is characterized by a lower diffusion rate and a higher solubility due to its close packed lattice structure. Two more structures that should be taken into account (and explained in detail later) are the body centered tetragonal (BCT) and the close packed hexagonal (HCP). These structures have a diffusion rate of hydrogen between the ferritic and austenitic phases.

The reported diffusion coefficient of DSSs, regardless of charging conditions, varies between $1.8 \cdot 10^{-12}$- $4.6 \cdot 10^{-16}$ m^2/s.[9, 58, 64, 65] The reasons behind the slower diffusion in DSSs than in ferritic steels are as follows:

I) Increased diffusion length in ferrite due to austenite islands. This effect is defined as the “tortuous path” for hydrogen.

II) Larger number of traps (mainly in the δ/γ phase boundaries) than single phase alloys.

The literature shows a variance in diffusion coefficients of hydrogen in the same DSS. One of the main affecting factors is the relation of the permeation direction to the austenitic islands. A permeation direction parallel with the rolling direction of the steel is promoting a straighter diffusion path along the ferrite grains. As a result, – a faster diffusion rate will be obtained. Fine dispersed austenite islands promote longer diffusion paths and more trapping compared to a structure consisting of coarse austenite islands and larger intermediate ferrite “paths”. Zakroczymski and Owczarek even reported [66] a diffusion coefficient of trapped hydrogen of $1.4 \cdot 10^{-16}$ m^2/s, which is in the same order of magnitude as the values for austenitic steels. Therefore, it is assumed that the austenitic phase acts as a trap. Another influencing factor on the diffusion of hydrogen in DSSs (based on the permeation of hydrogen through a DSS membrane) is the permeation path. Owczarek and Zakroczymski[57] have shown that a thicker permeation membrane results in a non-linear increase in the actual diffusion path. The relationship between the membrane thickness and the actual permeation path is shown in Figure 2-10.

Another important Hydrogen transport mechanism is along short circuit paths. There are many assumptions regarding the preferred paths and the nature of hydrogen diffusion in stainless steels.[56] An overview of local distribution of hydrogen in phases with different properties and the role of grain and phase boundaries [67, 68] is still incomplete.[9, 57] The microstructure’s orientation[69], the large differences between diffusion coefficients of hydrogen in different phases and the heat treatments strongly influence the diffusion behaviour of hydrogen.[9, 70] As a result, there are many contradictory publications in this topic.[71]

As it was shown by Owczarec et al. [57] the influence of the austenitic phase on diffusion of hydrogen in a DSS can vary dramatically by the distribution of the austenitic phase. However, by examination of each phase separately it was shown that even the grain size of the phases have a crucial influence on the diffusion rate.[71, 72] Yazdipour[73] and Oudriss[74] concluded that the boundary surface area per unit volume is less dominant in a coarse microstructure than in a fine microstructure of a single phase X70 steel. Mine et al. [75] found that titanium precipitates reduce the diffusion rate whereas FeCr precipitates

have no effect in an ultrafine-grained austenitic stainless steel. In the case of precipitates the available literature is based mainly on modelling and macro-scale measurements.

The final and most important hydrogen transport mechanism is based on the movement of dislocations. This mechanism is influenced by two factors; the available hydrogen and an applied load. The reason for the higher priority of this mechanism is that it is much faster than the two other mentioned diffusion mechanisms. This mechanism was published for the first time by Bastien[76] and was further developed by Tien et al.[77].

Only when the material is subjected to severe external loads and goes through plastic deformation can hydrogen be transported into regions of high stress/strain (e.g. in front of a crack tip). The transport of hydrogen is accompanied by enhanced dislocation formation and movement. Moreover, the presence of a hydrogen atmosphere in the dislocation results in easier movement of the dislocation through less interaction with stress fields and obstacles.[6, 78, 79]

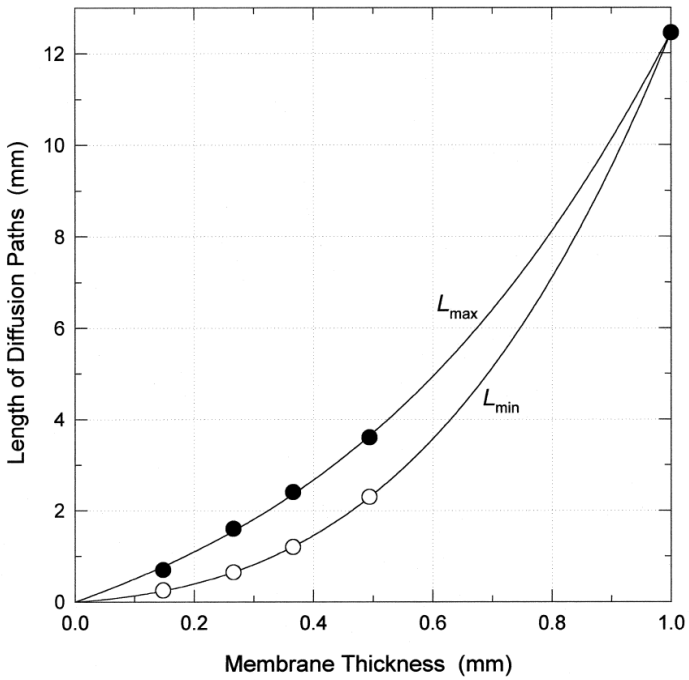

Figure 2-10: The relationship between membrane thickness and actual permeation path in a 25 wt.-% *Cr DSS.[57]*

This mechanism was proven in a large number of publications by direct macro-quantifications and indirect sub-micron elucidations where the enhancement of hydrogen

mass transport under external loading conditions consequently induced plastic deformation. The most crucial conclusion was that hydrogen effective diffusivity can increase by approximately 5 orders of magnitude under the combined conditions of plastic deformation during electrochemical cathodic charging.[80]Despite the reported observations regarding the influence of the austenitic phase on the diffusivity of hydrogen, there seems to be a lack of local observations on this topic to elucidate locally the role of the amount, orientation and trapping tendency of the austenitic phase in the DSS microstructure.

2.4.3 Hydrogen trapping

Apart from the diffusible hydrogen that occupies the interstitial sites in the lattice due to energy reasons, hydrogen can be trapped in defects in the lattice including dislocations, vacancies, impurities, grain and phase boundaries, particles and voids, as illustrated in Figure 2-11. These locations are defined as hydrogen trap sites. The difference between diffusible hydrogen and trapped hydrogen is the necessary time, or energy, required to release the atom. A higher number of traps results in higher solubility and lower diffusivity of hydrogen in the microstructure, therefore an increased amount of hydrogen traps will increase the capacity of hydrogen in the steel. The trapping theory was first published[81] in the 1960's. McNabb et al. [81] showed that hydrogen diffusion in metallic materials does not correspond to Fick's laws. With regards to the trapping sites in DSSs, as mentioned before, due to the large differences in the diffusion coefficients between the δ and γ, and the low diffusion rate in the latter, the austenitic phase is referred to as a trap in the DSS matrix. For DSS, this behavior does not apply to diffusion at a temperature above 700˚C (where the energy is sufficient in order to release the hydrogen from all traps). As shown in Figure 2-11, there are different kinds of traps which differ in the required energy for releasing hydrogen; this energy is defined as the trap binding energy. In other words, the hydrogen free energy in the trap is lower than the energy in the lattice interstitial site as shown in Figure 2-12. The binding energy divides the traps into two main types, reversible and irreversible traps. A reversible trap is defined as having a binding energy of below 60-70 kJ/mole whereas for irreversible traps the energy barrier for regaining the mobility is higher. Non-metallic inclusions and precipitates are typical irreversible traps.

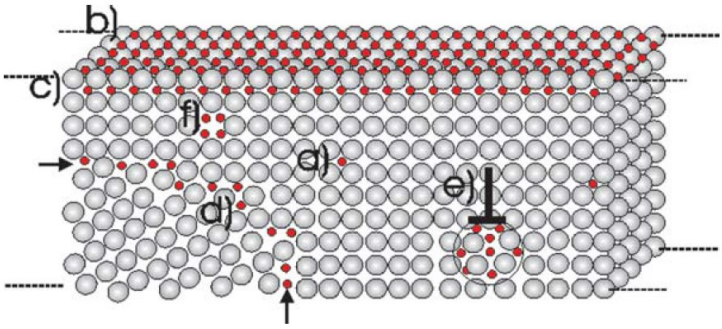

Figure 2-11: Various potential traps in a steel microstructure: a) dissolved in the microstructure, b) adsorbed and (c) absorbed at the surface, d) trapped in grain and\or phase boundaries, e) in stressed/strained regions (such as dislocations), f) in vacancies.[82]

The dimensions of traps vary from the scale of an atomic one dimensional defect (such as a dislocation) to a micron- and sub-micron scale three-dimensional defect, such as grain and phase boundaries. The key for better understanding of hydrogen assisted degradation and cracking is in the detection and quantification of hydrogen occupation in these defects

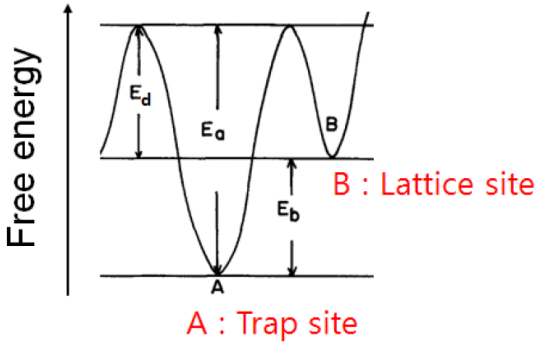

Figure 2-12: The energy level of hydrogen around trap sites[83]

2.4.4 Hydrogen assisted cracking (HAC)

The phenomenology of HAC can be described by three factors: the local/global mechanical load, the local microstructure and the hydrogen concentration. Hydrogen easily diffuses into almost any alloy matrix and can be trapped by certain internal defects, such as grain and phase boundaries, dislocations, non-metallic inclusions and precipitates in structural materials. The consequences are well known for more than half a century; the alloy's mechanical properties degrade and it may be subjected to a premature failure due to embrittlement. The risk of HAC in structural components, especially steels, presents enormous challenges in terms of material selection for a wide range of applications, predominantly in energy generation related fields and marine environment applications.[12] The hydrogen degradation mechanism entails a set of complicated processes that occur before and during service and might lead to a catastrophic failure.[6, 68, 84-86] The life time of structural components in such applications is mainly controlled by the factors mentioned above (hydrogen concentration, sensitivity of the material's microstructure to increased hydrogen concentration and applied mechanical load). These three factors are key for the establishment of hydrogen assisted cracking models that are used to explain the degradation processes, as shown in Figure 2-13.

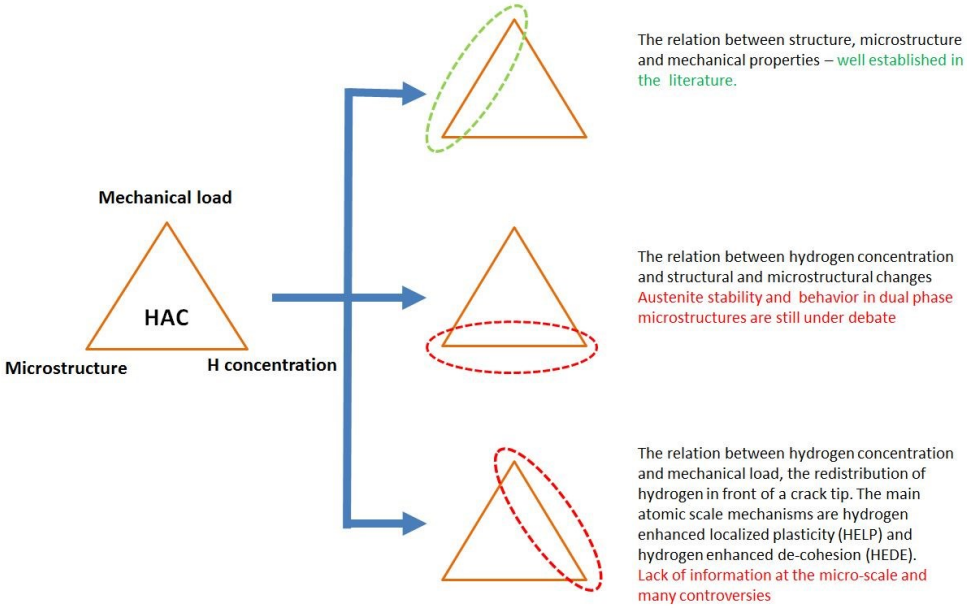

Figure 2-13: Influencing factors in hydrogen assisted degradation and cracking of steels. The main knowledge gaps are described as well.

Each factor shown in Figure 2-13 contains many parameters and these are expanded upon in the following:

The Microstructure:

This term consists of two main expressions that are often confused:

I) The microstructure – this encompasses the chemical composition, phase distribution and preferred orientation, grain size, grain and phase boundaries, inclusions or precipitations and

II) The crystal structure – this includes the lattice structure (FCC, BCC, HCP, etc.) and structural defects (dislocations density, stacking fault, twinning, etc.)

The mechanical stress:

This term can be separated by local and global stresses or by external and internal stresses. The mechanical load is influenced by the fabrication and service conditions. A DSS lattice contains internal stresses between different phases in addition to residual stresses induced during fabrication, welding and service. It

should be noted that these parameters are as a result of elevated temperature application.

The local hydrogen concentration:

This expression represents the amount of hydrogen in the material (it is separated into diffusible and trapped hydrogen). It is important to know how the hydrogen is loaded into the material (during fabrication including welding or during service by cathodic protection for instance). The “critical” hydrogen concentration that might lead to local failure depends on the other parameters, e.g. martensitic steels with higher hardness are more susceptible to HAC than austenitic steels with higher ductility and therefore fail with lower hydrogen concentrations.

The models that are used to explain the degradation processes are based on several proposed mechanisms at the nano-scale. These mechanisms are relying on, in most cases, complementary hydrogen sensitive macro-scale methods (such as Thermal desorption spectroscopy, carrier gas hot extraction, etc., for the quantification of hydrogen concentration), mechanical properties testing methods and posterior hydrogen non-sensitive sub-micron scale topographic and structural observations (mainly by electron microscopy). The application of some of the suggested models becomes more challenging for complex microstructures containing more than one phase (e.g. welded components and austenitic-ferritic stainless steels) often resulting in contradictory conclusions.

It is agreed that on the atomic scale there is more than one mechanism active and involved during the degradation process. Numerous mechanisms have been proposed to account for hydrogen assisted cracking, however, the more dominant mechanisms for steel under mechanical load and sufficiently dissolved hydrogen are hydrogen enhanced de-cohesion (HEDE)[87] and hydrogen enhanced localized plasticity (HELP) [3, 5, 6, 68, 88, 89]. For all proposed mechanisms – the impact of each depends locally on the microstructure, mechanical load and hydrogen concentration (Figure 2-13). One example of the relation between these factors has been given in section 2.3.1. where it was shown that the higher the material strength, the more it is susceptible to hydrogen. In addition to this, in a heterogeneous microstructure containing different concentrations of hydrogen in different features (phases, grain/phase boundaries, precipitates) each region behaves differently under mechanical load with different active embrittlement mechanisms.[90] In addition, one mechanism can be replaced by another during the degradation process and therefore a posteriori analysis might be in many cases misleading.[6]

One of the biggest gaps for further progress in understanding the embrittlement process is the lack of methods for the validation of all suggested mechanisms. Such a method must have the ability to locally and accurately map the hydrogen distribution at the submicron scale.[91] The diffusion process of hydrogen and the interaction of hydrogen with strained regions in the material (e.g. an evolving crack) can be realized only by applying such a technique following and during these processes, i.e. by ex-situ, in-vitro and in-situ experiments.[82]

2.4.5 Hydrogen assisted cracking mechanisms

In addition to the extensive discussion in the last century, particularly over the last decade a variety of mechanisms and theories have been proposed in order to explain the behavior of engineered components under mechanical load and higher hydrogen concentration. There are still many controversies and disagreements about the relevance of some of the failure mechanisms and their dynamics. The embrittlement of a metal and the degradation of the mechanical and physical properties by the presence of hydrogen is a complex process which involves many of the embrittlement mechanisms.[86] Each case (by means of structure, load, and hydrogen concentrations) has its own circumstances, relevant failure mechanisms and the order of the mechanisms that take part in the degradation process. Some of the mechanisms are referring more to the surface where the hydrogen source is playing a more dominant role, whereas in the case of precipitates from the IV and V transition mechanisms, metals can crack due to the formation of brittle hydrides. Most of the relevant mechanisms were reviewed by Robertson[6] and listed in the following:

- Hydrogen enhanced de-cohesion[87, 92-96]
- Hydrogen-enhanced localized plasticity[88, 97-100]
- High hydrogen pressure bubble or void[101, 102]
- Hydrogen-induced reduction in surface energy[103, 104]
- Hydrogen-enhanced dislocation ejection from the surface or near surface region[105]
- Hydrogen- and deformation-assisted vacancy production[106]
- Hydrogen-triggered ductile to brittle transition[107, 108]
- Hydride formation and cleavage[109, 110]
- Hydrogen- and strain-induced phase transformations[111, 112]
- Reactants and hydrogen[113]

It is agreed that on the atomic scale there is more than one mechanism active and involved during the degradation process. Numerous mechanisms have been proposed to account for hydrogen assisted cracking, however, the more dominant mechanisms for steel under mechanical loading and sufficiently dissolved hydrogen are: adsorption induced dislocation emission (AIDE)[114, 115], hydrogen enhanced de-cohesion (HEDE)[87] and hydrogen enhanced localized plasticity (HELP). [3, 5, 6, 68, 88-90] Additionally to these, in the frame of this research it is necessary to introduce the following additional mechanisms: the hydrogen assisted phase transformation and the pressure theory. In the following sections the suggested embrittlement mechanisms will be presented and discussed in detail.

2.4.5.1 Adsorption induced dislocation emission (AIDE)

Lynch was the first researcher who introduced the AIDE mechanism.[114, 115] This mechanism has a higher complicity than other mechanisms since it is based on some of the basic mechanisms that were developed earlier. This mechanism argues that hydrogen has to be first adsorbed near a crack tip. The adsorption of hydrogen results in subsequent formation of dislocations.[116] The formation and emission of dislocations from the crack tip affects the mechanical properties under further plastic deformation. By applying a sufficient load the dislocations can easily move away from the crack tip. As part of the nucleation of a dislocation, a dislocation core is formed by shearing of several atomic layers. Another part of this process is the formation of microvoids ahead of the crack tip as well as nucleation and growth of voids at second phase particles. However, the more dominant part in the propagation of the crack occurs firstly by the emission of dislocations from crack tips. It should be noted that the process is accompanied by the absorption of hydrogen that weakens the interatomic bonds in the range of several atomic layers. All the sub-processes in the AIDE are shown in Figure 2-14.

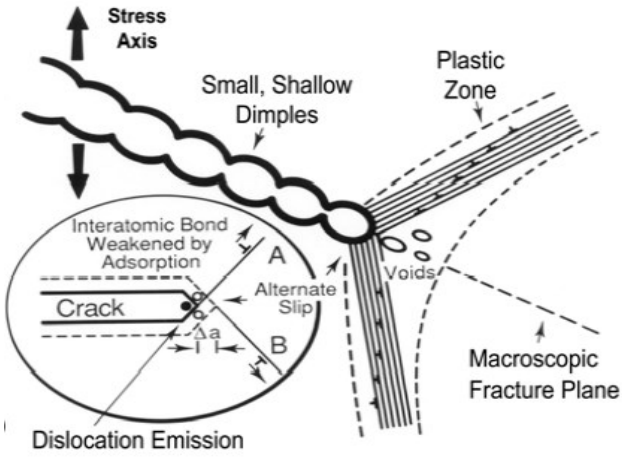

Figure 2-14: A schematic illustration of the AIDE mechanism involves alternate-slip from crack tips facilitating coalescence of cracks with voids formed in the plastic zone ahead of cracks.[105, 115]

2.4.5.2 Hydrogen enhanced de-cohesion (HEDE)

This model is based on a simple assumption, the model was developed by Troiano[94] and Oriani[87] in the 1960's since the existing theories in this time were unable to explain some of the early experiments with hydrogenated samples under mechanical load. The idea behind the HEDE mechanism is that a solute hydrogen atom in the metallic matrix can share its electron to the 3d-orbitals of the neighbor iron atoms and remain as a proton in the matrix. As a result the electron density increases locally and the cohesive force between the metal atoms is reduced allowing the propagation of the crack under lower load as shown in Figure 2-15a.

2.4.5.3 Hydrogen enhanced localized plasticity (HELP)

This theory is based on the two contradictory hardening/softening effects of hydrogen in different alloys that was reported by Nelson in 1983.[117] The HELP theory was developed by Sirois[118] and Sofronis[88] and was proven by novel set of in-situ experiments in transmission electron microscopy (TEM) by Tabata et al.[97]. The HELP process explains the interaction of dislocations with hydrogen. This mechanism requires a certain concentration of hydrogen dissolved in front of the in the crack tip or in the stress concentration area. During the movement of a dislocation by external stresses, the hydrogen can enhance locally the dislocation movement at lower stresses. In other words,

dislocations shielded by hydrogen cloud will move faster than ones without it when a similar shear stress is applied on the material. In order to keep enhancing the velocity and to continue the dislocations must carry the hydrogen environment with them. As a result the local hydrogen concentration is driven by the motion of dislocations and the obtained fracture has a local ductile failure with a brittle appearance on the macroscopic scale. Tabata et al.[97] conducted several in-situ experiments by environmental TEM in order to compare the effect of vacuum and H_2 on mechanically loaded Fe sample. These experiments showed that dislocations nucleation and movement are facilitated under the hydrogen environment. Hydrogen can also shield the dislocations and reduces the interactions between defects and precipitates. The HELP is illustrated in Figure 2-15a.

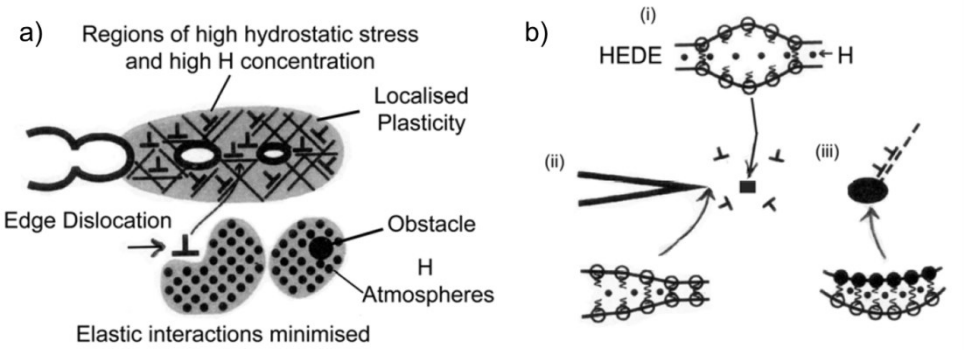

Figure 2-15: A schematic diagrams illustrating the hydrogen enhanced localized plasticity mechanism – HELP (a) and the hydrogen enhanced decohasion mechanism – HEDE (b) where the weakening interatomic bonds takes place by (i) hydrogen in the lattice, (ii) adsorbed hydrogen, (iii) hydrogen at the precipitate-matrix interface.[70]

2.4.5.4 High hydrogen pressure bubble or void

When high concentration of hydrogen is located in a trap in the microstructure there is always the risk of recombination of two hydrogen atoms back into molecular hydrogen. This recombination process is defined as the pressure theory which is one of the first theories in this field. The hydrogen molecules generate high pressure in the matrix that eventually leads to blisters and cracks as shown in Figure 2-16. Hydrogen does not necessarily recombine in traps but can also form during electrochemical hydrogen charging (this type of hydrogen ingress results in very high fugacity on the surface and therefore very high

concentration in the subsurface layers). The susceptibility of DSS for this type of degradation is due to the large differences in the diffusion coefficients between the two phases. Nevertheless, for other grades the formation of voids or blisters, by the recombination of hydrogen, can occur around impurities or in micro-voids. The combination of mechanical load and hydrogen is not covered by this theory and therefore it is limited for specific cases.[119-121]

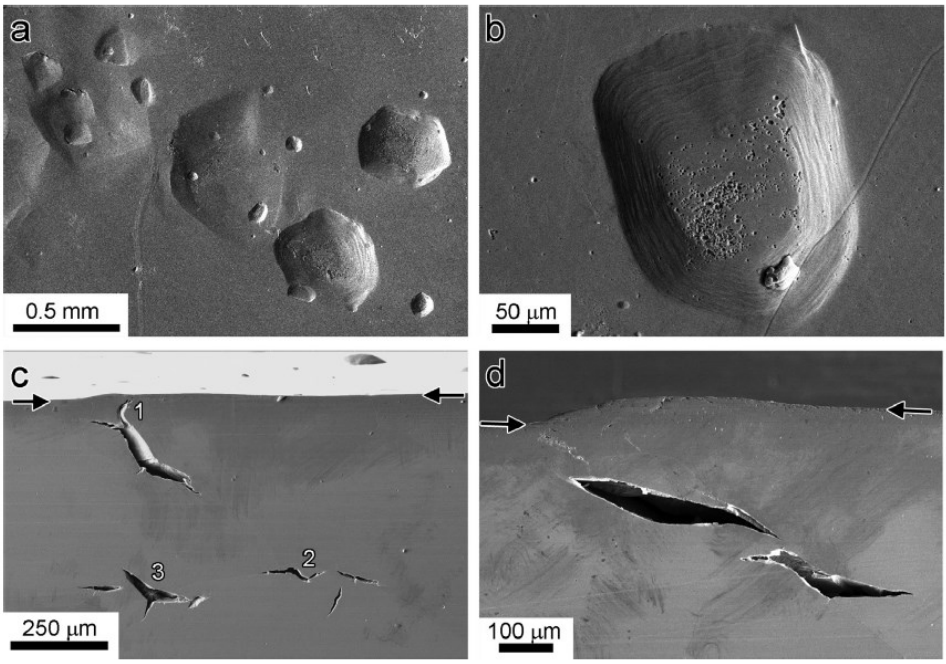

Figure 2-16: SEM images of blister in different location in a high purity iron in (a) low and (b) high magnification. (c) Cross-section of the sample showing the morphologies of internal cracks where the hydrogen was accumulating. The surface of the sample is marked by arrows. 1) Crack underneath blister showing curving of crack towards the free surface. 2) Zig-zag crack morphology. 3) Triple-point crack morphology. (d) Close-up view of a cross-section of a blister and the underlying crack.[120]

2.4.5.5 Hydrogen- and strain-induced phase transformation

As mentioned in chapter 2.2, Ni which is the most common austenite stabilizer can vary between 1-4 wt.-% in lean DSSs, 5-7 wt.-% in standard DSSs and above 8 wt.-% in austenitic stainless steel grades.[11, 12] The attempts to use grades with lower Ni content and the replacement of this element with Mn and N in DSS lead to the instability of the

austenitic phase under any applied strains and stresses. In addition, due to the relatively low stacking fault energy, the austenite can undergo phase transformation by quenching to low temperatures, plastic deformation and even irradiation by various ions. High concentrations of hydrogen (even when excluding mechanical load) produce large distortion in the lattice. As a result the lattice can transform into brittle martensite during the exposure to strains and/or hydrogen. Two kinds of martensite can form in the austenitic phase: α' (bcc) and ε (hcp). In the present, there are still some controversial opinions about the nature of this transformation. Luu et al. [122] obtained no phase transformation in the austenitic phase of a 2205 DSS after charging with hydrogen in an electrochemical process. Marchi et al. [123] have shown that by gas phase thermal charging of a super DSS type 2507 no phase transformation was obtained in the austenite. On the contrary, Han et al. [124] showed that even 304 and 316 austenitic grades (with higher nickel content than DSSs) undergo a phase transformation during gaseous hydrogen charging whereas only the 310s grade (containing more than 20 wt.-% of nickel) was not affected by charging. One may conclude from the literature that the correlation between the local hydrogen distribution and the expected transformation is missing (including the type of obtained martensite in relation to the hydrogen concentration). The two main implications on the sustainability of steels due to phase transformation are: I) The brittle nature of the martensitic phase upon the austenite facilitates the initiation and propagation of a crack (where the residual stresses due to the transformation, are assumed to contribute to this degradation process), II) The α'-martensite phase in the austenite enhances the hydrogen diffusion since hydrogen diffusivity in α'-martensite is higher in few orders of magnitude than in the austenite phase.

2.4.5.6 Hydrogen induced reduction in surface energy (Adsorption theory)

The adsorption theory was developed by Uhlig[125] in the 1960s. This theory was established based on the Griffith criterion for fracture in ideally brittle solids. As it was described in the HEDE mechanism hydrogen has been thought to reduce the binding energy of the metal atoms, however, in this case at the extreme root of notch. As a result, the critical level of the shear stress required to create new surfaces is reached. The main assumption of this theory is that the adsorption of hydrogen is resulting in the decrease in surface energy for the formation of fresh crack surfaces and that the existence of a crack where the hydrogen is adsorbed. Due to this decrease, the crack can more easily propagate. In other words the crack can propagate under lower mechanical load.[6]

2.4.5.7 Hydride theory

The hydride theory is based on the formation of brittle hydrides which facilitates the propagation of a crack. This theory has almost no relevance for DSS since the stable hydrides for the applications described in the first chapter are the transition metals in V periodic group, such as Nb, V, Ta, Zr, Ti and Mg. These elements can interact with hydrogen to form metallic hydrides, whereas the common elements in DSS (e.g. Fe, Ni, Cu, Cr and Mo) can interact with hydrogen to form only a metal-hydrogen bond. Nevertheless, the hydride mechanism is based on the diffusion of hydrogen to regions of high hydrostatic stresses (i.e. ahead of crack tip). The high hydrogen concentration contributes to the formation of hydride resulting in a cleavage of the hydride after reaching a critical size. Noteworthy is that this mechanism can occurs in well-defined regime (in means of temperature and mechanical load) were the hydrides are stable therefore under extreme conditions also Fe can form hydrides however this is not the case here.

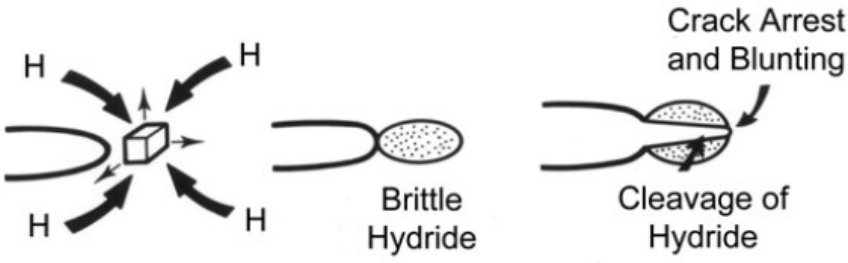

Figure 2-17: Schematic diagram illustrating the formation and fracture of brittle hydride at the crack tip.[70]

2.5 Hydrogen isotopes – properties and uses

Hydrogen is the isotope with the highest abundance out of the three isotopes: protium (i.e. hydrogen) deuterium, and tritium. Although in different abundances, hydrogen and deuterium are considered as stable isotopes unlike tritium (which decays into He). All the three isotopes of hydrogen are frequently used for the investigations of hydrogen assisted cracking of metals especially for local distribution imaging (as distinguishable tracers for hydrogen). Therefore it is necessary to give a detailed introduction to the differences between these isotopes and the use of them in those experiments.[126] Hydrogen is commonly used in general quantification approaches such as by mass spectrometry and carrier gas hot extraction methods.[127] One example where the necessity to use deuterium instead of hydrogen was shown by Straub et al. [128] for local ToF-SIMS analyses. It was shown in this work that although the material was deuterated, the adsorption of hydrogen at the surface before and during analysis interfered the imaging process due to strong homogenous distribution at the surface as shown in Figure 2-18. Tritium was used by Saintier et al. [129] to observe the mobility of hydrogen (tritium) by dislocations under external mechanical load.

Some of the physical properties of the isotopes are listed in Table 3 for comparison. On earth, hydrogen and its isotopes can exist in the molecular state, dissociated as ions in electrolytic mediums or in the atomic state in elevated temperatures.

Table 3: Physical properties of hydrogen isotopes[54]

	^{1}H Hydrogen	**^{2}H Deuterium**	**^{3}H Tritium**
Nuclear mass	1.000	2.014	3.016
Abundance	99.98%	0.02%	10^{-18}
Radioactive stability	Stable	Stable	$^{3}H \rightarrow \beta^{-} + {}^{3}He$ (half-life decay: 12.32 years)

All isotopes have the same chemical properties however, when considering the degradation of steels by high concentrations of hydrogen in the metallic lattice, the impact of the dissolved ion size in the lattice and in traps can be quite significant.

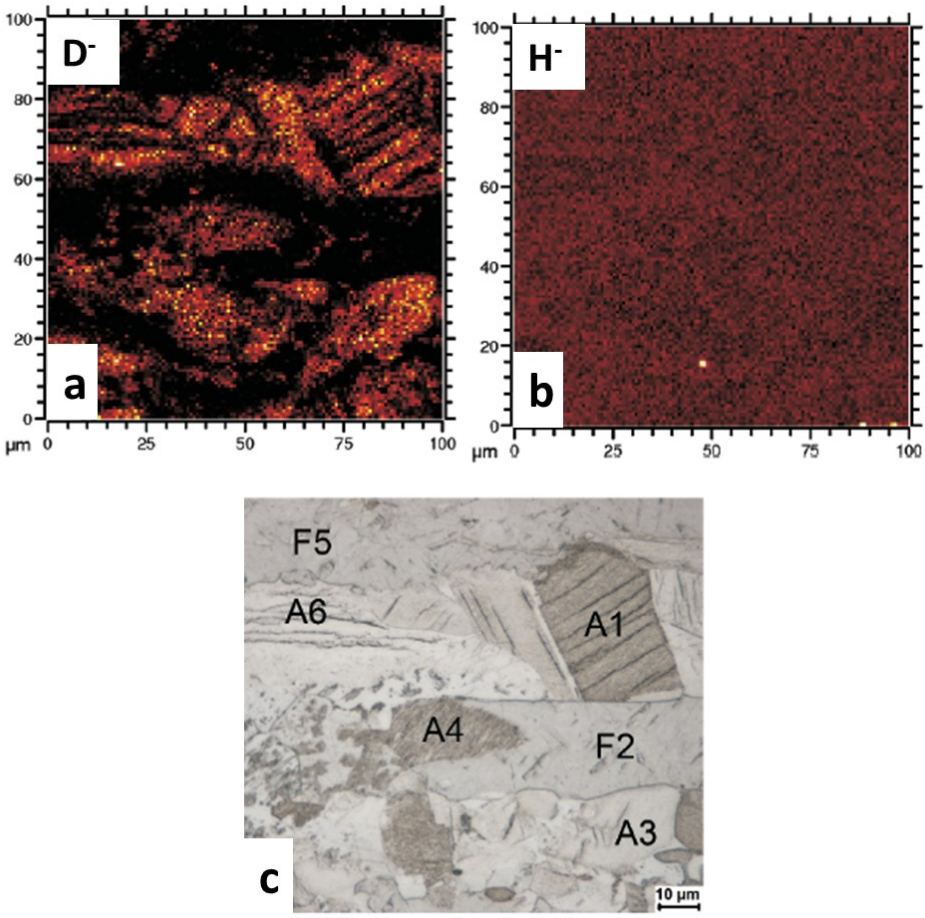

Figure 2-18: ToF-SIMS images of a) deuterium and b) hydrogen distribution at the surface of an electrochemically deuterated DSS 2205 sample and c) OM image of the same ROI (A and F stand for austenitic and ferritic grains respectively).[128]

Due to the fact that some of the degradation processes are pronounced by the internal strains applied by the dissolved atom it is necessary to take the mass/size of the dissolved atom into consideration in the interpretation of the results. The three most significant factors that must be taken into account are permeability, diffusivity and solubility. There is a large number of publications where those factors are experimentally examined and theoretically calculated and compared. For iron, all comparable values (starting from the permeation activation energy, the solubility values of hydrogen and deuterium, and the effective diffusivity) are differing in the same order of magnitude. In the more recent literature[130] the classic isotope effect is assumed. The meaning of the classic isotope effect refers to the

ratio of the diffusivity coefficients of hydrogen isotopes which is equivalent to the inverse ratio of the square root of the masses of the isotopes, as shown in the following equation:

$$D_H/D_D = (m_D/m_H)^{0.5} \quad (11)$$

where D is the diffusivity and m is the mass of the respective isotope. The subscripts H and D refer to hydrogen and deuterium, respectively.[130] From this expression the following relation can be developed:

$$D_H = \sqrt{2}D_D = \sqrt{3}D_T \quad (12)$$

where the subscript T refers to tritium. The relationship between the isotopes is based on the classical rate theory where the relation between the diffusivity and the atomic vibrational frequencies of the interstitial atom in the lattice are inversely proportional to mass.[130] The activation energy for diffusion is assumed to be independent of the mass of the isotope.[130] The simplified relation can be assumed for ambient temperature and for Ni[131] and stainless steels[132-135] unlike other metals[136] where this assumption cannot be applied. Figure 2-19 shows some of the materials where the diffusion behavior of the three isotopes differs in different temperatures. Nevertheless, this subject is still under debate with the claim that these values must be calculated separately for each case. For instance, Kumnick et al. [137] showed by electrochemical charging of pure iron that the diffusion coefficients ratio between hydrogen and deuterium D_H/D_D is ~1.8 for a temperature range of 9-73°C as it is shown in Figure 2-20. This result indicated on a greater value than the classical ratio of 1.41. Moreover, Raczynski[138] showed that for pure iron, in the range of 10 to 60°C, gaseous charging in a pressure of 0.1MPa, the D_H/D_D ratio is temperature-dependent and varies between 1.8 at 60°C and 2.05 at 10°C. These values are also greater than the square root of the mass ratio and much greater than the value of 1.2 which was observed in temperatures above 100°C. Another issue that must be taken into account in the use of tritium is its decay into He.[63] This process produces bubbles and blisters in the material discarding the hydrogen induced degradation. Clearly, the strong influence of fundamental parameters such as: material properties (e.g. high purity, alloy), type of charging (e.g. high pressure gas or electrochemical), experimental setup (e.g. sample's surface finishing, current density, electrolyte composition, etc), temperature, make it impossible to deduce a clear general conclusion.

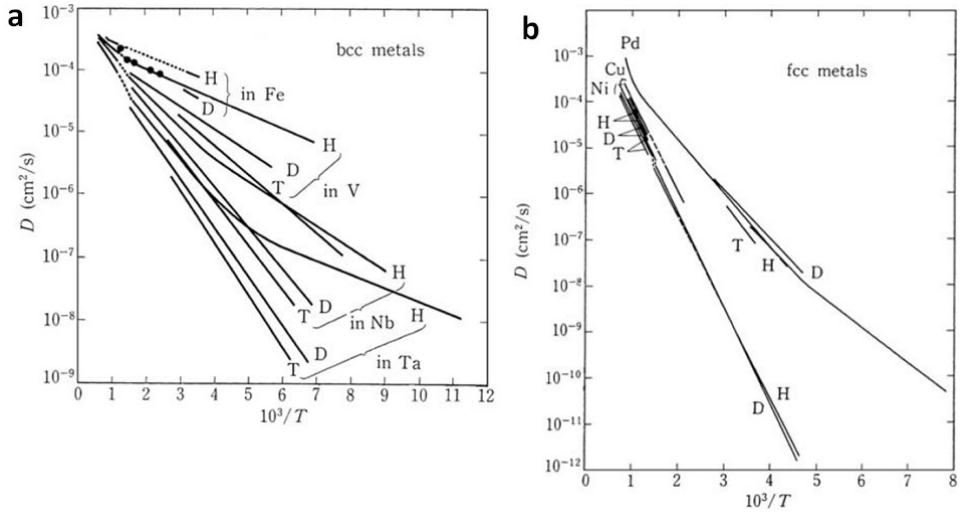

Figure 2-19: Diffusivity of Isotopes in different temperature in a) bcc metals and b) FCC metals.[54]

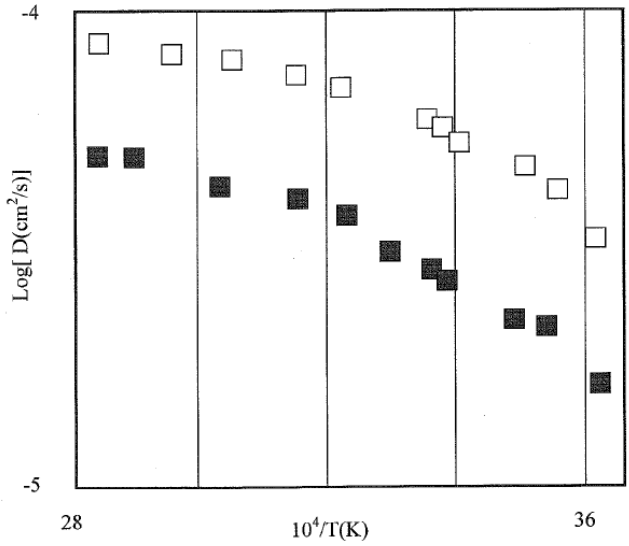

Figure 2-20: Diffusivity of Isotopes in high purity Fe (open squares: H, filled squares: D)[137]

2.6 Methods for characterization of hydrogen related degradation (macro-quantitative and microscale methods)

As described in chapter 1.4.4 there are several models that are used in order to explain the embrittlement of steels by hydrogen. The models are relying on, in most cases, the conventional approach. This approach consist of hydrogen sensitive macro-scale methods (such as Thermal desorption spectroscopy, carrier gas hot extraction, etc., for the general quantification of hydrogen concentration), methods used to test the mechanical properties and posterior non sensitive sub-micron scale topographic and structural observations (mainly by optical and/or electron microscopy). In the last 50 years many direct methods for local observations on the hydrogen distribution were developed. The following chapter is divided into the two parts, the conventional approach and the innovative methods. In each of the following parts the macro-scale and the micro-scale are explain. More attention is given to the microscale techniques with special attention to the Secondary Ion Mass Spectrometry due to its relevance to this research. However, before starting it is necessary to clarify four terms eliminate any confusion: structure, microstructure, direct and indirect analysis/method. The term structure stands for any crystallographic related subject, from crystal structure and symmetry to lattice defects (i.e. dislocations, stacking faults, etc.). The term microstructure refers to any observable feature, not only by visible light (e.g. phases, preferred orientation of the grains, cracks, etc.). Some of the features can be related to both terms (e.g. twins, boundaries, etc.). The other two terms refer to the characterization process. Direct method is a method where the results indicate directly on the character. For instance, the use of Bragg based scattering methods (e.g. XRD, ED, etc.) for indicating on a structural feature. EDX, for example, cannot indicate on any structural feature, the same way XRD cannot indicate on any chemical feature but only structural.

.

2.6.1 Conventional macroscale quantitative methods

The development of methods to measure the absolute hydrogen contents in metallic materials has begun in the previous century. The general quantification of hydrogen can be conducted in the solid state as well as after melting the material. In order to quantify the hydrogen concentration the dissolved/trapped hydrogen should be released from the material either by giving sufficient time for effusion at ambient temperature or by supplying heat and sufficient energy to accelerate the process. After it is released, the effusing hydrogen is carried to the detector by gaseous or liquid medium or in vacuum, the carrier medium (especially if it is gas) must be inert to the hydrogen and must have different

physical properties (e.g. different heat conductivity). In this way the quantification by the analyzer can differentiate the based on a chemical or physical principle of operation.[139]

One of the first approaches that were developed to deliver the hydrogen in ambient conditions is based on the mercury method (ISO 3690).[139] The mercury method was the standard procedure to determine the amount of diffusible hydrogen. The quantification was fulfilled by placing the specimen into an evacuated chamber. The hydrogen is collected for 72 hours at room temperature. The recombination of hydrogen and the formation of molecules results a change of the pressure in the chamber that can be measured by liquid mercury. The main disadvantage of this approach is the health risks of using mercury and therefore this method is less common nowadays. Unlike the mercury based measurements hydrogen-hot extraction based methods are more common nowadays. These approaches are based on providing heat for the thermal activation of the hydrogen atoms in the lattice for desorption of the atoms. The hydrogen recombines to molecular gas and collected from the chamber. The collection can be obtained by vacuum hot extraction method (VHE), carrier gas hot extraction method (CGHE) where the hydrogen is collected by a continuous flow of a high purity inert gas (such as nitrogen) or by melt extraction. The melt extraction can also be performed after applying the previous methods; however, this melting does not allow any further investigations. After the collection, the quantification is obtained by thermal conductivity device (TCD) which is based on the comparison of the thermal conductivity of the examined gas mixture compared to the pure carrier gas. The main disadvantages of the TCD are the detection limits and resolution. This issue is solved by determination of hydrogen with mass spectrometry (MS). [127, 140, 141]

The procedures described above are used for the quantification of hydrogen in the sample. However, determination of hydrogen permeability and diffusivity is obtained by a different method. Hydrogen diffusion characteristics around ambient temperature are determined by an electrochemical method based on the Devanathan-Stachurski approach.[142] This type of experiments are conducted on an electrochemical double cell divided by a membrane. The membrane consists of the examined sample. The double cell consists of hydrogen generating cathodic part and hydrogen oxidizing anodic part. The measured current indicates directly on the ion transport through the membrane from one cell to the other.

2.6.2 In-direct observations of hydrogen assisted cracking

As mentioned previously, the assumptions and theories for explaining hydrogen assisted cracking are based on combining macroscale hydrogen quantification method with micro scale topographic observations. OM, TEM and SEM are the most common microscopic

techniques in this approach. These tools can indicate a change in the structure, topographic changes or the fracture character. However they cannot indicate on any local hydrogen concentration. The literature contains a huge number of publications however the outstanding ones are those where these methods were applied during in-situ processes. One of the most familiar examples is the in-situ experiment made by Birnbaum et al. [143] inside a TEM after introducing some modifications to allow gas flooding and creating a gaseous hydrogen environment around the sample. During the experiments a gas pressures of up to 20 kPa was obtained. The experimental setup allowed analyzing how the introduction of the gas during mechanical loading changes the dislocation mobility. It should be taken into account that the electron beam increases the fugacity of hydrogen by few orders of magnitude and therefore the dissociation and ionization of the H_2 molecule is much higher.[144] This experiments were applied on several metals during the 1990s. These experiments provided the first in-situ evidence for the existence of the HEDE and HELP mechanisms in the sub-micron scale.

In the recent years the field of electron and ion microscopy is experiencing a major progress in means of resolution and experimental setup. The use of FIB milling takes a major part in the recent progress by decreasing the size of the samples to enable in-situ experiments as it was shown by Hajilou et al. [145] (Figures 2-21 and 2-22).

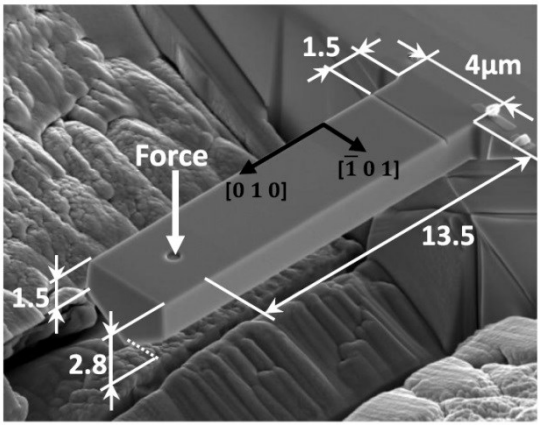

Figure 2-21: Dimensions of one representative tested cantilever in the In situ electrochemical microcantilever bending test[145]

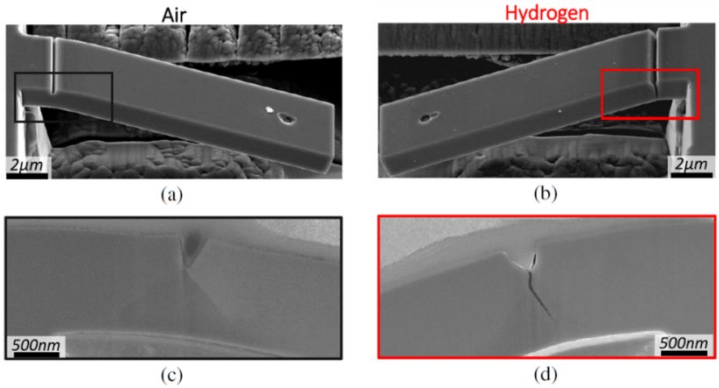

Figure 2-22: Representative SEM images of the H free (a) and H charged (b) cantilevers bent to a displacement of maximum 5μm. SEM images of cross sections of the marked areas in (a) and (b) are shown respectively in (c) and (d). [145]

This group has shown combined hydrogen charging and mechanical loading experiments. By the experimental setup, dislocations nucleation and pinning at the crack tip in Fe–3wt% Si samples were revealed. The innovation in those experiments was in the sample preparation by FIB milling that enabled to produce single crystalline microcantilevers. Therefore, it was possible to characterize the degradation process. This experimental setup allowed analyzing the type of fracture and further TEM and EBSD measurements (as shown in Figure 2-22). The samples were compared with samples bent in air.

In-situ imaging of hydrogen assisted deformation have also developed in the last decade. Among the different indirect approaches AFM was also used recently for imaging during electrochemical charging. Barnoush et al. [146] showed that electrochemical charging of super DSS with hydrogen contributes to the formation of slip lines at the surface of the austenitic phase. The irreversible deformation of the austenite is shown in Figure 2-23. Clearly, the progress with indirect methods is significant. Still, in order to advance the field – direct indications are required. None of the available indirect methods can locate and measure the concentration of hydrogen at key microstructural features. The indirect approaches are limited with local analyses of the hydrogen diffusion for instance along interfaces and grain boundaries.

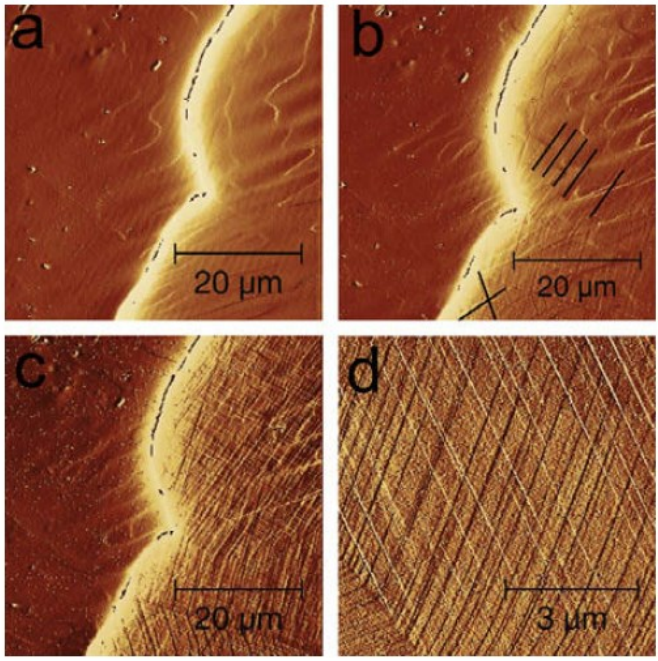

Figure 2-23: Barnoush in-situ experiments on AFM images form the surface of the sample during in situ electrochemical H-charging. Before H charging (a), after 1 h (b), 2.5 h (c) and higher magnification image from the surface of the austenite grain (d). On the left is a ferrite grain and on the right is an austenite grain which can be distinguished by its convex grain boundary.[146]

2.6.3 Direct observations and mapping of hydrogen distribution – hydrogen sensitive methods

There is a rather small number of advanced techniques for the detection of hydrogen at the microscale.[82] The available techniques can be divided into two groups, the first group offers outstanding resolution at the nano-scale, e.g. atom probe tomography (APT)[147], but is strongly limited with applying in-situ experiments due to the complicated instrumental set-up and sample geometry requirements, the second group offers lower resolution in the sub-micron to micron-scale but allows more flexibility with the experimental set-up and therefore enables in-situ experiments e.g. neutron tomography (NT)[119]. The advanced method exist nowadays, the maximal resolution and the major achievements are listed in Table 4. Note that Time-of-Flight Secondary Ion Mass Spectrometry is not listed in Table 4. This method is explained in details in chapter 2.6.4

As shown, the resolution varies in a wide range between these methods. Investigations of hydrogen trapping in the crystalline materials is intensively studied with several other methods such as thermal desorption spectroscopy[148, 149], nuclear reaction analysis[150] and elastic recoil detection[151]. However, these methods provide only bulk-averaged information on microstructural interaction with much lower spatial resolution, and the direct interpretation from these signals can be difficult.[147] Moreover, in order to obtain reliable results, in most of the listed methods, especially APT, hydrogen must be replace with deuterium in order to be able to distinguish the adsorbed hydrogen from the intentionally introduced one.

On the other hand, hydrogen microprint technique (HMT) delivers reliable results on the sub-micron scale by the use of hydrogen and not deuterium. Moreover, this method was also applied to in-situ permeation analyses of low carbon steel and showed that the main diffusion path in this type of steel was lattice within grains.[71] Nevertheless, this method requires coating of the analyzed surface with the hydrogen sensitive film (AgBr) and sometimes with additional layers. The coating hinders the characterization of the microstructure, and more important – makes it impossible to proceed with additional experiments (e.g. electron backscattered diffraction).

The clear conclusion here is that as resolution becomes better the sample preparation and the experimental setup becomes more and more difficult. According to the needs of the scientific community the ability to map and even quantify the hydrogen distribution in precipitates[152] and atomic defects such as dislocations and vacancies is possible by

APT. Takahashi et al. [147] have shown recently by this method the distribution of hydrogen within the core of V-Mo-Nb carbides in a low-alloyed ferritic steel (Figure 2-24).

Table 4: Summary of direct methods for hydrogen mapping[82]

Method	Resolution and requirements	Experimental achievements
Ag decoration / Hydrogen microprint technique (HMT)	Sub-micron with electron microscopy. Surface must be covered with Ag containing emulsion. Further analyses are difficult.	These methods were applied in-situ to monitor hydrogen permeation.[71] In addition, ex-situ HMT was applied to observe the effects of stress and deformation on segregation of hydrogen.[153]
Scanning Kelvin probe (SKP)/ Scanning Kelvin probe force microscope (SKPFM)	Few tens of micrometers. Palladium must be used in order to enhance the sensitivity to hydrogen and enables reliable mapping of hydrogen activity.	This method was used in order to correlate the crystallographic orientation of grains in γ-SS to the hydrogen diffusivity.[69]
Atom probe tomography (APT)	Sub-nano (up to one billion atoms). Very difficult sample preparation due to specific geometry of the sample.	This is the only direct method where hydrogen can be mapped in the atomic scale.[147]
Neutron radiography	20-30 micrometers. No sensitivity to composition or microstructure.	This method was used to observe the enrichment of the cracks surfaces with molecular hydrogen and surrounded by a 50μm zone with a high hydrogen concentration.[119]

The use of APT enabled to obtain a quantitative composition profiles. Haley et al. [154] concluded that deuterium is more useful for indicating microstructure-related effects by comparing deuterium and hydrogen distributions in Ag. APT offers the best resolution for the detection of hydrogen.[152, 155] however this method requires very specific sample preparation and in-situ permeation or mechanical load is inapplicable.

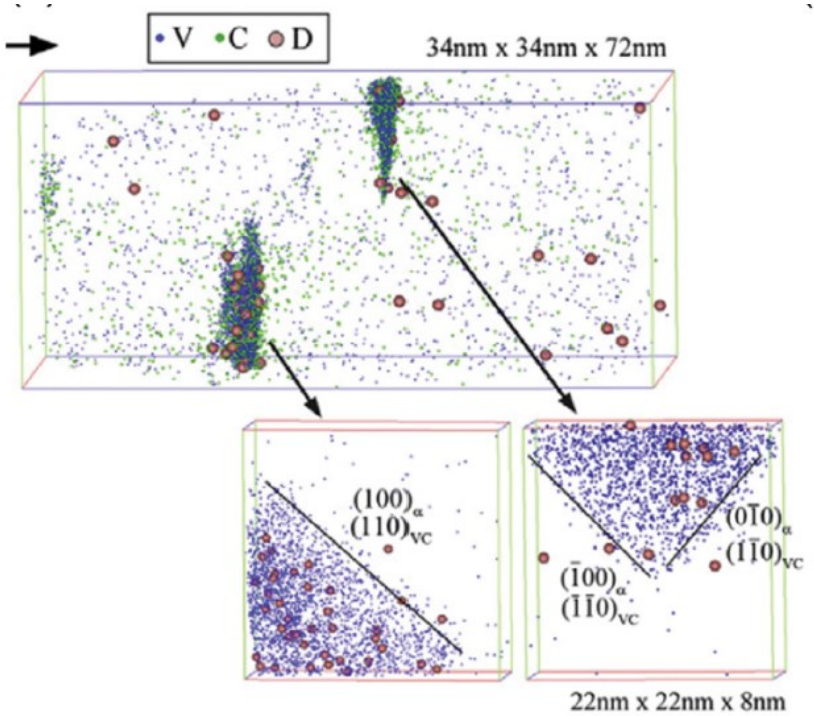

Figure 2-24: Takahashi APT experiments – 3D elemental maps of the peak-aged steel sample with deuterium charging revealing the deuterium distribution at a VC precipitate.[152]

On the contrary to this method, NT offers the best flexibility for in-situ experiments.[119] However the reachable resolution varies in the range of 20-30µm in the best case. Still, this method can provide three-dimensional direct information about the distribution of hydrogen around cracks (Figure 2-25). One example for these observations was shown by Griesche et al. [119] who showed hydrogen-stimulated cracks and blisters and the related hydrogen distributions in an ARMCO™ iron. In this work the electrochemical charging process induced formation of cracks and blisters. The cracks were surrounded by a 50µm area that contained up to ten times more hydrogen than the bulk (Figure 2-26).

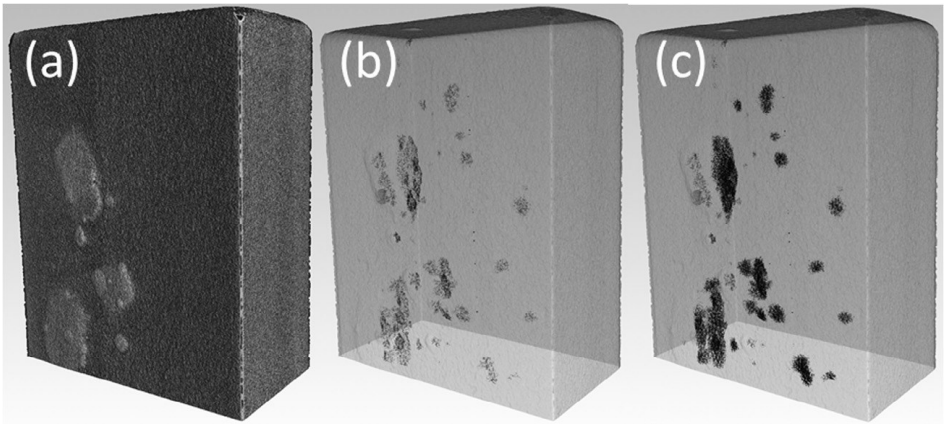

Figure 2-25: Inclined view on the reconstructed 3-D model of a hydrogen-charged iron sample, the raw data is produced by neutron tomography. The surface with blisters is shown in (a). The crack distribution in the interior is presented in (b) and the additional hydrogen distribution in (c).[119]

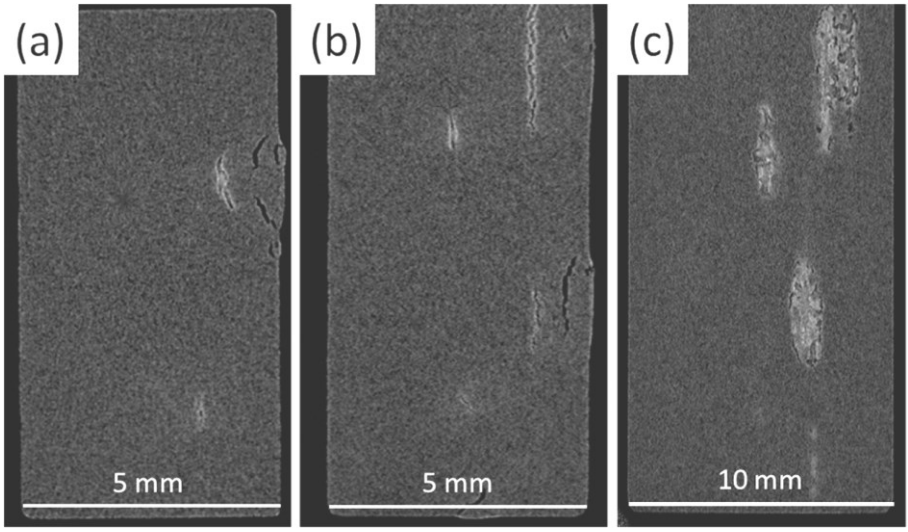

Figure 2-26: Three orthogonal slices taken from arbitrarily positions in the reconstructed 3-D model: (a) xy-plane, (b) yz-plane, (c) xz-plane. The data is produced by neutron tomography.[119]

2.6.4 Direct observations and mapping of hydrogen distribution by Time-of-Flight Secondary Ion Mass Spectrometry

Secondary ion mass spectrometry (SIMS) in terms of resolution, is located between APT and NT. The principle of SIMS is the generation of secondary ions by impacting high energy primary ions which causes a collision cascade within the near surface atomic layers of the investigated area. As a result, atomic and molecular fragments are produced and may leave the surface[156] as shown in Figure 2-27.

There are two modes of SIMS analysis, the dynamic and static ones. Both of them are used in the last decade for investigations of deuterium interactions in steels. In dynamic SIMS the primary ion flux is aggressively eroding the surface and resulting in high sensitivity for trace elements. The ToF-SIMS can work in both ways dynamic and static SIMS, however in the current work it was used mainly in the static mode. In this mode the secondary ions originate exclusively from non-damaged areas. By the so called “static limit” of 10^{12} primary ions per cm^2, the low primary ion flux density statistically guarantees that every primary ion hits a non-damaged surface. Nowadays, the static mode is mostly executed by using ToF-SIMS instruments with the capability of parallel mass detection and high transmission of the Time-of-Flight analyzers.[156]

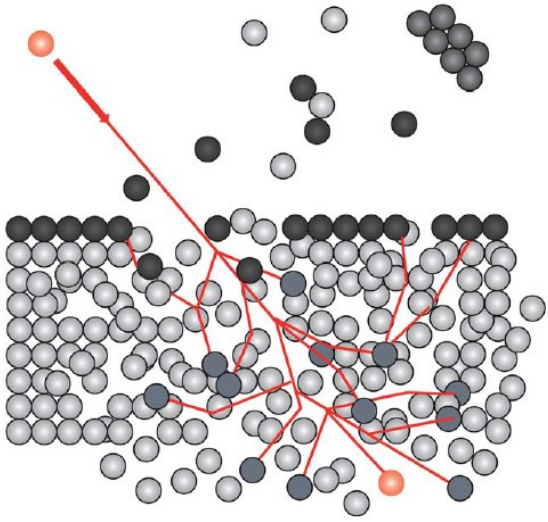

Figure 2-27: Collision cascade in a solid sample covered by a monolayer initiated by the impact of an energetic primary ion (red).[157]

For the ToF-SIMS the energy of the primary ions is transferred to the constituents of the solid. As a result of this the bonds are broken and particles leave the bombarded surface due to momentum transfer.[157] The majority of the sputtered material is not charged and therefore cannot be extracted by the Time-of-Flight (ToF) analyzer. The charged portion (less than 1% of the sputtered material) is analyzed by the mass spectrometer. In the ToF-analyzer the secondary ions are accelerated in an electric field and are distinguished, after a drift path, according to their flight time. The operation principle is shown in Figure 2-28.[158] According to the equation of kinetic energy, the measured flight time (t) can be converted to mass-to-charge ratio by using the following equation:

$$2\frac{Ut^2}{L^2} = \frac{m}{z} \tag{13}$$

were U is the applied voltage of the extraction electrode, L is the drift length and m/z is the mass to charge ratio.[159]

The lateral resolution of the ToF-SIMS instrument, which is essential especially in the case of imaging, is determined by many factors, including: primary ion beam spot size, mass resolution, signal intensity per pixel, instrument stability (mechanically and electrically), scanning step-width and the dimensions of the collision cascade induced by the primary ion beam in the respective material. In ToF-SIMS, mass resolution and lateral resolution have opposite requirements. Therefore, in each case the best overall resolution is a compromise between a few factors, most significantly, the primary ion beam.[159] There are different default modes of operating the primary ion source, differentiated by pulsing cycles. The pulse time defines the mass resolution; the shorter the pulse, the higher the mass resolution in the spectra. By “bunching” primary ion pulses (as in high-current bunch mode – HCBU), a high mass resolution with narrow peaks can be attained, but with a lateral resolution of only 2-5µm. In order to achieve submicron lateral resolution, the primary ion gun is operated in a non-bunched mode, using longer pulse times of primary ion bombardment. This imaging or burst alignment (BA) mode allows for much better lateral resolution and results in a degraded mass resolution.[160] In the BA mode the peaks appear broader and therefore, overlapping is inevitable.

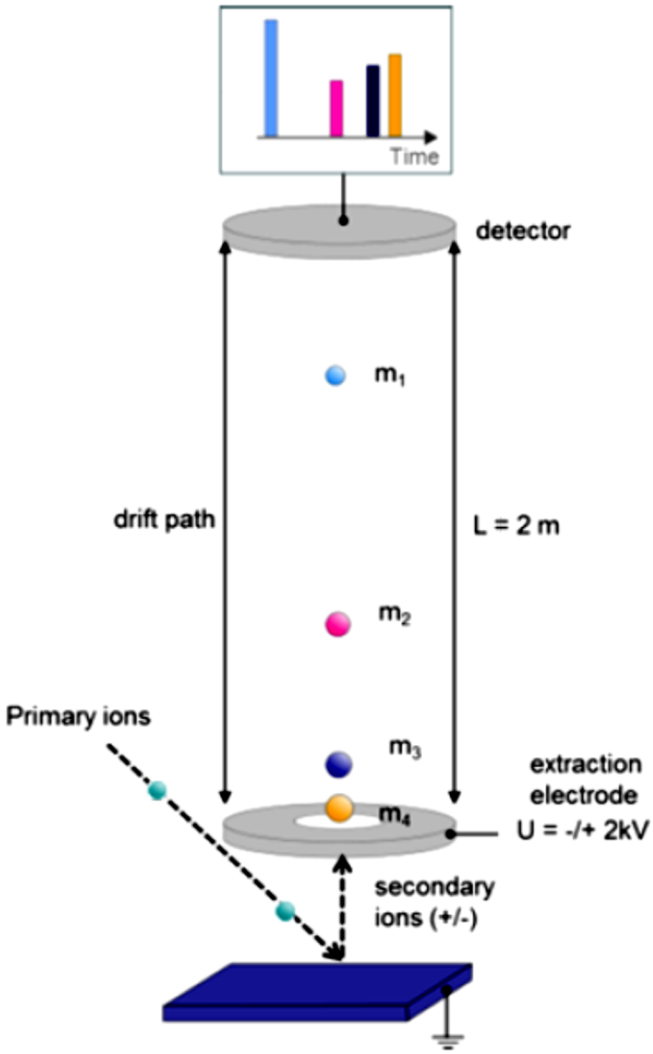

Figure 2-28: The principle of the Time-of-Flight detector allowing mass dispersion in a drift path where $m_1 < m_2 < m_3 < m_4$.[158]

In addition to these default modes, Holzlechner[161] and Kubicek[162] have shown recently a special alignment of the BA mode to obtain a spatial resolution of below 100 nm and a better mass resolution (sharper peaks) but still not comparable to the HCBU. The initial use of SIMS for investigating hydrogen distribution in steels was already in the early 1980s by the group of Birnbaum [163-166]. The analyses were carried out by dynamic SIMS, which was used for acquiring low spatial resolution spectra.

The first outstanding use of SIMS for hydrogen mapping was reported by Oltra et al. [167] in 1994. In this work, dynamic SIMS was used to chemically image the distribution of deuterium (^{2}H) in a DSS microstructure after SSRT tests, with a spatial resolution of ~1µm as shown in Figure 2-29. The disadvantage of dynamic SIMS is the rapid erosion of the surface and the formation of significant topographic changes within a short time, which influence the reliability of the data.

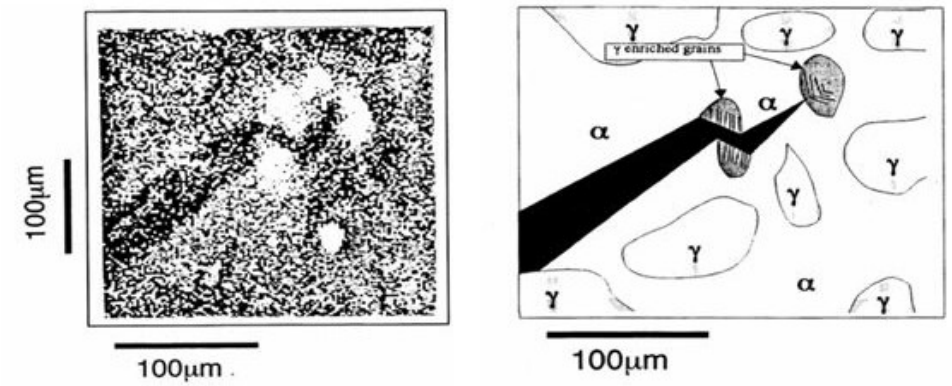

Figure 2-29: Oltra's experiments with imaging dynamic SIMS: The image (left) and the schematic overview (right) show the high concentration of deuterium in the austenitic grains in a DSS after strain tests in deuterated environments (gaseous and aqueous).[167]

In recent years there is an increasing number of publications where SIMS is used as the major tool for mapping of hydrogen on the micro-scale[72, 168]. Similarly to the conventional approach of applying several complimentary techniques, the trend here is also to combine SIMS with complementary methods in order to correlate the total hydrogen concentration, the local hydrogen distribution and the hydrogen enhanced structural and microstructural changes in the material.[69, 126, 145] Oudriss et al. [90] have shown the combination of ToF-SIMS with EBSD to study anisotropic hydrogen segregation and diffusion in nickel polycrystalline structure. The results indicated that the hydrogen distribution in a polycrystalline pure nickel depends mainly on the grain boundaries character.

One of the biggest advantages of this technique for studying steels is that the ToF-SIMS, has a parallel mass detection capability at sub-µm lateral resolution, which enables both detailed imaging of the microstructure and analysis of the chemical composition.[169] For instance, Straub et al. [169] showed a valid phase identification in the microstructure of a 2205 DSS, particularly by using Cr^+, Fe^+, Ni^+ and $CrFe^+$ secondary ion yields to distinguish

between the phases. Izawa et al. [168] have investigated the formation of the oxide surface layer on austenitic stainless steels and evaluated the probability of the formation of α' martensite. Table 5 presents the most significant experiments during the development of the SIMS to produce both images and spectra in the field of hydrogen induced degradation of metals.

Table 5: Summary of SIMS analyses for investigations of hydrogen enhanced degradation

Source	Year	Type of charging	H/D	Analysis type	Mode
[170]	1982	Electrochemical	D	Ex-situ depth profiling	Dynamic
Application and content of paper: concentration profile in strained and unstrained regions in an AISI 302 alloy					
[171]	1994	Electrochemical	H	Ex-situ spectra	Dynamic
Distribution of hydrogen in the vicinity of a crack tip under different bending loads of a 0.3% C, 1.0% Cr, 1.1% Mn, 0.9% Si steel					
[172]	1995	tensile test in aqueous solution	D	Ex-situ depth profiling and imaging	Dynamic
Hydrogen and deuterium trapping sites. Accumulation at grain boundaries, in segregation bands and on inclusions in a low-alloyed steel					
[173]	2003	Immersion in aqueous solution	H, D	Ex-situ imaging	Dynamic
Visualization of hydrogen desorption in a spheroidal graphite cast iron					
[174]	2009	Gaseous	H	Ex-situ depth profiling and imaging	Dynamic
Fatigue test in gas environment in a AISI 304					
[72]	2014	Electrochemical	D	Ex-situ depth profiling and imaging	Static
Visualization of hydrogen desorption in both 2205 DSS and Ni base alloy					
[175]	2014	Gaseous	H	Ex-situ depth profiling	Dynamic
Time variation of the distribution of hydrogen in a 316L stainless steel.					

3 Objectives of the study

3.1 Statement of the problem

Considering the lifetime of an engineering component, while in service it is exposed to both hydrogen (e.g. as a result of cathodic protection in marine applications) and a load, which results from the common use of this component (e.g. internal pressure of the delivered medium in a pipe system, routine shutdowns, etc.).

The evaluation of the degradation of steels by hydrogen has been a topic of study for more than 100 years. Despite all efforts, the understanding of this phenomenon is still limited in the academic community. There are still many questions about the whole process from the source of hydrogen, generated by electrochemical reaction or by the adsorption of hydrogen gas molecules to the surfaces, followed by dissociation and diffusion through the steel and eventually how hydrogen atoms interact with the material microstructure and existing microstructural traps. All existing theories and models are based on the assumption that under sufficient loading, hydrogen is transported in the microstructure mainly through the interaction with and the movement of dislocations. It is assumed, but so far never shown, that the strain fields around cracks are subjected to the highest hydrogen concentration supplied from internal and/or external sources. A higher hydrogen concentration in front of a crack leads, not only, to the activation of the atomic mechanisms (HEDE and HELP) but also, in the case of austenitic phases, to transformation into a brittle phase that facilitates crack propagation, as mentioned earlier.

The following conclusions can be drawn by reviewing the literature:

- There is no single method that can solely deliver the information that is needed for better understanding. Only in recent years are research groups worldwide combining more than one method in order to cover the degradation process comprehensively. Hydrogen is affecting the structure and microstructure and therefore in order to obtain a better overview of the problem, three methods must be used: chemical sensitive, microstructural – topographical and structure sensitive method. This combination can contribute to a better understanding of HELP and HEDE mechanisms.
- ToF-SIMS belongs to the multivariate data producing method. Imaging processing with ToF-SIMS is an even more complicated process, where the data capacities are enormous. This type of method requires data treatment to maximize the extracted information from the raw data. Although there is increasing attention on

ToF-SIMS, up to the present no appropriate data treatment and/or normalization were applied to the raw data (which in some cases was essential in order to eliminate artifacts).

- Use of several methods requires the ability to combine the data. One approach that has been applied in recent years, in all fields except in the field of hydrogen assisted cracking investigations, is called data fusion.
- As mentioned before, there are three factors that control the hydrogen assisted cracking process: microstructure, hydrogen concentration and mechanical load. Despite the outstanding progress in the development of experimental approaches, no in-situ direct indication of strain induced hydrogen transport in the material was shown at the microscale.
- Similar to the previous point, there is a countless number of publications where hydrogen transport, diffusion and permeation through ferritic, austenitic and DSSs were simulated and conducted in the macroscale. However, to understand the role of grain (and phase) boundaries, in-situ/in-vitro local observations of these phenomena are, qualitatively and quantitatively, still missing.
- The austenitic phase in DSSs differs in the stability of the phase under strain depending on the alloying elements content. The strain can be induced by external loads and by the diffusion of hydrogen into the microstructure in large quantities. The transformation takes place in two structures: BCT/BCC or HCP. Up to the present there is no direct indication for the relationship between local hydrogen concentration and the resultant phase.
- Despite the complexity in investigating the hydrogen assisted degradation process of a DSS microstructure there is a large number of publications, however, very few of them use direct methods to indicate the behavior of the hydrogen concentration on the microscale.

3.2 Special objectives

The present study cannot answer all open questions mentioned above. Thus, the goal here is to examine some of the existing mechanisms and theoretical models by the development of new in-situ and ex-situ experiments (Figure 3-1), allowing observation of the hydrogen on the microscale. Specifically the following three subjects were examined in order to overcome the gaps defined above:

I) The distribution of hydrogen in a DSS microstructure

II) Ductile to brittle transition of HAC

III) The interaction of hydrogen in regions of high stresses/strains

The research is based on a proof-of-principle that has been delivered already in the literature, proving that observation of hydrogen in the microstructure by ToF-SIMS as the main method is feasible. During this research the use of complementary techniques to correlate the hydrogen distribution with structural and microstructural changes was established and developed. Data fusion approaches (topography by SEM with chemical image data by ToF SIMS), including multivariate data analysis, will be tested as part of the implementation of complementary techniques. The main experimental challenge in the research is the development of new in-situ experiments inside the ToF-SIMS machine to get beyond the existing state-of-the-art.

The project was designed to investigate the following four central questions:

- What is the influence of N and Ni on the susceptibility of the austenitic phase to hydrogen induced martensitic transformation?
- What is the role of phase and grain boundaries in dual phase alloys with regard to hydrogen trapping?
- How crack initiation and propagation depends on hydrogen concentration and phase properties?
- Is it possible to observe hydrogen migrating into strained regions by internal stress and mechanical load induced diffusion?

The experiments will be conducted by using two highly relevant types of steels: standard duplex stainless steel (DSS) and lean duplex stainless steel (LDX). The selection of the standard grade stemmed from frequent use in many industrial applications where the risk of hydrogen assisted cracking is an important issue (as shown in the literature review). The LDX was selected due to the fact that this grade is considered a proper replacement for the

high Ni-content DSSs. The use of these two grades can provide a better understanding by performing a qualitative comparison. In addition, these two grades are suitable for studying the austenitic phase susceptibility to hydrogen assisted cracking due to the variation of the N and Ni content.

It should be noted here that the proposed experiments are conducted using the hydrogen isotope deuterium (^{2}H/ D). The reason for this is the difficulty to distinguish the relevant hydrogen in artificially charged steel samples from the adsorbed ambient hydrogen species in the analysis chamber of the SIMS instrument. Many investigations have been carried out on permeability, diffusion coefficients and solubility of hydrogen in stainless steels in comparison with deuterium, which shows there are only small differences between both hydrogen isotopes [130, 172]. For D and H, the values of the diffusion coefficients are in the same order of magnitude. [54, 130, 132, 176]

The project consisted of three central experiments:

Ex-situ – static experiments: These experiments are designed first of all to elucidate the distribution of deuterium in a DSS microstructure. In addition, these experiments can reveal parameters such as deuterium mobility as a function of the sample temperature and determination type of transformed austenite. Furthermore, information on the impact of charging on the phase stability when the surface is directly exposed to the electrolyte, the relationship between deuterium concentration and phase transformation and the apparent degradation of the steel sample can be gained.

In-situ – mechanical loading experiments: These novel experiments are aimed at in-situ elucidation on the deuterium-steel interactions under varied mechanical loading conditions, specifically the assumed enrichment of deuterium around the region of high stress state by imaging ToF-SIMS (Figure 3-1).

In-situ – deuterium permeation experiments: This novel in-situ approach to study the deuterium permeation (Figure 3-1) through a steel membrane in a charging cell (produced from a single piece of steel) during ToF-SIMS imaging is conducted only on a 2205 DSS sample. The experiment is a kind of a Devanathan-Stachursky permeation experiment where the deuterium detection at the exit surface is “replaced” by the ToF-SIMS instrument.

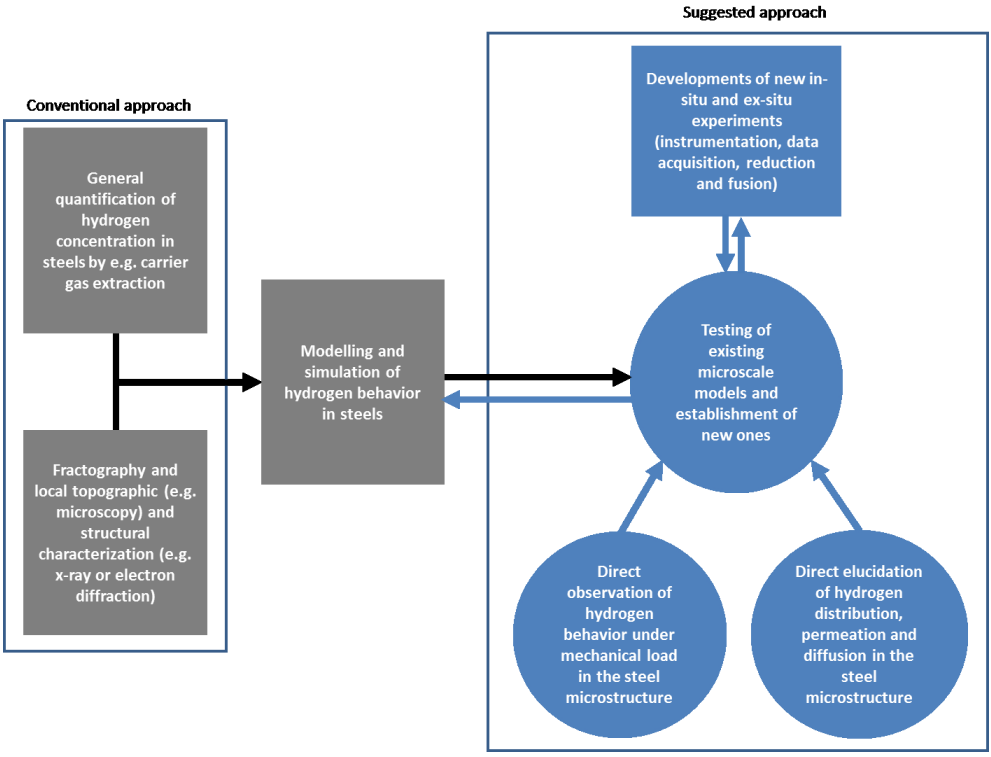

Figure 3-1: Survey on the existing and the new approach to build and test models on hydrogen behavior in steels

4 Experimental

4.1 Tested materials – composition and state

DSS contains many grades, as shown in chapter 2. The standard DSS (2205DSS) and lean duplex stainless steel (2101LDX) stainless steels were chosen only as case studies to test the approach suggested in this research. Both contain austenite and ferrite in reasonable quantities. Both are used in industry and both are studied with regard to hydrogen assisted cracking. Table 6 shows the nominal values of the alloying elements. The measured values of the alloying elements in the materials are shown in Table 7.

Table 6: Nomenclature and nominal chemical composition of the tested DSSs (wt.-%).[27]

Grade	**UNS**	**EN**	C	Cr	Ni	Mo	Mn	N	Cu
2205	**S31803**	**1.4462**	0.03	21.0-23.0	4.5-6.5	2.5-3.5	2.0	0.08-0.20	
2101	**S32101**		0.04	21.0-22.0	1.35-1.70	0.1-0.8	4.0-6.0	0.20-0.25	0.10-0.80

Table 7: Chemical composition of the tested DSSs (wt.-%) measured by optical emission spectroscopy (OES).[177-179]

Grade	C	Cr	Ni	Mo	Mn	N
2205	0.018	22.35	5.54	3.08	1.82	0.156
2101	0.02	20.96	1.54	0.183	4.88	0.17

Commercial lean 2101 and standard 2205 DSSs were purchased from ThyssenKrupp and specified by Edelstahlwerke GmbH.

Figure 4-1 shows the orientations that were examined for each type of steel and experiment:

- For the 2205 standard DSS: The as-received material was in the form of a rod after solution-annealing at 1050°C and water quenching with a measured ferrite content of 51 vol%. The standard DSS was used in all experiments and was analyzed in the normal and perpendicular directions as shown in Figure 4-1.
- LDX 2101 was received in the fully annealed condition as a 1 mm thick plate with a measured austenite fraction of approximately 60%.

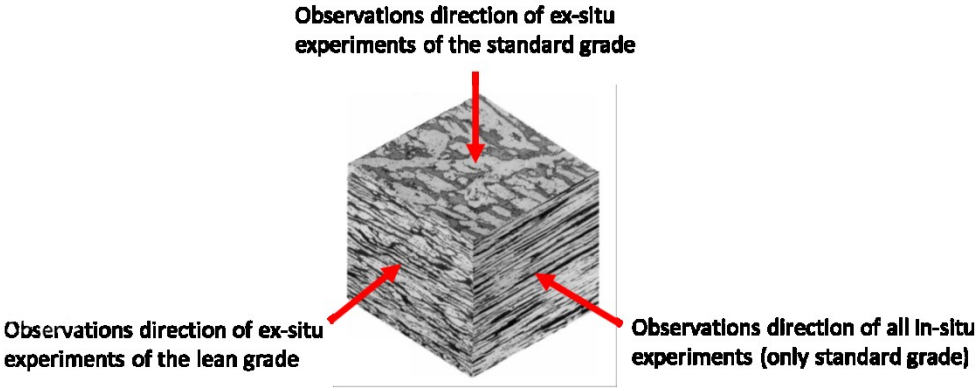

Figure 4-1: Directions in which the observations, for each type of steel and experiment, were conducted (figure was taken from ref.[13]). Ex-situ experiments were conducted at the normal direction (ND) for the DSS2205 and in the transverse direction (TD) for the LDX2101. In-situ permeation and in-situ mechanical loading experiments were conducted in the rolling direction (RD).

4.2 Detection and analysis

4.2.1 Time-of-Flight Secondary ion mass spectrometry (ToF-SIMS)

Mass spectrometry (MS) is widely used in a variety of methods and fields. The literature review contains two out of many approaches where MS is applied (as the analyzer for general quantification of hydrogen and in SIMS). The analysis procedures can be used in many different ways, such as: the physical state of the analyzed material (solids, liquids and gases) and the detector type (ToF, quadrupole, etc.). ToF-SIMS was applied to many other fields before it was adapted to hydrogen analysis in steels (in-organic, organic and biological, semi-conductor industries and even forensic investigations). ToF-SIMS is based on a secondary ionization process resulting from a primary ion. This technique enables the determining of the atomic and molecular composition of solids following a sputtering process of the material surface. There is a variety of operation modes, two of which are shortly introduced in chapter 2.6.4. Each operation mode is used to address different analytical problems.[180]

A schematic drawing of a ToF-SIMS and the optic system of the LMIG (focusing) are shown in Figure 4-2 and 4-3a, respectively (the adjustments of the different parts in the LMIG are described in the following chapters).

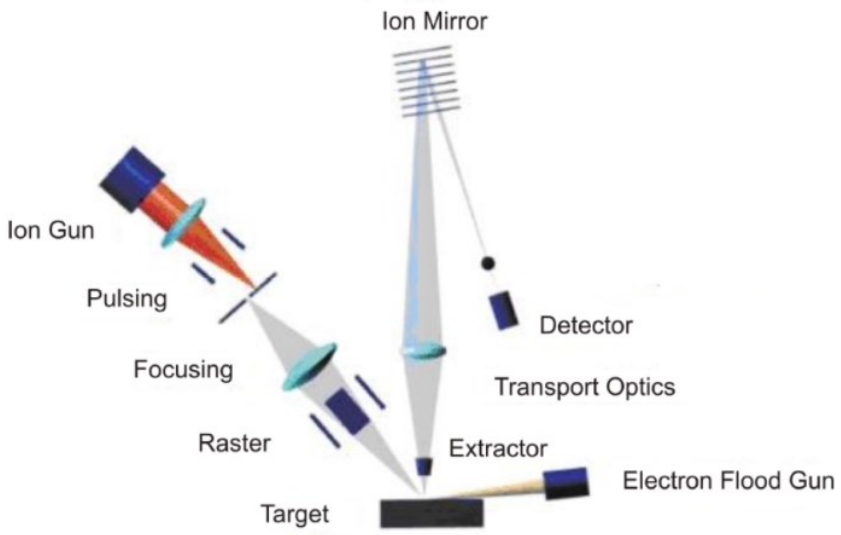

Figure 4-2: Overview of the liquid metal ion gun column in the ToF-SIMS instrument of IONTOF © (Muenster, Germany).

The ion source, and in general the primary ion gun, is the most significant part of the instrument by which the type of desired resolution (mass or lateral) is adjusted and determined. Nowadays the primary ions are extracted mainly from a liquid metal ion gun (LMIG). For less than a decade Bi has been used to generate the primary ions, however in the past other metals were used as an ion source such as Ga and In. The main requirements from a LMIG are high mass projectile and strong and distinct signature in the mass spectrum.

As a result of the sputtering process, only a small fraction of sputtered particles is electrically charged and analyzed according to their mass to charge ratio (m/z) in the mass spectrometer/analyzer. The sputtering process in both dynamic and static SIMS induces secondary ions that are positively or negatively charged.

The extraction of each polarity is controlled by the “extractor” which is the first part of the detector (cf. Figure 4-2) by applying counter potential to the desired ions on the extractor. Surface spectra can be obtained either in the positive or negative analysis mode. The majority of elements have different ion yields in each polarity. Therefore, in most cases, optimal analytical and spatial information for a specific element is obtained in one analysis mode. In this research both negative mode and positive mode data were obtained in sequential experiments by switching the polarity of the whole mass spectrometer. The negative mode was used for obtaining D^-, OD^-, CN^-, CN_2HD^- signals and the positive mode for distinguishing the chemical composition of ferrite and austenite by the detection of the metallic alloying elements (Cr, Fe, Ni etc.).

4.2.1.1 Modes of operation

The different modes of operating the LMIG differ in their mass and lateral resolutions. High mass resolution is obtained by using the High Current Bunched (HCBU) mode where a high flux primary ion beam is bunched to allow a minimal time gap between the first and last primary ions in each package delivered to the sample. In this case the lateral resolution is limited to only 2–10 µm. On the other hand, the Burst Alignment (BA) mode is used for fast imaging. In this case the optical alignment is based on the “Lens Source” lens to produce a beam crossover in aperture 2 and subsequently the “Lens Target” lens is used to focus the primary ion beam to a minimal spot size on the target surface. In the BA mode the primary ion current is three orders of magnitude lower than in the HCBU mode, therefore in the BA mode the data acquisition process takes much longer. In comparison to these modes (HCBU and the BA) the Collimated Burst Alignment (CBA) mode[161, 162] is used for imaging with higher spatial resolution due to the reduced primary ion intensity (below the

BA). The improvement in this mode is achieved by applying higher voltage to the “Lens Source” in order to diverge the beam. Aperture 1 blanks out the ions deviating from the optical axis whereas the collimated near-axis ions pass through. The higher voltage applied to the “Lens Source” collimates the primary ion beam and decreases the primary ion intensity. The collimation process shifts the crossover from aperture 2 (in the BA mode) towards the target. By applying a voltage to the “Lens Magnification” the shift of the crossover from aperture 2 is compensated. Another advantage in this mode is the focusing and aligning of the beam is simpler and faster compared to the BA. The achievable spatial and mass resolutions and the typical voltages applied on the different lenses for the HCBU, BA and CBA are given in Table 8 and an illustration of the beam pathways in the optical axis for BA and CBA are shown in Figure 4-3b (noteworthy is that the given values were obtained on a ToF-SIMS V with Bi^{1+} instrument using standard BAM L200 specimen[156]). Unlike the BA mode where focusing of the beam is fulfilled by adjusting the “Lens Target” and “X/Y Stigmator”, the first step to acquire good focus in the CBA mode is done by aligning the “Lens Magnification” in such a way that the current signal on aperture 2 (scope 2) achieves a rectangular-like shape.[161] The next steps are similar to the BA mode alignment.

Table 8: The achievable spatial and mass resolutions and the typical voltages applied on the different lenses for the HCBU, BA and CBA.[161]

Operation mode	HCBU	BA	CBA
Lateral resolution (l.r.)	~2 to 10 µm	~250 to 300 nm	96 < l.r. < 136 nm
Mass resolution	~11 000	~200	~200
DC-current	16 nA	0.4–0.75 nA	70 pA
Lens Source	~3150 V	~3300 V	~3750 V
Lens Magnification	~15 kV	0 V	13 kV
Ion-fluence at the target [ions/cm^2]	~3.3×10^{11}	~3.1×10^{11}	~2.8×10^{11}

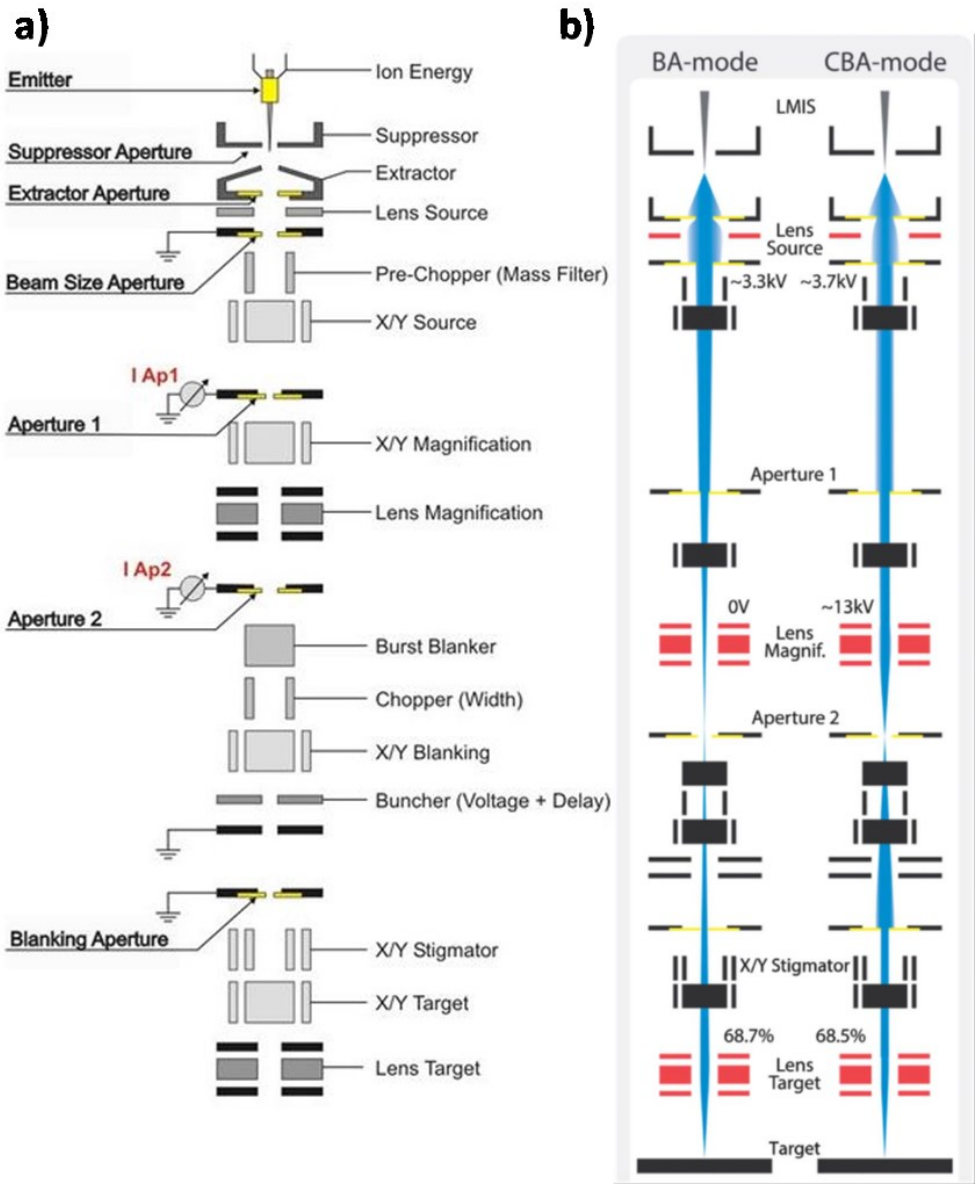

Figure 4-3: a) Overview of the liquid metal ion gun column in the ToF-SIMS instrument of IONTOF © (Muenster, Germany) and b) Primary ion gun scheme of the beam guidance for the BA and CBA modes used for imaging on an ION-TOF instrument.[161, 162]

4.2.1.2 Sputtering ions for surface contamination removal and ion yield enhancement (dual gun)

The ToF-SIMS is equipped with a dual source column – DSC (in addition to the LMIG primary ion gun). The primary ion beam is pulsed to get chemical information by analyzing the secondary ions emitted between each pulse (timing of the sputter and secondary ions extraction into the ToF-analyzer). The pulsing results in a very low current density (i.e. low erosion speed < 0.1 nm/min). When a high sputter rate is required (e.g. for depth profiling) the DSC uses a dual beam mode. In this way the DSC beam is sputtering the surface and the newly exposed surface is analyzed by the second beam. The DSC can work in two modes: sputter and analysis and with three different sources of ions: Ar, O, and Cs. The sputtering mode with any of the sources can be used to clean the surface from contaminations. In addition, O and Cs can be used also in order to enhance secondary ion yields.

The formation of negative secondary ions is greatly enhanced by the presence of Cs at the surface, while the yield of positive secondary ions is improved by oxidation of the surface. Oxidation can be achieved by oxygen bombardment and/or by oxygen flooding (increasing the partial pressure of oxygen within the analysis chamber by a nozzle of oxygen gas).[181] The ion yield is shown in Figure 4-4 for Cs sputtering and in Figure 4-5 for O sputtering. In summary, O and Cs are reactive sputter species and deliver enhanced secondary ion yields for specific elements in positive or negative SIMS, respectively. Ar, on the other hand, is a non-reactive sputter gas, delivering a basic secondary ion yield. Surface contamination removal and ion yield enhancement were the key advantages of the dual beam mode in all the experiments in this work. The dual mode allows adjusting of the analysis and the sputter parameter independently, e.g. the use of a low energy sputter beam of O_2 or Cs to remove any surface contaminations and in parallel to increase the yield of positively or negatively charged secondary ions. Both can be used in low voltage for short times in order to minimize topographical and structural damage. Literally, in the current work O sputtering was used to enhance the ion yield of positive fragments (i.e. almost all alloying elements, for example to detect the phases by the composition) and the Cs was used to enhance the ion yield of all negative fragments (almost all non-metals, for example H, D, O, S, P, Si and fragments of these elements).

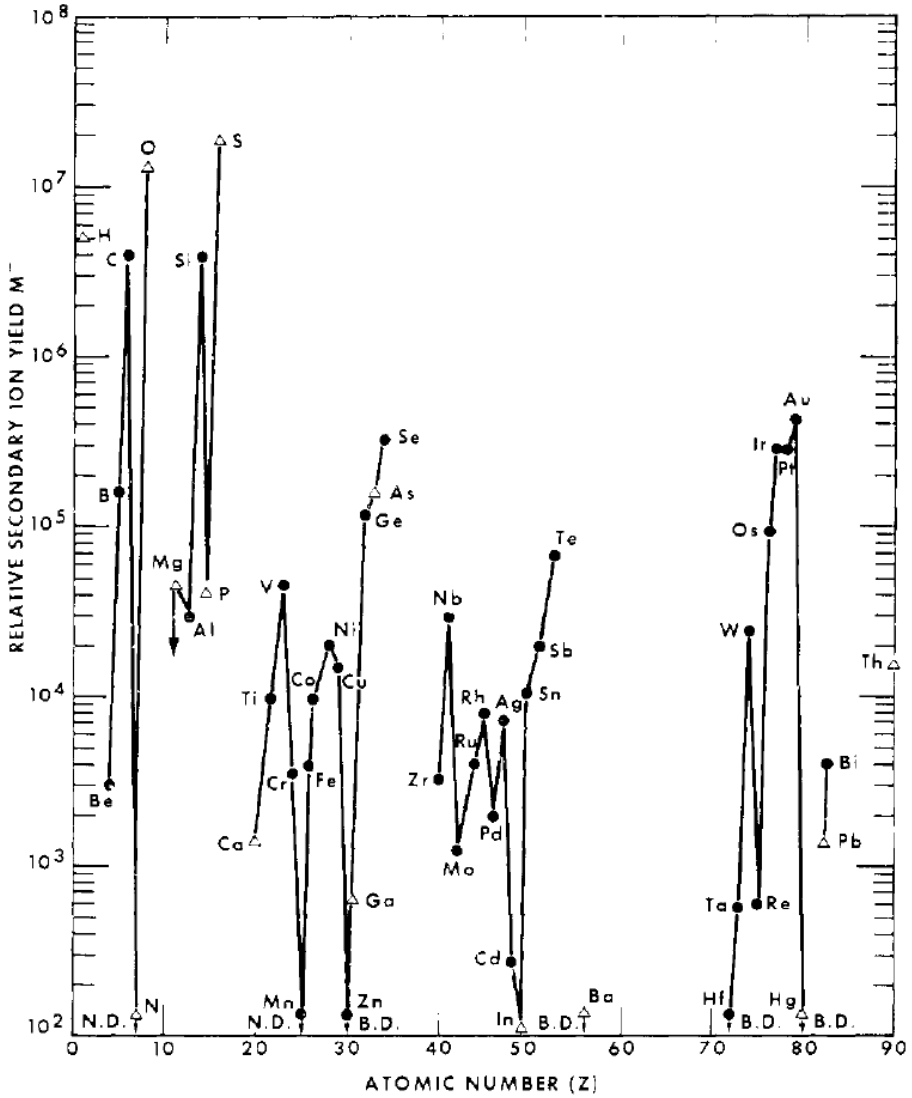

Figure 4-4: Relative secondary negative Ion yield (M-) from Cs+ bombardment vs. atomic number of secondary ion. [181]

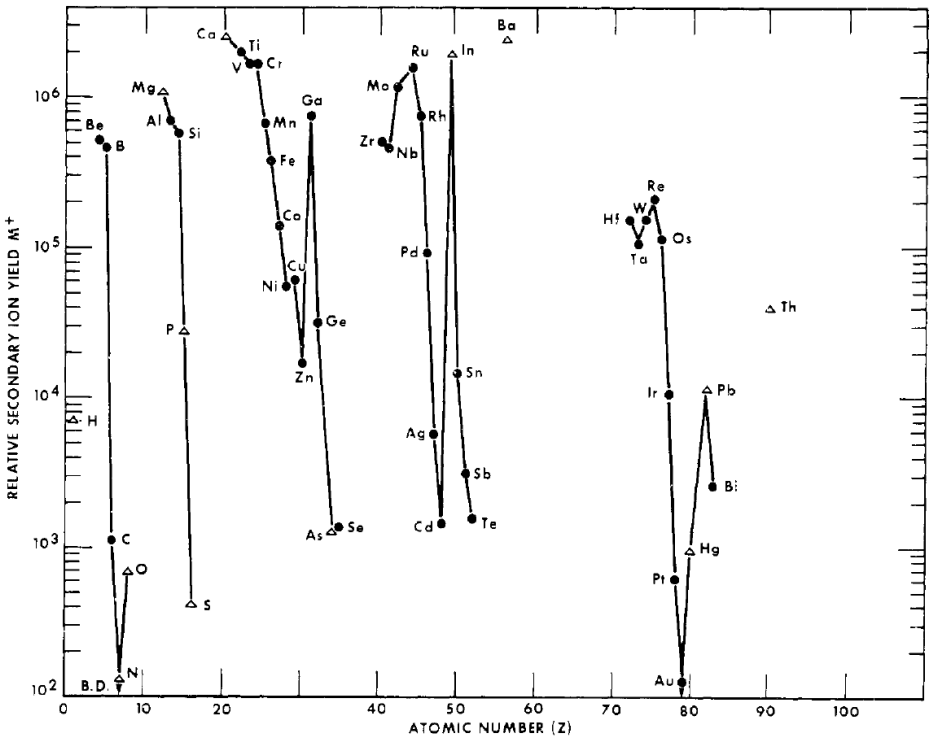

Figure 4-5: Relative secondary positive ion yield (M+) due to O- bombardment vs. atomic number of secondary ion.[181]

4.2.2 Application specific sample holders and sample preparation

The core of this research is based on observing the distribution of hydrogen after electrochemical charging, during hydrogen permeation and during external mechanical loading. Each of these observations required a specific experimental setup which is based on a suitable sample holder and sample geometry. The design of the sample holders for the in-situ experiments was the most challenging part in this project due to the following reasons:

- Must function in the ToF-SIMS chamber (i.e. UHV regime) without breaking the required conditions for the analysis.
- Geometry and size limitation in accordance with the analysis probes (primary and DSC guns, analyzer, etc.), mechanical positioning system of the stage, power supply plugs and cold fingers.
- In case of non-infinite hydrogen source: the ability to control the temperature of the sample due to the high effusion of hydrogen in the ToF-SIMS chamber in RT.
- The ability to apply mechanical loads by an electric device that can function under UHV.

The following parts describe the considerations and design of the experimental setup.

4.2.2.1 Ex-situ – static analyses

The heating and cooling sample holder is produced by IONTOF and is part of a system for the analysis chamber and loadlock. This system comprises of cooling by liquid nitrogen (LN_2) that is connected to the sample by a heat conductive material (cold finger made of copper), resistive heating and programmable computer controlled temperature of the sample (the sample holder is shown in Figure 4-6). The sample temperature can be adjusted between -130°C and + 600°C with a 1°C precision.[182] The sample holder has four electric pins which are designated for temperature measurement by a thermocouple and power supply for the resistive heating coils.

The reason for using this sample holder stems from the high diffusion rate of hydrogen and the loss (effusion) of hydrogen from the sample in UHV (as it is in the main chamber of the ToF-SIMS instrument). For the ex-situ observations the sample is mounted on the heating/cooling sample holder and transferred to the loadlock at room temperature. The first step is to purge dry nitrogen at $5x10^2$ mbar to minimize adsorption of atmospheric species at the sample surface and to reduce the humidity in the chamber. Subsequently the cold finger is attached to the sample and the sample is cooled down by filling LN_2 in the dewar.

Cooling the sample without dry nitrogen induces the formation of a relatively thick ice layer (compared to the information depth of SIMS) on the sample surface. In addition, filling the dewar with LN_2 before attaching the cold finger generates an insulating layer of ice between the cold finger and the contact plate of the sample holder. The gas purging is stopped when the sample reaches a temperature of -70°C. In this stage the loadlock is pumped to $5x10^{-6}$ mbar. The sample is transferred into the analysis chamber when it reaches a temperature of -130°C. The low temperature of the sample allows analyzing and sputtering of the sample without losing the diffusible hydrogen.

Due to the high mobility of hydrogen or deuterium in metals at room temperature, and a higher diffusion coefficient and lower solubility in the ferritic phase, it is impossible to consider an analyses concerning deuterium segregation in this phase at room temperature in this setup (ex-situ electrochemical charging).

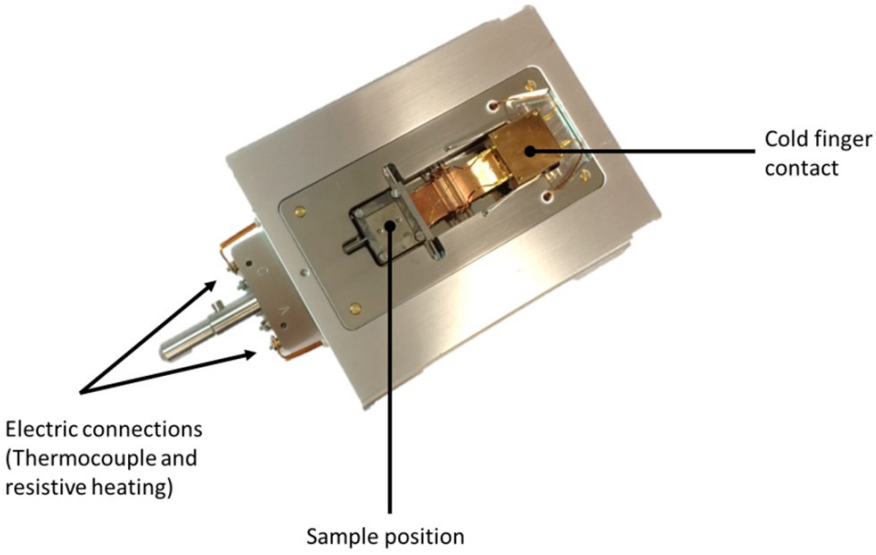

Figure 4-6: Description of the sample holder for ex-situ mechanically non-loaded experiments (*IONTOF ©, Muenster, Germany).*

The flat samples (11 x 8 mm^2) for the mechanically non-loaded experiments were prepared by spark cutting the materials normal to the rolling direction and were carefully grinded and polished using a 0.25µm diamond suspension as the final step. The spark cutting technique was also used for preparing a hole in the sample for immersing it in electrochemical charging. The sample dimensions and geometry are shown in Figure 4-7. Before charging with deuterium, all samples were cleaned for 10 minutes in an isopropanol ultrasonic bath.

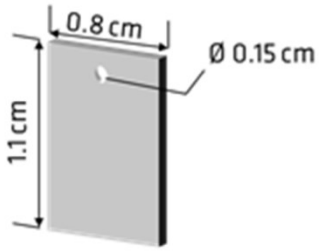

Figure 4-7: Geometry and dimensions of the sample for ex-situ mechanically non-loaded experiments.

4.2.2.2 In-situ –mechanical loading experiments

A specific sample holder was designed and manufactured in collaboration with the BAM workshop. The installation and optimization of the device for mechanically stimulated loading required the following conditions, in addition to the limited space under the analysis probes:

- Control over the sample temperature in an in-situ experiment inside the ToF-SIMS instrument due to the high effusion rate of hydrogen on one hand, and the need of ductile behavior of the material above the ductile-to-brittle transition temperature (DBTT), on the other hand.
- Measurements by ToF-SIMS require a flat surface.
- The ability to induce force by a device that can function in UHV. This device should not produce any heat and should not contain any lubricants as both can affect the vacuum and the experiments, e.g. piezoelectric device.

The sample holder is based on the temperature monitoring core of the ex-situ sample holder described in the previous chapter. This core was incorporated into the device by

keeping the temperature monitoring (by a thermocouple) and removing the resistive heating option. That allowed having two pins to supply electricity to the mechanical loading system. The only device that can supply sufficient mechanical load is a piezoelectric actuator. Piezo elements can work in a static mode for high and continuous loads (tested in this work) and in the dynamic mode with a frequency controllable load for simulating fatigue loads (not tested in this work). PiezosystemJena[183] was found to be the company which can deliver the piezo actuators with the geometric requirements. The actuators are from the PA/T series that is based on stack type actuators in a multilayer design (shown in Figure 4-8a). The actuator is mechanically pre-loaded to facilitate dynamic applications. The housing of the actuator, in combination with built-in springs, allows a motion without mechanical play (shown in Figure 4-8b). The drawback of a piezo based actuator is that it has a drift and hysteresis. This problem can be solved by attaching a high resolution strain gage feedback sensor to the actuator by the supplier. The typical accuracy with a strain gage is 0.5% of the used motion. This solution was inapplicable in this case due to the limited number of electric lines in the ION-TOF sample holder (cf. Figure 4-6).

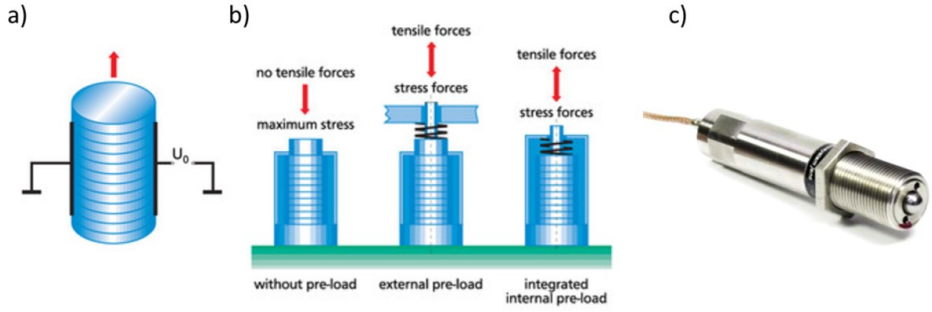

Figure 4-8: Schematic illustration of the Piezo actuator, a) The stack type architecture, b) Preloading technique and c) The PA/T design.[183]

The limitations of having a sample with a flat surface and design based on the core of the ION-TOF heating/cooling sample holder, forced a four-point bending test. The specimen geometry is a beam with uniform cross section. In three-point bending, the load is applied at the mid-span of a simply supported beam whereas in four-point bending, equal loads are applied at equal distances from the simple supports to create a shear-free central region.[184] The design of the sample holder is shown in Figure 4-9.

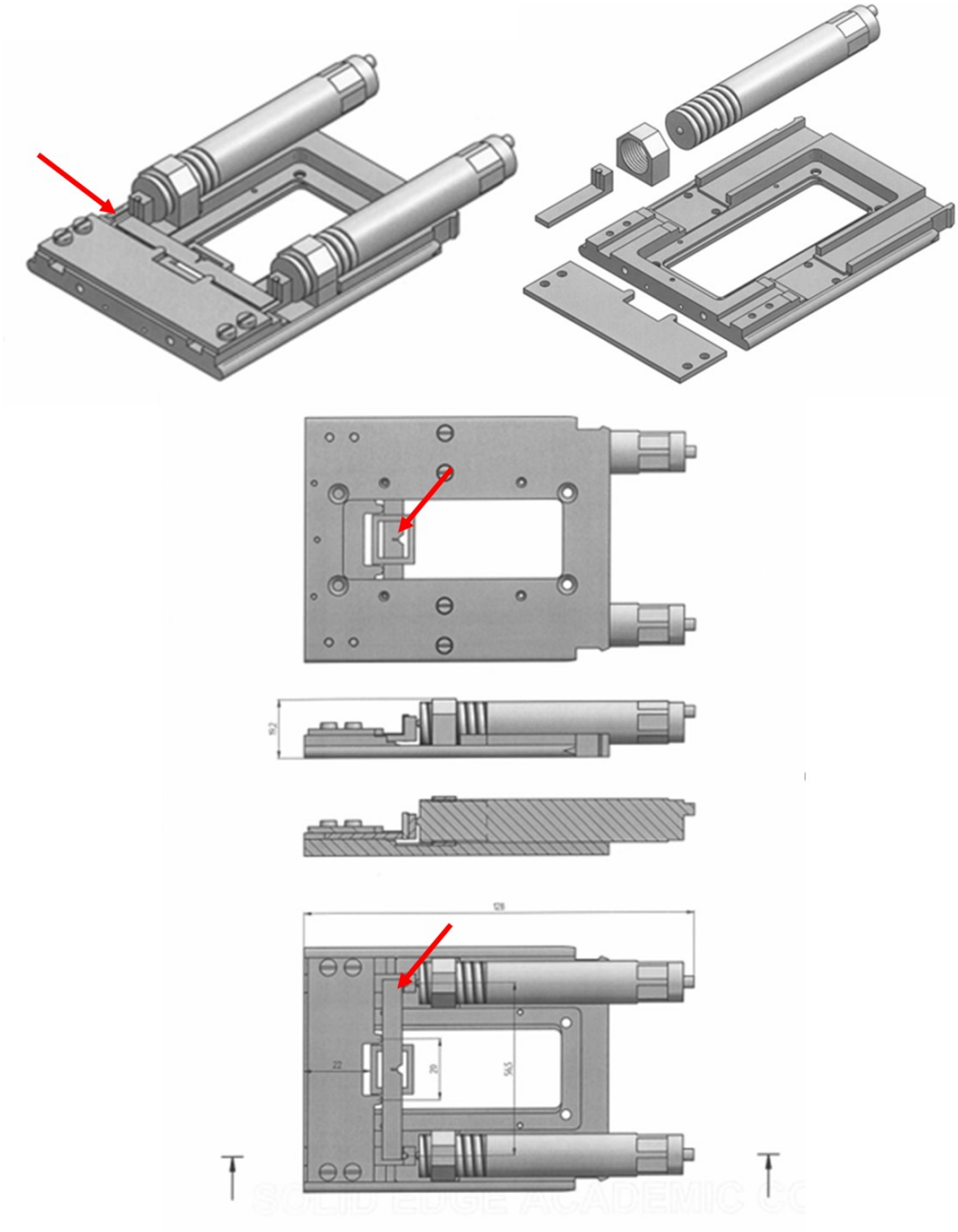

Figure 4-9: Geometry and dimensions of the sample holder for in-situ four-point bending experiments. The sample is indicated by a red arrow.

The bend testing standards[184] were not considered in the design of the sample holder due to the small dimensions of the whole device. However, based on four-point bend testing where a uniform tensile stress is applied over a relatively large area of the specimen, the maximum deflection (middle of the specimen between the two inner spans) can be estimated from the following equations:

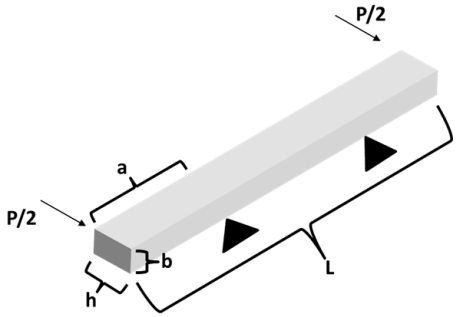

$$\delta = \frac{Pa}{24EI}(3L^2 - 4a^2) \tag{14}$$

$$I = \frac{bh^3}{12} \tag{15}$$

where P is the load, a is the distance between the inner and outer support spans, L is the distance between the outer spans and E is the Young's modulus. For calculating the moment of inertia I for a rectangular beam, h is the length along the axis parallel to the load and b is the length along the normal axis of the specimen.[184] The initial thickness of the sample obtained by EDM slicing was 750-800µm. The samples for this experiment were also carefully grinded and polished using a 0.25µm diamond suspension as the final step for the analyzed side. In addition, the samples for this experiment were notched by EDM (with a wire diameter of ~0.1mm) in order to enhance the stress concentration ahead of the notch and therefore the equations shown above cannot be applied. The geometry and dimensions of the sample are shown in Figure 4-10.

The setup of the in-situ mechanical loading experiment is similar to the ex-situ experiments. In these experiments the sample was also charged with deuterium before analyses, mounted on the mechanical loading device, introduced to the main chamber and held at low temperature using LN_2 cold finger.

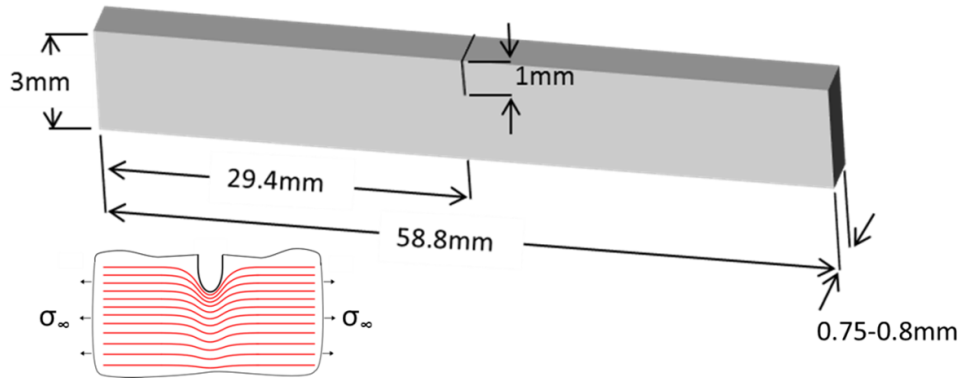

Figure 4-10: Geometry and dimensions of the sample for the in-situ mechanical loading experiments and an illustration of stress concentration ahead of the notch.

The sample was chemically imaged by ToF-SIMS at the sub-µm scale before and after applying the load. The sample holder in this design has three limitations:

1. Limited displacement of the piezo actuators – up to 50µm for each actuator
2. Low cooling rate of the sample due to the robust design in comparison to the sample holder for the ex-situ static experiments
3. Inability to monitor the displacement/ applied stresses due to the lack of a strain gage in the actuators.

4.2.2.3 In-situ – deuterium permeation experiments

This experiment was designed by M.Sc. engineering Franka Straub and has been described elsewhere.[177] The test cell was designed in a Devanathan-Stachursky permeation experiment but was adjusted in a way that allows the ToF-SIMS to act as the permeating ions detector. The cell was made from the test material, a solution-annealed 2205 standard DSS with the flat polished outer surface exposed to UHV, as illustrated in Figure 4-11, for in-situ imaging by ToF-SIMS. This cell allowed continuous electrochemical charging of the DSS (DSS) with deuterium from inside and analyzing the outer surface exposed to UHV at the same time. The inner surface of the cell was flat and plan-parallel to the monitored outer surface. This is how a 0.5 mm thick steel membrane has been established for permeation experiments with deuterium. To introduce deuterium into the steel, a continuous flow of an electrolyte solution of 0.05 M D_2SO_4 and 0.01 M $NaAsO_2$ (recombination poison) in D_2O was realized through the tubular test sample. This was accomplished by pumping the electrolyte through a flexible polymer pipe. The pipe was

lead from outside the UHV chamber to the tubular sample within the chamber using flexible stainless steel bellows. A Pt wire was introduced to the inner part of the tube acting as a counter electrode (anode) in the galvano-static charging process using a current density of 10mA·cm^{-2}. This experiment was running for 38 days.

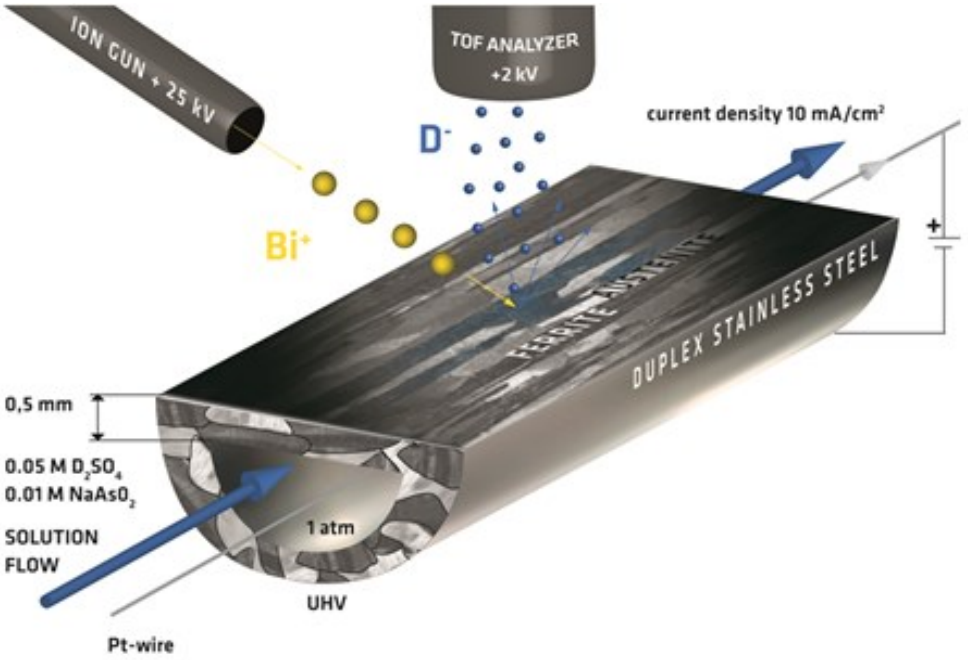

Figure 4-11: Schematic view of the real time and in-situ deuterium permeation experiment within the ultra-high vacuum chamber of the ToF-SIMS instrument.

4.2.3 Scanning electron microscopy (SEM)

For the SEM analyses in this research a LEO 1530 VP Gemini scanning electron microscope was used. Unlike the ToF-SIMS the SEM is based on the acceleration of electrons. The electron source (Field Emission Gun) is located in the upper part of the SEM chamber. The electrons are accelerated to 30 keV and aligned by electromagnetic lenses. The interaction of the electrons with the sample produces a variety of inelastic or elastic collisions resulting in a variety of signals that can be detected by deferent detectors. Three important signals are detected in a typical SEM:

- Back scattered electrons (BSE) are produced by elastic collusion with the grains of the atoms and therefore carry information about the type of the material examined. The energy of the BSE is in the same order of magnitude as the primary beam (E_0)
- Secondary electrons (SE) are produced in the whole volume of interaction by multiple elastic and inelastic collusions. These electrons have an energy order of magnitude three times lower than the incident beam (i.e. <50 eV) and therefore are emitted only from the near surface layers (<50nm). These electrons are used for topographic information.
- Characteristic X-rays have the biggest interaction volume and therefore the lowest resolution. They are produced by the interaction of the incident beam with inner shell electrons of the atom. The interaction yields characteristic X-rays by the relaxation of the atom after the loss of the inner shell electron. Only X-rays allow qualitative or quantitative elemental identification that is conducted by energy dispersive X-ray spectroscopy (EDS).

In the present work SEM was used mainly to produce topographic images of the sample surface by an SE signal. The signal can be detected by two types of SE detectors: normal SE detector (that is located to the side of the sample) and in-lens detector (that is located in the objective lens of the primary beam). Due to the location and design of each of the detectors different objects on the surface can be intensified. In general, an in-lens detector can reach higher magnifications. Figure 4-12 shows the differences between an in-lens detector and regular SE detector in a DSS material.

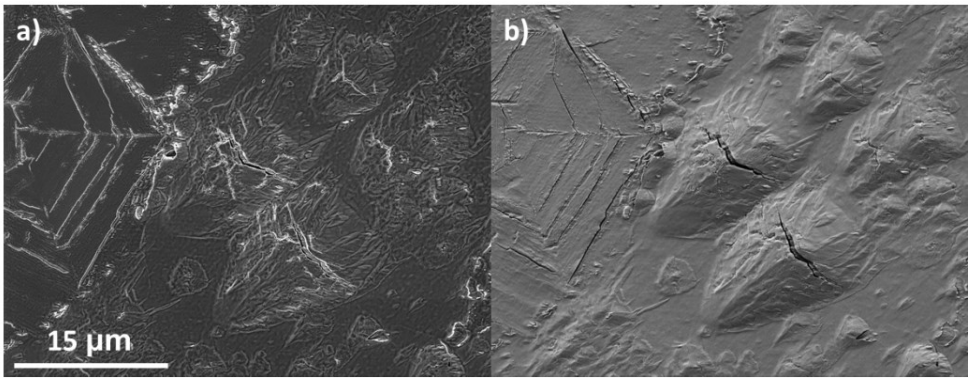

Figure 4-12: SE images taken by a) In-lens detector and b) Regular SE detector of a standard 2205 DSS after electrochemical charging.

In the current work, high resolution images were acquired using a Zeiss Supra 40 instrument (Carl Zeiss, Oberkochen, Germany) equipped with a Schottky field emitter and

attaching a silicon drift detector (SDD). The micrographs were recorded with an Everhart-Thornley detector using 10–20 kV. EDX measurements have been taken in 15 kV by a Thermo Fisher Scientific (Waltham, MA, USA) detector with a 100 mm^2 area and a resolution of 512x384 pixels (140pA, 6s).

4.2.4 Electron back-scattered diffraction (EBSD)

During analyses by SEM, backscatter electrons can be used for obtaining information about the structure. Electron backscattered diffraction (EBSD) is a technique that provides crystallographic information. The main disadvantage of this method is the requirement for a highly polished sample, therefore, as the surface layer is damaged, the extraction of the data is harder. The analysis is conducted by tilting the sample 70° to the EBSD detector which is located 90° to the incident beam. The data is collected by a camera that captures the backscattered electrons that are near to the Bragg angle (forming the Kikuchi bands). An illustration of the analysis setup is shown in Figure 4-13. The information depth is in the order of few hundreds of nanometers for steels and the spatial resolution (obtained by optimizing the spot size of the incident beam) is in the order of few nanometers.

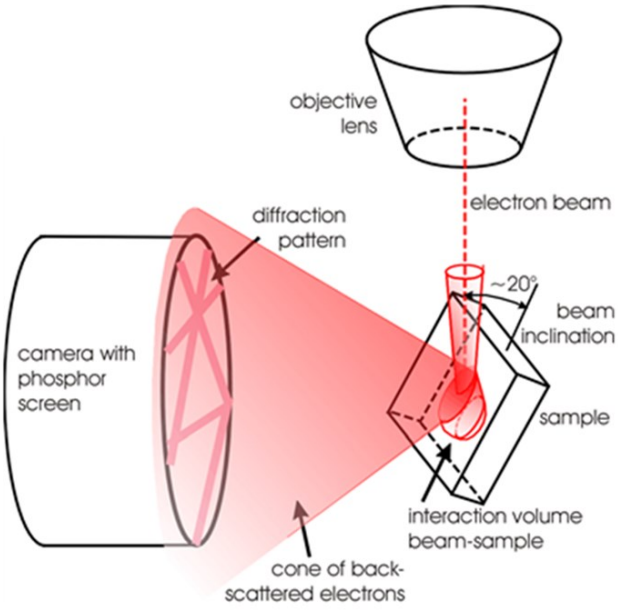

Figure 4-13: Schematic illustration of the experimental setup for EBSD measurements.[185]

The analysis of these patterns is used for the identification of phases, residual stresses, defects and grain orientation. The interpretation of the data is obtained by the comparison of the acquired data to the Kikuchi map that is simulated by the computer after selecting the possible structures. The dataset is produced by recording the Kikuchi pattern of each pixel. These patterns indicate the characteristics of the crystal structure and orientation. The EBSD was used in the current research to study the induced phase transformation phenomena after ToF-SIMS analyses of the ex-situ static samples when the deuterium had direct contact with the analyzed surface.

EBSD investigations were performed in a field emission scanning electron microscope (FE-SEM) LEO Gemini 1530VP FE-SEM (Carl Zeiss, Oberkochen, Germany) with an attached EBSD system of Bruker Nano. EBSD patterns were acquired by an e-FlashHR system equipped with back- and fore-scattered electron detectors (ARGUS) with a resolution of 160 x 120 pixels. The diffraction patterns were collected using 20kV, a beam current of approximately 12nA, step size of 380nm and a dwell time of 15ms. 6 out of 12 bands were correctly indexed. The data processing was carried out using CrystAlign (ESPRIT, Bruker Nano, Berlin).

4.2.5 Focus ion beam milling (FIB)

Focused ion beam (FIB) machining is based on a focused Ga ion beam that erodes the surface aggressively in a similar way as ToF-SIMS utilizes Ar, O or Cs ions. However, unlike ToF-SIMS where the primary beam is larger, FIB allows the creation of a very sharp cut (the curtain) through the sample by focusing the primary ion beam in a way that allows observation of the cross section or production of TEM samples by very thin slices from the sample. The primary region of interest is initially coated by Pt to facilitate the sharp cut. Thereafter, the beam strikes the sample surface and elastic ion-atom collisions result in the removal of surface atoms. Similar to the ToF-SIMS, the primary ion can be collected to produce an image by secondary ions as well as ion induced secondary electrons. The emitted ions are influenced by the crystallographic orientation and therefore grain patterns can be produced from this signal as shown in Figure 4-14. FIB milling was used in the current research in order to investigate the source of the formation of different defects on the surface by observations in the cross section. FIB investigation was carried out on a FEI dual beam Quanta 3D FEG at an operating voltage of 30 kV and current of 0.5nA.

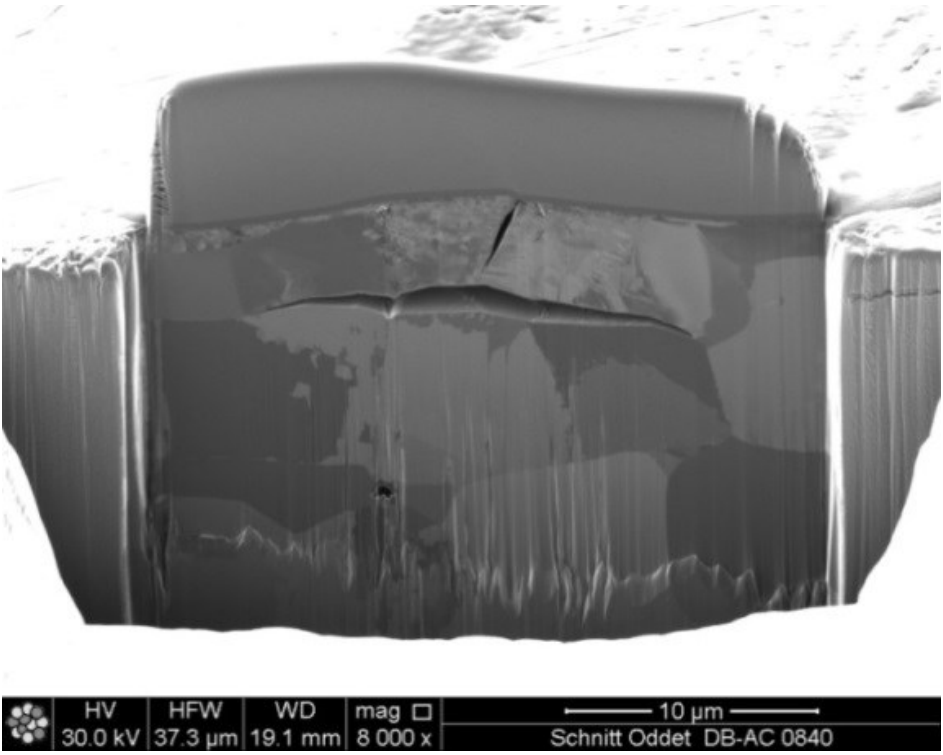

Figure 4-14: Example secondary ion image made during a FIB cut in a standard 2205 DSS after electrochemical charging. The image was made by the secondary ion signal and therefore shows the grain pattern.

4.3 Procedures

As described in the literature survey, the detection of hydrogen by ToF-SIMS was and still is a major challenge. Although there is an increasing number of publications where ToF-SIMS is being applied as a technique for mapping hydrogen in the microstructure in the sub-micron scale, most of the publications use deuterium (^{2}H/ D) and even tritium (^{3}H/ T) implantation as tracers for hydrogen. In some publications it is declared that the electrolyte was prepared with a mixture of both isotopes. The use of the deuterium emerges from the requirement to distinguish between hydrogen species diffused through the microstructure of DSS to the imaged surface and hydrogen containing residual gas species adsorbed thereon. Of course, there are differences in diffusibility and solubility for both hydrogen isotopes, but these range within the same order of magnitude. It is well-known that, in principal, deuterium behaves very similar to hydrogen in steel microstructures. For these reasons it is necessary to use ingredients with the highest purity of only one isotope and not a mixture of both.

4.3.1 External deuterium cathodic charging

Charging in an electrochemical process was chosen in order to imitate service conditions of e.g. off-shore natural gas and oil delivery system; although charging by gaseous deuterium and elevated temperature is possible. The main impact of using deuterium in this research is the high cost of the substances of the charging electrolyte. In addition, the impact of a lower diffusion rate and higher strains in the lattice must be considered.

Due to the high costs of the ingredients, the electrolyte solution was prepared in smaller portions (0.1L instead of 1.0L). In some cases when the electrolyte was changing color (due to a chemical reaction during charging) or when a change of 5% in the pH was obtained (due to charging and evaporation over time) the electrolyte was replaced. The conventional ingredients and the substitutes are given in Table 9. Since some of the ingredients are used in standard concentrations in conventional charging processes they are commonly diluted in water. For this reason it was necessary to use some of the ingredients dry/ purchased diluted in heavy water (D_2O). Cathodic charging was performed in two ways in the presented work. The first type of electrochemical charging of the microstructure was applied during ToF-SIMS observations on permeation of deuterium inside the ToF-SIMS.

Table 9: Components used in conventional and current permeation and charging experiments in the ToF-SIMS

Conventional materials	Amount	Necessities and remarks	Substitutes	Necessities and remarks
H_2O	1 L	Solvent	D_2O	Purchased
H_2SO_4		Dissolved in H_2O, ready-to-use 0.1M solution	D_2SO_4	Purchased
$NaAsO_2$		White crystals Salt, dissolved in H_2O, ready-to-use 0.1M solution	Taken in the dry condition	Dissolved in the electrolyte directly

The charging parameters are described in detail in chapter 4.2.2.3. The second type of charging process was conducted before SIMS analyses for the ex-situ static analyses and for the in-situ mechanical loading analyses. A schematic illustration of the charging process is shown in Figure 4-15. The charging process was conducted for between 48 and 168 hours in order to test the impact of different time intervals on the degradation of the material. For the ex-situ static and in-situ mechanical loading analyses, samples were charged with the same current density of 5mA/cm^2.

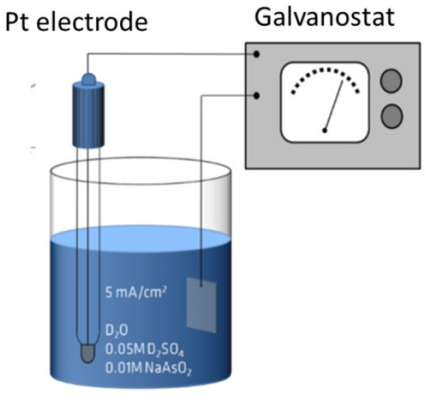

Figure 4-15: Schematic illustration of the electrochemical charging process of the samples for ex-situ static and in-situ mechanical loading analyses.

4.3.2 ToF-SIMS experimental steps and mass interpretation

4.3.2.1 Ex-situ charged samples

During this research an acquisition process was developed to enable data fusion and further observations by different methods (e.g. SEM, EBSD etc.) where the first analysis was conducted on the standard DSS. The lean DSS was analyzed at a later (and more advanced) stage. Therefore, the steps of acquisition are divided into standard and lean DSSs. For the standard DSS, a pulsed bismuth primary ion gun (25 keV, Bi^{3++}) in the CBA mode was used, enabling high lateral resolutions below 100 nm.[161, 162] Additionally to ToF-SIMS imaging in the CBA mode, high mass resolution spectra were acquired using the HCBU mode to differentiate contributions of H_2, OH_2 and D and OD secondary ions (SI) with peaks at m/z=2 and m/z=18, respectively. To remove surface contaminations from the sample and for co-sputtering during analysis, an area of 450 X 450 μm^2 was sputtered with a 3 keV Cs^+ beam. The sputter time was 5 min for surface cleaning and 1 min for co-sputtering after every data acquisition. Cs co-sputtering was also used to enhance the negative secondary ion yield. Imaging of the deuterium distribution was carried out by scanning a field-of-view of 100X100 μm^2 with 1024X1024 or 512X512 pixels and 30X30 μm^2 with 256X256 pixels for high resolution images. Imaging for phase distinction has been made in the positive mode with the sample at room temperature. To enhance the metal secondary ion yields, the sample was sputtered with O_2 primary ions for 1 min. Finally, ion induced secondary electron (SE) images were acquired to enable analysis of the same field-of-view with the SEM later.

For the lean DSS the measurements were carried out on a pulsed bismuth primary ion gun (25 keV, Bi^{1+}) in the CBA mode. To remove surface contaminations from the sample and for co-sputtering during analysis, an area of 300X300 μm^2 was sputtered with a 3 keV Cs^+ beam. In order to obtain a clean surface without inducing considerable changes on the surface the sputter time was 1-2 min. The imaging of the deuterium distribution was carried out by scanning a field-of-view of 50X50 μm^2 or 100X100 μm^2 with 512X512 pixels. Once SIMS analyses had been finished, the sample was left in UHV for one day until it warmed-up to room temperature. Deuterium charged samples must be investigated immediately after charging. During the analysis process deuterium is effusing from the sample, therefore the acquisition process is limited to within a certain time frame. Unlike deuterium distribution imaging, phase identification, before charging or after the sample contains no deuterium, can be conducted without any time limitations. The processes that took place during the whole acquisition of the data are divided these two cases. The actions for phase

identification are summarized in Table 10 whereas the actions for deuterium mapping are summarized in Table 11.

Table 10: Summary of the different processes in the ToF-SIMS before deuterium charging or after the warm-up of the sample.

Procedure	Primary ions	Mode	Raster size (μm^2)	Comments
Positive SI yield enhancement	O_2^+	DC	500X500 to 300X300	
Sputter cleaning	Ar^+	DC	500X500 to 300X300	Alternative to O_2^+ sputtering
Phase identification	Bi^{1+}	HCBA positive	150X150	
Phase identification	Bi^{1+}	BA positive	150X150	Alternative to HCBA

Table 11: Summary of the different processes in the ToF-SIMS in the time frame where the sample contains deuterium.

Procedure	Primary ions	Mode	Raster size (μm^2)	Comments
Negative SI yield enhancement	Cs^+	DC	500X500 to 300X300	
^2H imaging	Bi^{3++}	CBA negative	100X100 to 30X30	
^2H imaging	Bi^{1+}	CBA negative	100X100 to 50X50	
^2H and H_2 distinction	Bi^{1+}	HCBA negative	150X150	Alternative to Bi^{3++}
Ion-induced SE imaging	Bi	DC	150X150	For orientation by other methods.

4.3.2.2 In-situ mechanical loading

The in-situ mechanical loading required the most challenging acquisition process. As mentioned before, on one hand, the sample must contain sufficient amounts of deuterium that must be kept in the microstructure dictating imaging at low temperatures, on the other hand, the mechanical load must be applied at temperatures above the DBTT [186, 187] to have ductile behavior of the material (mainly of the ferritic phase). For this purpose the experiment was conducted by repeating two processes:

- Imaging with ToF-SIMS at a low temperature (~-80°C) (in the initial state before mechanical load and after applying the mechanical load).
- Warm-up by removing the sample from the cold finger to above -50°C (upper range of the ductile-to-brittle transition) and applying mechanical load.
- Cool down by connecting the sample to the cold finger and imaging with the ToF-SIMS while the sample is cooling down.

Two acquisition processes are shown in Figure 4-16 where the red line indicates the temperature of the sample recorded by the thermocouple and the blue line indicates the mechanical load applied to the sample.

The initial experiment was conducted in a single step where the sample was mechanically loaded with maximum displacement of the actuators (Figure 4-16a). The second experiment was conducted in three steps with applying low, medium and high loads (Figure 4-16b).

The mechanical load on the sample was concluded by the displacement of both actuators. The displacement is obtained by applying varying voltage by an external power supply. The actuators are connected in parallel and active in the range of -20 – 130V (indicating zero to maximal displacement).

The user can control the displacement manually using the controls. Each of the actuators are tested by the supplier (PiezoJena) and delivered with a displacement-voltage diagram to allow the user to estimate the displacement by the applied voltage later. Such a diagram is shown in Figure 4-17.

In the second experiment the first image was taken with no load applied (-20V), the second after applying low load (~30V), the third image after applying medium load (~80V) and the last image was taken after applying maximal load (130V).

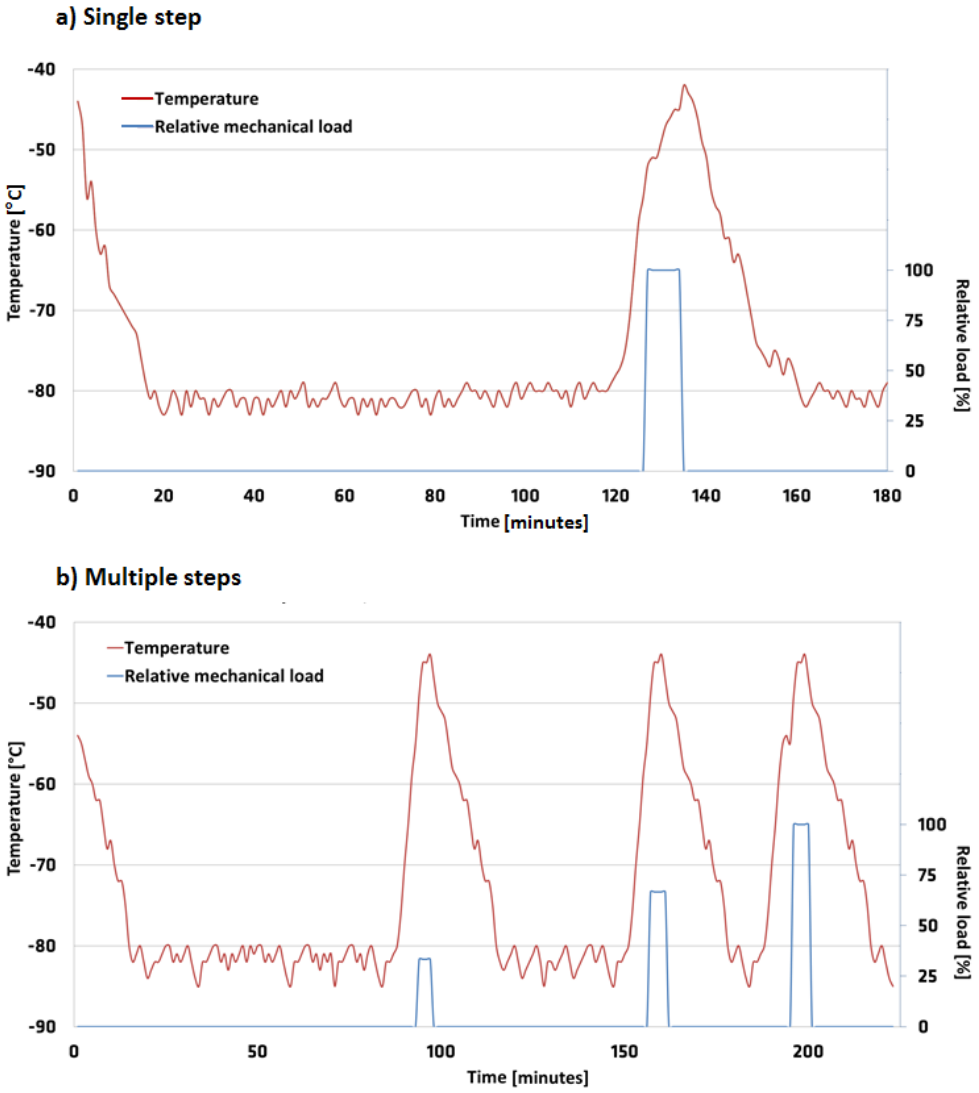

Figure 4-16: Course of the in-situ mechanical loading experiments. a) Applying the maximal load by changing the potential applied on the actuators from -20V to 130V in one step and b) Applying the load stepwise by changing the potential applied on the actuators from -20V to 130V in three steps. Imaging by ToF-SIMS took place when the sample temperature was below -75°C. All images were taken with the same parameters (acquisition time and primary ion current). The blue line refers to the load and the red line to the sample temperature.

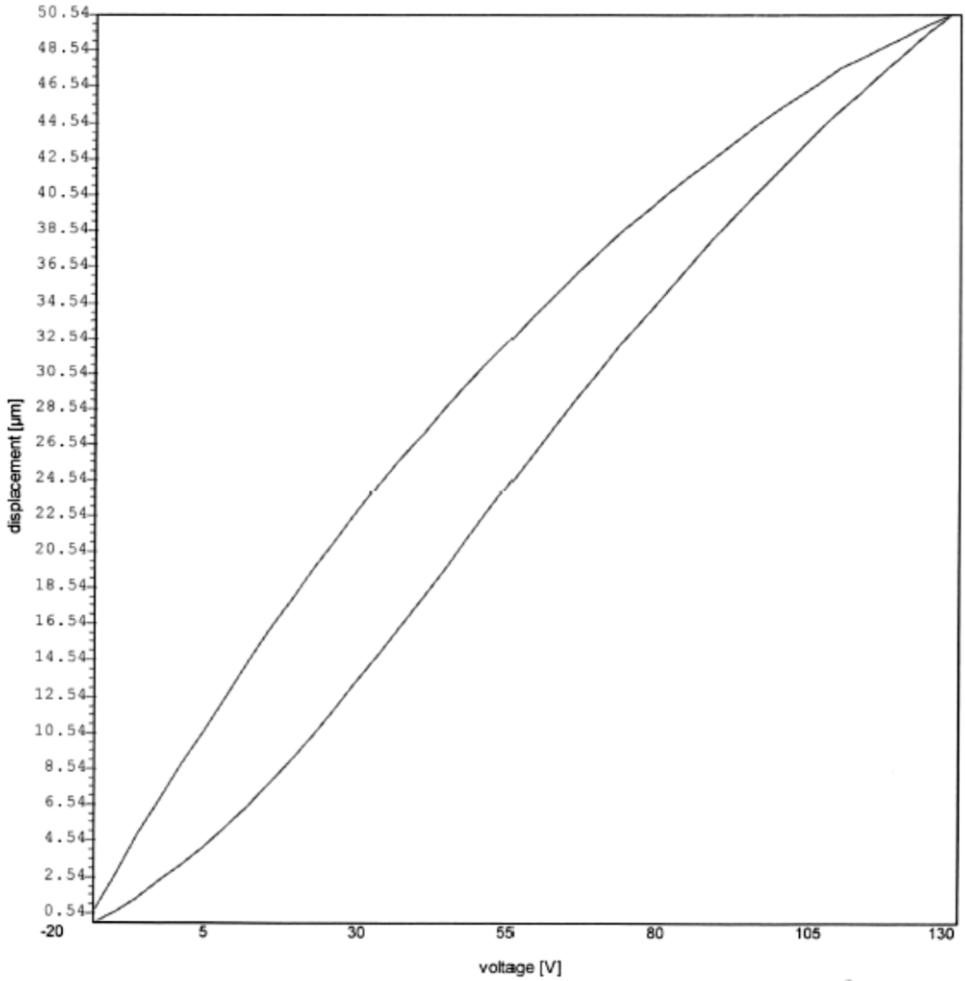

Figure 4-17: Displacement-voltage diagram of a piezoelectric actuator delivered by PiezoJena.

4.3.2.3 In-situ permeation experiments

ToF-SIMS measurements were performed using a 25 keV Bi+ primary ions delivered by a liquid metal ion gun (LMIG). A sputter ion gun providing 3 keV Ar+ ions for sputtering has been used for cleaning the region of interest. Prior to the measurements, an area of 300 × 300 μm^2 was sputtered by Ar+ primary ions for 5 min to remove surface contaminants originating from the cell production process. ToF-SIMS data from the surface of the steel was acquired from a 100 × 100 μm^2 sample region of interest (ROI) performing the burst alignment mode with a beam diameter of approximately ~250 nm providing sufficient lateral resolution for imaging the steel's micro structure.

The information depth of the SIMS method equals the first and second monolayer of the steel surface.[188] The first step of the experiment was to image the finely polished DSS surface of the cell before charging by ToF-SIMS in positive mode. A representative ROI of 100 × 100 μm^2 was selected to identify the austenitic and ferritic phases by the detection of Cr+, Mn+ and Fe+ secondary ions; first with instrument settings delivering high mass resolution (HCBU mode) and thereafter with settings for high lateral resolution (BA mode).[169] Subsequently, negative secondary ion images were acquired from one and the same ROI at increasing times of charging with deuterium over a period up to saturation (37 days).

ToF-SIMS delivers m/z peak list that is interpreted by the operator. For all experiments the interpretation of the peak list is given in Table 12. Based on the interpretation of the spectra and the resulting mass list and mass maps (images) the data is processed by a different software as described in detail in the next chapter.

Table 12: The delivered peak list (m/z ratio) acquired in the HCBU and the interpretation of the mases.

Observed m/z	Suggested assignment (positive SIMS mode)	Suggested assignment (negative SIMS mode)
1		H
2		D
16		O
17		OH
18		OD
26		CN
40		C_2O
41		C_2OH
42		CNO
43		CN_2HD
44		$NOCH_2$
50	^{50}Cr	
52	^{52}Cr	
53	^{53}Cr	
54	^{54}Cr	
55	Mn	
56	Fe	
58	Ni	
68	FeC	
69	FeCH, $CrNH_3$	
70	$FeCH_2$, $^{53}CrNH_3$	NiC
71		$^{54}CrOH$
72		FeO
73	$FeNH_3$, FeOH	FeOH
74		FeOD
75		NiOH, $FeOH_3$
76		$NiOH_2$

4.3.3 Data treatment and data fusion

Except the novel in-situ experiments developed in this research, the second innovative part is the application of enhancement of data interpretability by the use of principal component analysis (PCA) for ToF-SIMS imaging of the deuterium distribution and the fusion of chemical data by ToF-SIMS with topographic data by high resolution SEM (HR-SEM). Although these data processing methods are widely applied in many fields they were never applied to such investigations before now. In addition, it must be noted that in the majority of publications with regard to hydrogen imaging by ToF-SIMS, even fundamental data treatment such as normalization is missing. Prior to any interpretation or further treatments (i.e. PCA) the raw data must be pre-processed by normalizing the secondary ions to the total intensity of each respective mass spectrum, scaling and mean centering. The raw intensity at each mass in each pixel is strongly influenced by the topography of the surface and by the secondary ion yield (i.e. matrix effects). Therefore it is necessary to pre-process the raw data in order to cancel bias related to these effects.

4.3.3.1 Multivariate data analysis (MVA) and principal component analysis (PCA)

PCA was adapted initially to this research on the results of the in-situ permeation experiment. By increasing charging times, enhanced deuterium count rates were observed when investigating the steel surface. In general, for a specific mass, solely, the measured secondary ion intensities in the normalized images are very low and hence a clear correlation of the lateral distribution of different species within the DSS steel microstructure is difficult. The PCA method assists here for identifying and enhancing the contrast between chemically different regions by looking at the main variances within a data set of secondary ions. The principle of PCA is shown in Figure 4-18. PCA uses a matrix containing the measured mass spectra for each pixel in secondary ion image in its rows. Calculated from the covariance of the matrix PCA generates new matrices containing, among others, the scores and the loadings that together represent a concise summary of the original data.[189, 190]

Subsequently to all SIMS measurement principal component analysis was used to identify trends in the collected data set of secondary ions. An example of the contrast enhancement in the loading plots of PCA processed images is shown in Figure 4-19 for the in-situ permeation experiment.

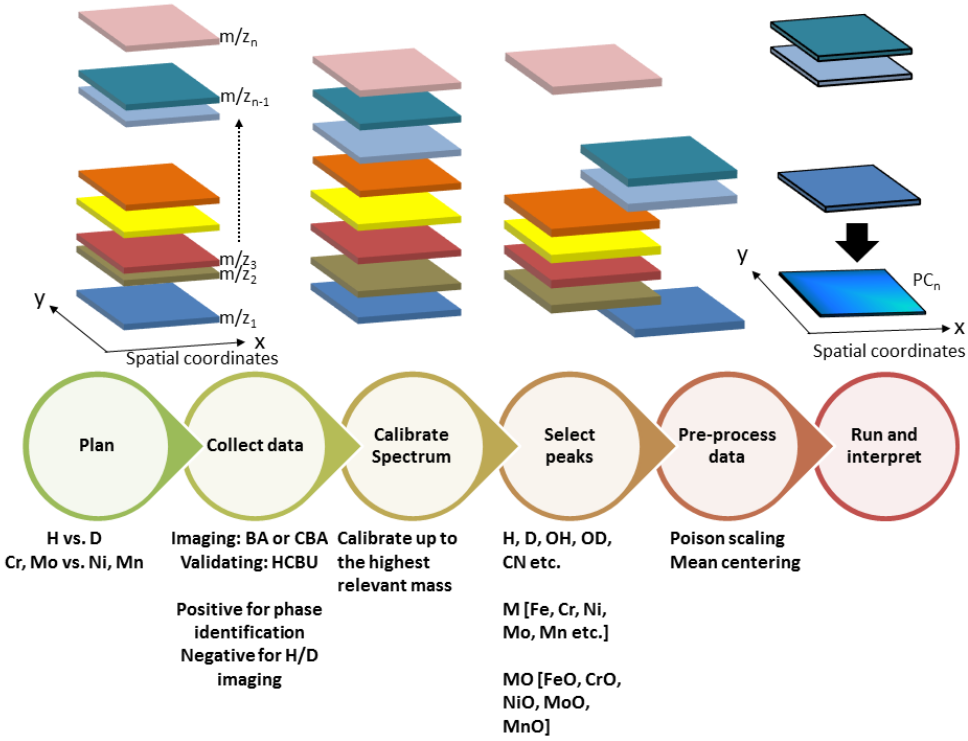

Figure 4-18: The basic concept for data pre-processing and PCA of image data.

This figure shows the time resolved deuterium accumulations in the analyzed surface and the comparison of the D- ions raw data images to PCA contrast enhanced images. Figure 4-19 a-c shows the normalized raw data images of only the D- signal taken after 28, 34 and 37 days, respectively; Figure 4-19 d-f shows the PCA enhanced images of images a-c, respectively. All images were taken from a 100x100 μm^2 area. As mentioned, the selection of specific peaks in the spectrum for applying PCA comes from two reasons:

1. For extracting only useful information from the data and removing noise peaks
2. High overlapping in high masses due to the formation of hydrides and hydroxides of hydrogen and deuterium in addition to the natural metal isotopes.

Noteworthy is that the image data from the in-situ permeation experiments were performed using the Solo + Mia toolbox (v7.5.2, Eigenvector Research Inc.) which were run in MATLAB (v7.9.0.529, MathWorks Inc.).

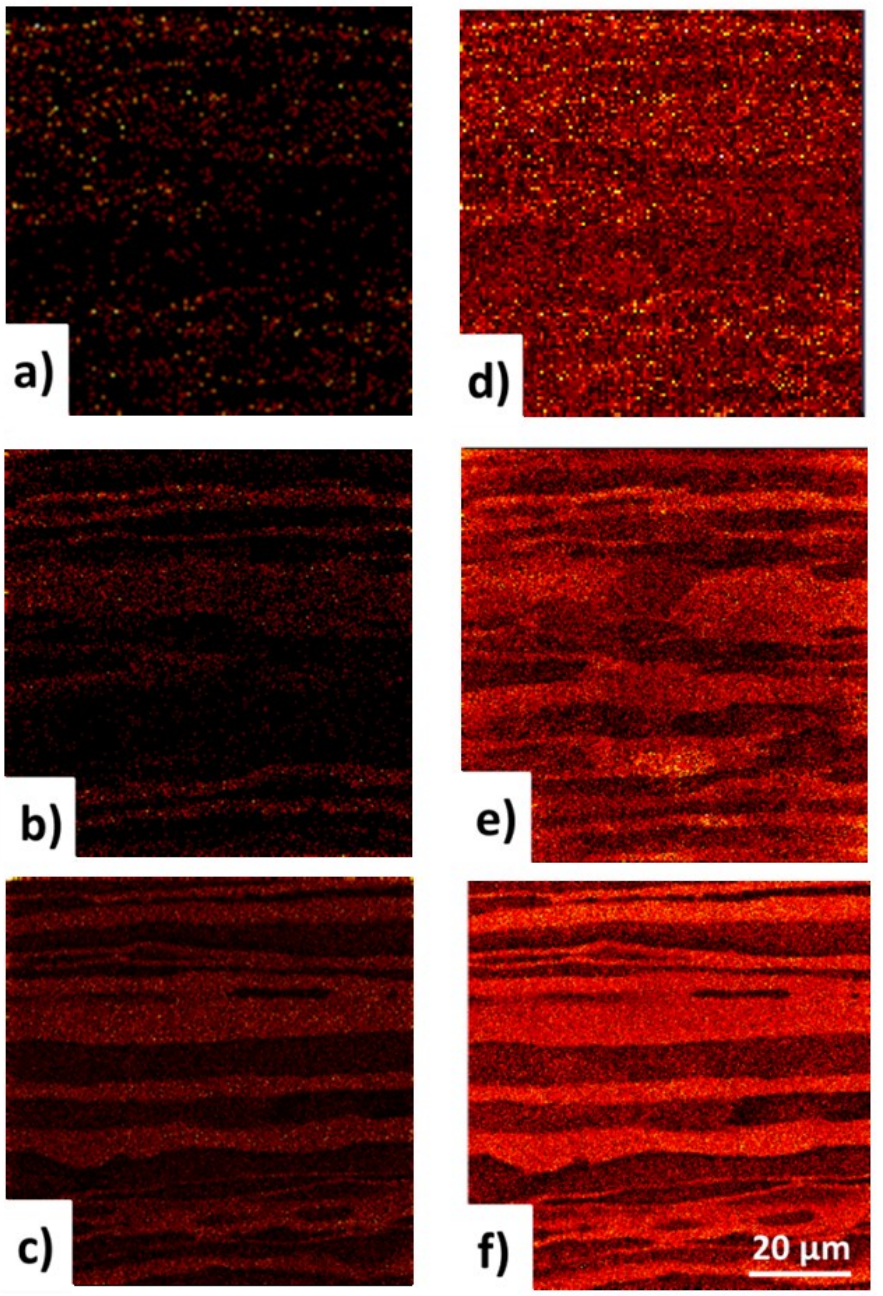

Figure 4-19: Example of PCA data treatment of the raw data acquired in the in-situ permeation experiment. Only the normalized D- signal images taken after 28 (a), 34 (b) and 37 (c) and the PCA enhanced loading plots (d-f) of PC1 of the images shown in a-c.

4.3.4 Data Fusion

Data fusion technology was invented for and frequently used in the field of aerial imaging already in the middle of the previous century. The initial use of data fusion was to combine high quality optical imaging with hyperspectral low resolution images for military uses. The technology is based on the combination of data from two or more sensors on the same area of interest to obtain better interpretability of the data.

At the end of the previous century scientists started to apply data fusion in the field of 'micro' science due to the development of high resolution digital imaging technologies. With regard to surface analyses by SIMS instruments, the machine is usually equipped with an electron detector for acquiring ion induced SE images with relatively low spatial resolution (that is limited by the PI beam and can reach a spatial resolution a bit below 100nm). The combination of SEM images with much higher spatial resolution and the chemical information from the SIMS produces an image that has greater quality and therefore provides more information than any of the input images would alone. It should be noted that for high masses (e.g. alloying metals) the chemical information can be delivered also by the EDX however the resolution is one order of magnitude lower in comparison to ToF-SIMS, not to mention the sensitivity for trace elements. Nevertheless, for light alloying elements (e.g. C, N) and diffusible elements (e.g. H or D) the use of ToF-SIMS is essential.

In the current research ImageLab© was used for both PCA of the data and the image fusion. The software was developed by EPINA GmbH to achieve comprehensive data processing and analysis for data acquired by multisensor imaging systems. As shown before, hydrogen degradation processes of metallic components can be locally characterized by many methods and the ability to work with different data on the same area of interest can be very complicated and therefore such software is necessary. ImageLab was designed for processing and analyzing multisensory data. This software supports the many spectroscopic imaging techniques, the more relevant ones being energy dispersive X-ray and mass spectrometry.[191] The advantage of this software is its ability to combine raw and processed spectral data with conventional high-resolution images. Figure 4-20 shows the general processing queue within ImageLab. Figure 4-21 shows an example of data fusion that was produced after acquiring ToF-SIMS and HR-SEM images on the same area of a deuterium-electrochemically charged 2205DSS. This image also emphasizes the importance of using deuterium instead of hydrogen charging, as it is described in chapter 4.3.1

The main steps that take place in the data processing are:

- The acquired data is subject to a feature extraction generating a set of spectral descriptors which forms the basis of chemometric algorithms applied to the data.[191]
- According to the selected descriptors any data processing can be applied by the user and compared later on.
- The resulting “virtual images” are finally combined into one or several “real” images which may be blended with photos to improve the interpretability of the data.[191]

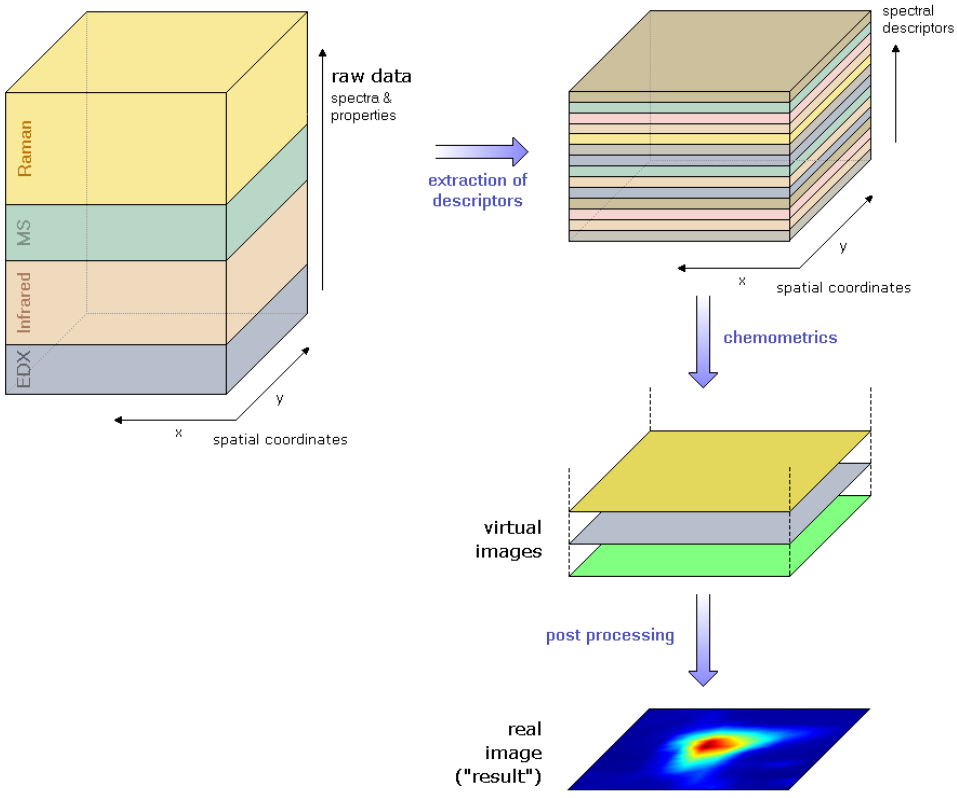

Figure 4-20: The basic concept of ImageLab for data processing and data fusion.[191]

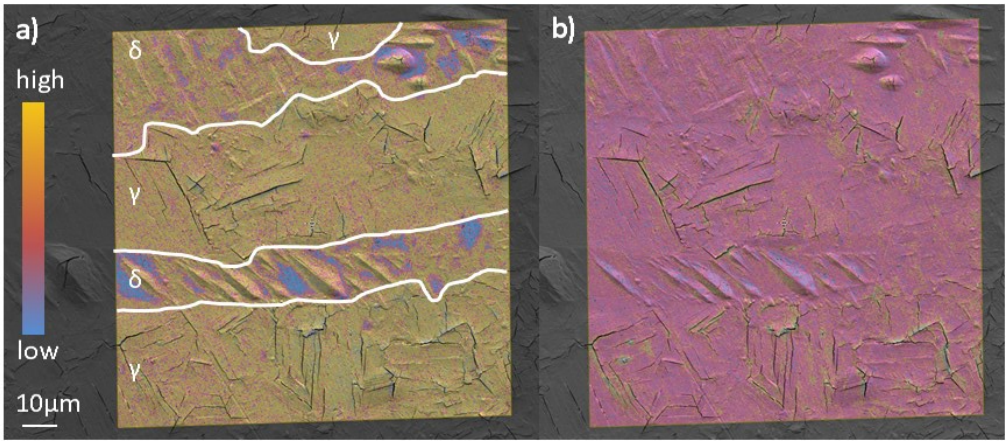

Figure 4-21: Example of data fusion of a HR-SEM image and normalized raw image data of a) deuterium and b) hydrogen SIMS by ImageLab©. The hydrogen is distributed rather homogeneously on the surface of the analyzed sample and is attributed to the adsorbed hydrogen species from the rest gas in the analysis chamber. The increased intensities appearing around cracks are assumed to occur due to the absorption of hydrogen during the time the sample was exposed to air while transferred from the charging cell to the analysis chamber. The deuterium shows higher and more homogeneously distributed intensities in the austenite than in the ferrite. The phase mapping is shown in Figure 4-21a, where γ and δ stand for austenite and ferrite, respectively.

5 Results and discussion

5.1 Ex-situ static experiments

5.1.1 Standard duplex 2205

Before charging the sample, the microstructure was characterized by secondary electron (SE) and secondary ion (SI) imaging. The ferrite and austenite phases have easily been differentiated by the respective Ni and Cr characteristic signals in ToF-SIMS (lower Cr^+ and higher Ni^+ secondary ion yields indicate austenitic grains) and, alternatively, by EBSD. Previous studies revealed a correlation between EDS elemental and SI image analysis[169].

5.1.1.1 Deuterium distribution in ferrite and austenite

Since the standard DSS was the case study for the in-situ mechanical loading experiments, as part of the investigations of the ex-situ static device was to realize the time frame for applying any mechanical load on the hydrogenated sample during ToF-SIMS imaging. ToF-SIMS images of a DSS sample after charging are shown in Figure 5-1. At -120 °C, the γ-austenite grains in the microstructure exhibit significantly higher D^- secondary ion yields, indicating a higher D solubility in this phase as compared to the δ-ferrite and a lower diffusivity, respectively. This observation is consistent with the five orders of magnitude higher diffusivity of D in the δ-ferrite and respectively lower solubility than the γ-austenite phase[167, 192].

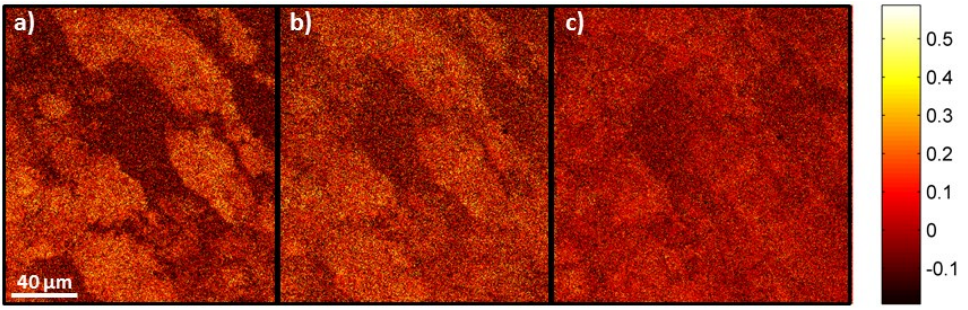

Figure 5-1: PC1 loading plots taken from the same area during sample warm-up of a DSS sample charged for 72 hours: a) -120°C – -60°C, b) -58°C – -30°C, c) -29°C – -4°C. PC1 is representative for deuterium in the microstructure.

During slow warm-up (~0.05 °C·S^{-1}) of the sample from -120°C up to room temperature the clear interface between the ferrite and the austenite was blurring (Figure 5-1) since the

difference in deuterium concentration between ferrite and austenite equilibrates. The distribution of deuterium in the microstructure becomes visible as a blurring of the interfaces between the phases when temperature increases. Figure 5-1a suggests that at low temperature the deuterium is captured in the austenite phase and that the effusion and migration to the ferrite is rather slow. In Figure 5-1b it is shown that deuterium diffusion is from the austenite 'reservoir' into the ferrite, and Figure 5-1c indicates the loss of deuterium in the sample when the sample is approaching room temperature. This phenomenon is caused by the outgassing of deuterium directly from the ferrite and austenite grains on the surface. At the same time the deuterium that is dissolved deeper in the microstructure is released mainly through the ferrite due to the higher diffusion coefficient in this phase. Although the ferrite is acting as a preferred pathway for the effusion and outgassing of deuterium from the (saturated) deeper microstructure[58], the intensity is kept relatively low compared to the γ-austenite due to the low solubility of deuterium in this phase. It should be emphasized that the term distribution is commonly used in the literature for this effect[72, 126, 167] although it refers to a faster effusion of deuterium through the ferrite i.e. along the fast pathway. This effect was also been shown by Mente et al. [9] in a 2-D finite element modeling of hydrogen assisted cracking in DSS. As confirmed by the ToF-SIMS imaging here, a significant higher mobility of deuterium atoms obviously occurs above ca. -58°C.

5.1.1.2 Deuterium induced twinning and cracking in the ferrite

The deuterium permeation and mechanical properties are different in both phases[56] and thus, it has to be anticipated that also the related cracking behavior differs. The effects of deuterium charging are thus highlighted for each phase separately by SIMS at a sub-micrometer resolution and data fusion with the respective SEM topography, as described in the previous section. Figure 5-2 reveals multiple arrow-head shaped plates. The arrow-head shaped plates were slightly elevated from the ferrite surface having microscale twins at the surface region of the plate. This phenomenon has also been reported by Lublinska et al. [193] for a similar DSS where the formation of microtwins has been analyzed with light and electron microscopy and with X-ray diffraction as well. As it becomes visible by the respective data fusion, these plates are characterized by a significantly higher concentration of deuterium, as compared to the surrounding ferrite. Particularly at the surface of larger plates, cracks appeared are associated with pronounced accumulations of deuterium around them, as it also becomes evident by Figure 5-2. In a series of experiments, it turned out that shorter charging times result in smaller number of plates on the surface in smaller size distribution where on some of the plates no cracks were observed as it was also described by Glowacka et al.[194].

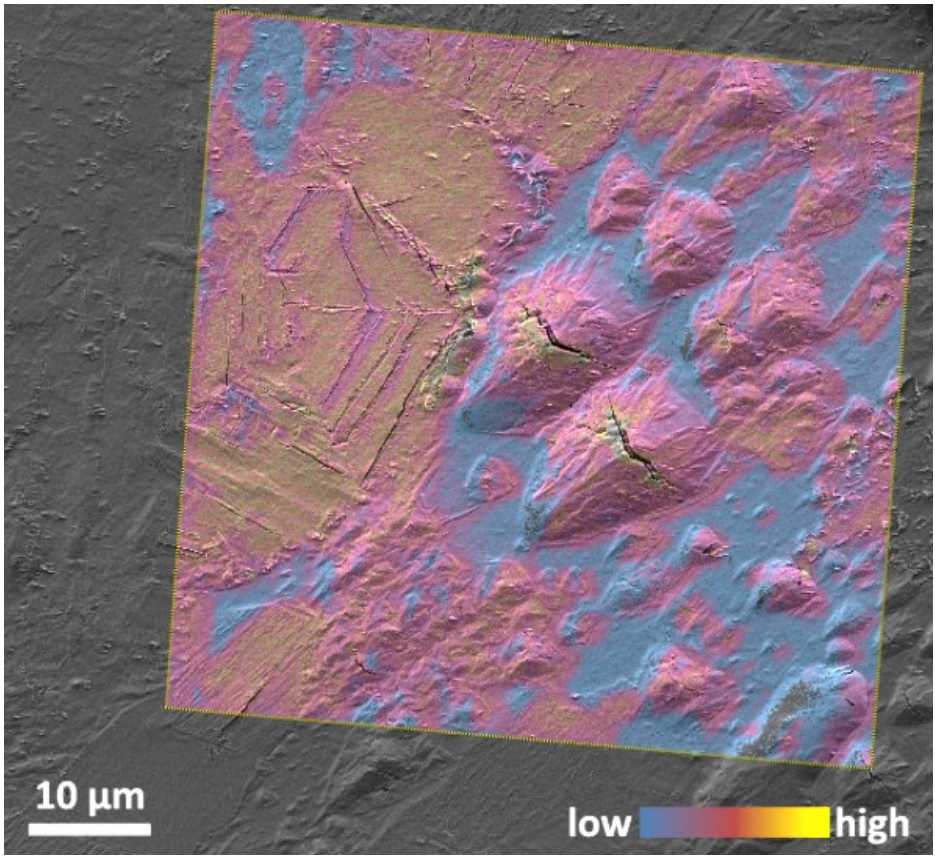

Figure 5-2: Fusion of a SEM topographic image and a SIMS PC1 loadings plot representing deuterium in the microstructure (colored). The image reveals needle shaped microtwins in the ferritic phase which are oriented along the grains. The concentration of deuterium is higher in the microtwins as in the ferrite phase surrounding it. The highest concentration of deuterium is concluded around the cracks. SIMS image data was acquired after 96 hours of electrochemical charging.

By the EBSD investigations, it turned out that micro-twins have been formed preferentially on the outermost surface of the charged DSS sample. Lublinska [121] and Szummer [195] observed a very similar behavior of ferritic stainless steel microstructures, i.e., the formation of grain oriented needle-shaped plates in the surface layer after electrochemical charging with hydrogen, which can also be taken as another evidence for the similarities in the micro-structural effects caused by hydrogen and deuterium. To elucidate further the observed arrow-head shaped plates at the surface to the microstructure underneath it, focused ion beam (FIB) milling has been utilized to produce a cross section normal to the surface and across one of those features which have been previously been imaged by ToF-SIMS from

the topside. Figure 5-3 shows a SI image of such FIB preparation which reveals a significant separation at the interface of the grains which was identified by additional EDS analysis as a respective austenite-ferrite interface. Since the grain at the surface has been identified as ferrite, it can be assumed that during charging deuterium has quickly diffused through this phase and subsequently been trapped (and recombined) at the mentioned interface forming these blisters, in particular, because the diffusion coefficient in the underneath lying austenite grain is significantly lower. Based on that, it can be assumed that the blister size and the occurring crack along the blister are strongly related to the thickness of the ferrite layer at the surface. Therefore a thinner ferrite region might lead to bigger blisters and a larger amount of them. It is anticipated that these high deuterium accumulations then caused or at least contributed to the phase separation at the interface resulting in the respective blistering. It also has to be anticipated that such blistering further strained the ferrite grain above which has been fully saturated and respectively been degraded by deuterium.

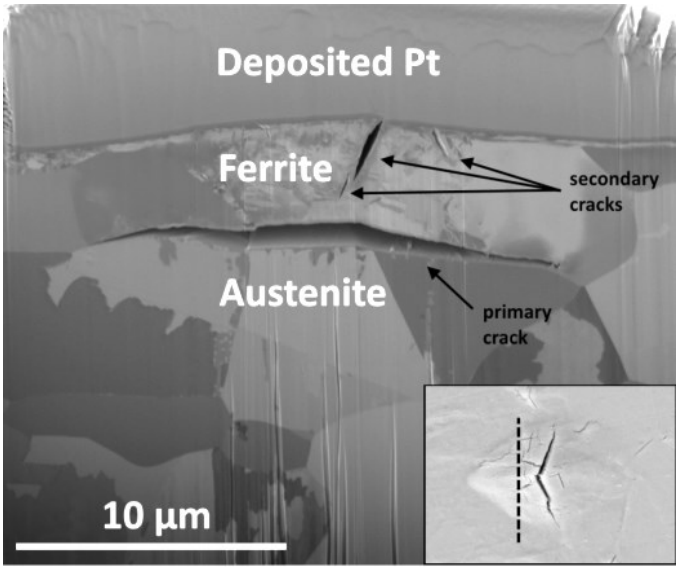

Figure 5-3: Total SI image of a FIB cross section normal to a micro-crack observed on the surface of the charged DSS sample. The FIB cut was taken from a different area on the sample than the one displayed in Figure 5-2. The FIB cut position is shown in the inset. A separation along the interface between the phases is clearly visible. The inner pressure in the blister caused the formation of secondary cracks in the ferrite. The deposited Pt layer is necessary for FIB and the phase characterization was done by EDS.

Since the highest deuterium accumulations have been detected by ToF-SIMS in cracked regions as compared to the surrounding regions in the ferrite (as shown in Figure 5-2 by the yellow regions compared to the surrounding areas colored in purple), it cannot be excluded that such deuterium saturation in the ferrite phase also initiated micro-strains, as reported by Szummer et al [195], for instance. The degradation of the ferritic phase through the formation of blisters in the 2205 grade is associated only with the hydrogen diffusion. Charging experiments conducted by Michalska et al. [196] in 3.5% NaCl solution in 10mA/cm^2 for 7 days showed the formation of blisters in the ferrite phase (Figure 5-4).

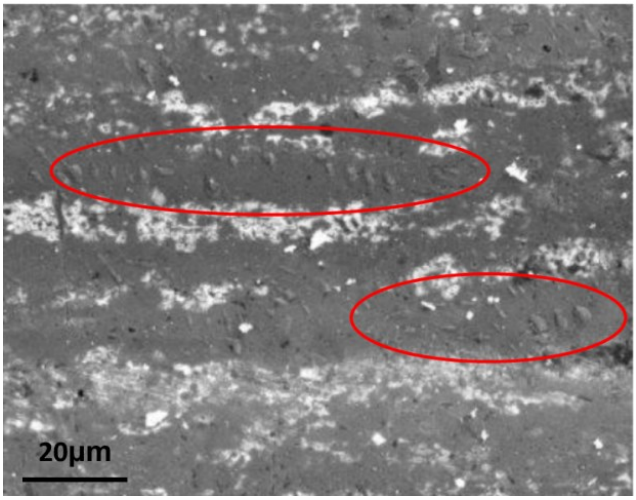

Figure 5-4: Michalska polarization test of a 2205 DSS in 3.5% NaCl solution: formation of blisters in the ferritic phase (marked by red ellipses) after charging the material for 7 days with a current density of 10mA cm^{-2}.

5.1.1.3 Deuterium induced twinning, phase transformation and cracking in the austenite

Figure 5-5 shows the data fusion of SEM SE topography data with the SIMS image data treated by PCA. Figures 5-5a and Figure 5-5b are showing the same information although the heat color palette used in Figure 5-5a is replaced by a single color where the D concentration is represented by the density of colored pixels. Major cracks in the austenite phase can be identified where the respective deuterium concentration indicated by the warmer colors is respectively higher than in the surrounding areas. From this image, significant parallel cracking can be observed in the austenite phase. Such phenomenon associated with deuterium saturation of the austenitic phase has already been reported

previously[128]. It has also been observed by Minkovitz, Rozenak and Eliezer[35, 197] utilizing diffraction methods (X-ray and TEM) to provide some evidence for a phase transformation caused by electrochemical hydrogen charging and respective crack initiation and propagation in the induced martensitic phase at room temperature. Glowacka et al.[198] also showed the presence of parallel bcc laths inside the austenitic phase indicating that a phase transformation of the austenite into martensite occurs under the presence of hydrogen. The formation of a thin martensite layer on the austenite related to hydrogen was also reported previously by Narita [34] who suggested a transformation sequence of:

$$\gamma \rightarrow \gamma * \rightarrow \varepsilon \tag{16}$$

where γ is austenite, γ* is a hydrogen-rich FCC phase formed as a result of the γ lattice expansion and ε is the hydrogen induced martensite phase.

Similarly to the ferritic phase, it can be assumed that high deuterium concentrations cause internal strain in the austenitic grains which lead to an increasing number of stacking faults potentially followed by twinning as already been described by Dadfarnia et al.[67]. Higher deuterium concentrations then lead to formation of ε-martensite on the surface[199] and parallel cracks in the austenite underneath the martensite. Transformation induced martensite (hexagonal close packed, HCP) on the surface of the austenitic phase has been verified by respective SEM/EBSD analysis (as shown in Figure 5-5). It turned out that such transformation preferentially occurs where the γ(111) planes are perpendicular to the surface, enabling a transformation of a thin layer along ε(0001). However, cracking associated with deuterium charging of the austenite in the DSS has not only been observed in this predominantly parallel occurrence. Actually, three different regions have been identified in the austenite phase of the investigated DSS that have to be attributed to the various deuterium concentrations (Figure 5-5b).

The first region is represented by non-cracked areas with elevated deuterium concentration (marked by #1 in the Figure 5-5b). The increased deuterium levels are attributed to non-affected ferrite and, in particular, to the higher solubility of deuterium in the austenite in general. The second region is marked by #2 in Figure 5-5b. It occurs around the parallel cracks mentioned above and is characterized by relatively high concentrations of deuterium. The relatively high deuterium concentration in this region can be attributed to the formation of high strains (as in the ferrite) where the deuterium is deeply trapped and/or even to the formation of a deuterium saturated γ* phase. The third region, marked by #3 in Figure 5-5b, has been observed around cracks with relatively low concentrations of deuterium.

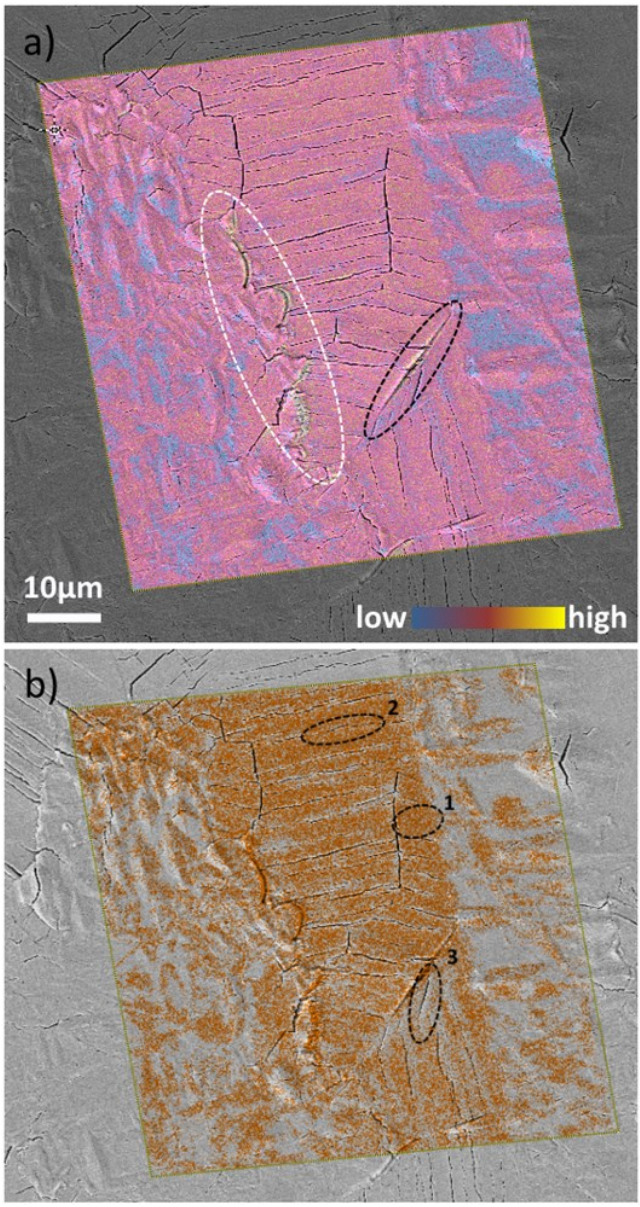

Figure 5-5: Fusion of a SEM topographic image and a SIMS PC1 loadings plot representing deuterium in the microstructure (colored). The highest deuterium concentration was observed around some of the parallel cracks and more significantly around larger cracks marked by a black dashed ellipse in a) and around cracks at the phase boundaries (marked by a white dashed ellipse in a). Regions 1-3 in b) are discussed in text and are indicating on three levels of deuterium concentration in the austenite in cracked and non-cracked areas.

Here it can be assumed that the lower solubility for deuterium in comparison to austenite is due to a phase transformation into a BCC phase with low deuterium solubility, such as ε. The cracks that have been obtained along the ferrite-austenite interface are attributed to the high deformation of the phases due to charging.

The micro-cracks and the plastic deformation of the surface due to blistering in the ferrite together with parallel cracking and the phase transformation in the austenite were sufficient to cause cracks alongside the interface. A theoretical model proposed by San Marchi [123] has shown that when an external load is applied, a crack can propagate through the austenite by the formation of cleavage micro-cracks in the ferrite, another possibility is that the crack can grow along the interface until it links all the cleavage cracks in the ferrite. Mente et al. [200] discussed the crack path in these two cases by finite element modeling. In the case presented here it can be assumed that the cracks along the interfaces are distributed randomly (as it can be seen in Figure 5-6) because no external load was applied.

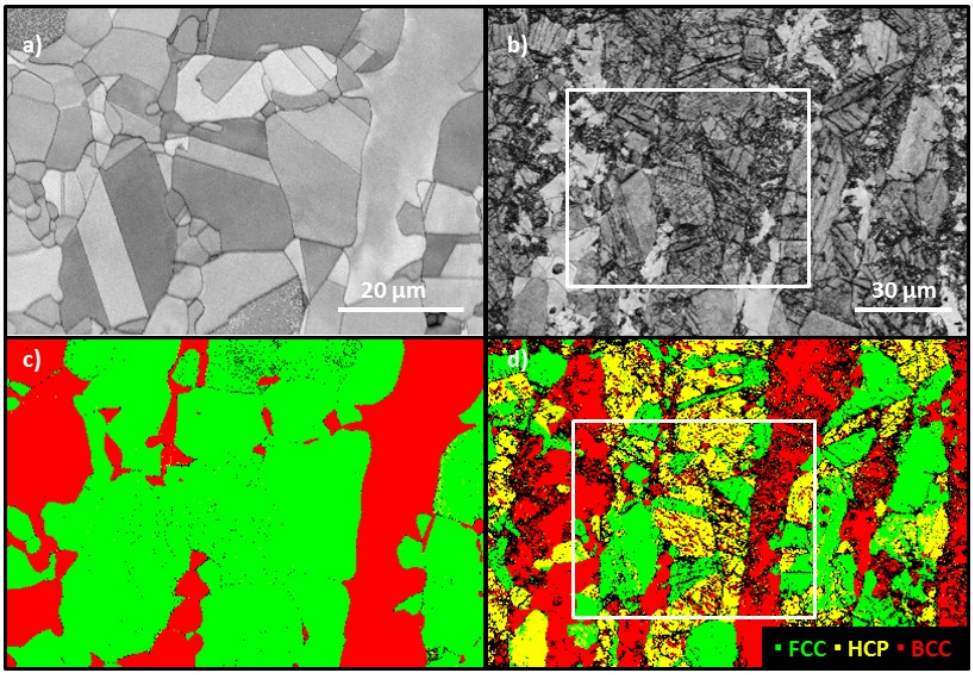

Figure 5-6: SE topographic and EBSD phase maps of the sample before (a and c) and after (b and d) charging with deuterium. The area shown in a and c is marked by a white rectangle in b and d. The changes of the surface are caused by charging.

In addition, it cannot be denied that the cracks and the deuterium induced phase transformation in the austenite are not only due to the diffusion of deuterium into the material during charging but also occurring during the effusion and outgassing of deuterium from the sample thereafter as it was shown by Yang et al.[201]. It must be noted that during charging the sample was losing the mirror quality of the polished surface already after 24 hours. Therefore it is assumed that most of the changes occurred during charging.

The analysis was repeated with another sample with shorter charging time of 60 hours (cf. Figure 5-7). In this case a severe cracking at the ferrite-austenite interface has been observed. The cracks in the δ-γ interface can be attributed to respectively high deuterium accumulations. The ferrite-austenite-interface in DSS 2205 has also been considered elsewhere to attract high hydrogen or deuterium concentrations [58, 202-204]. In this context, the interface has been anticipated as a reversible trapping site, but also as a path for accelerated diffusion [74].

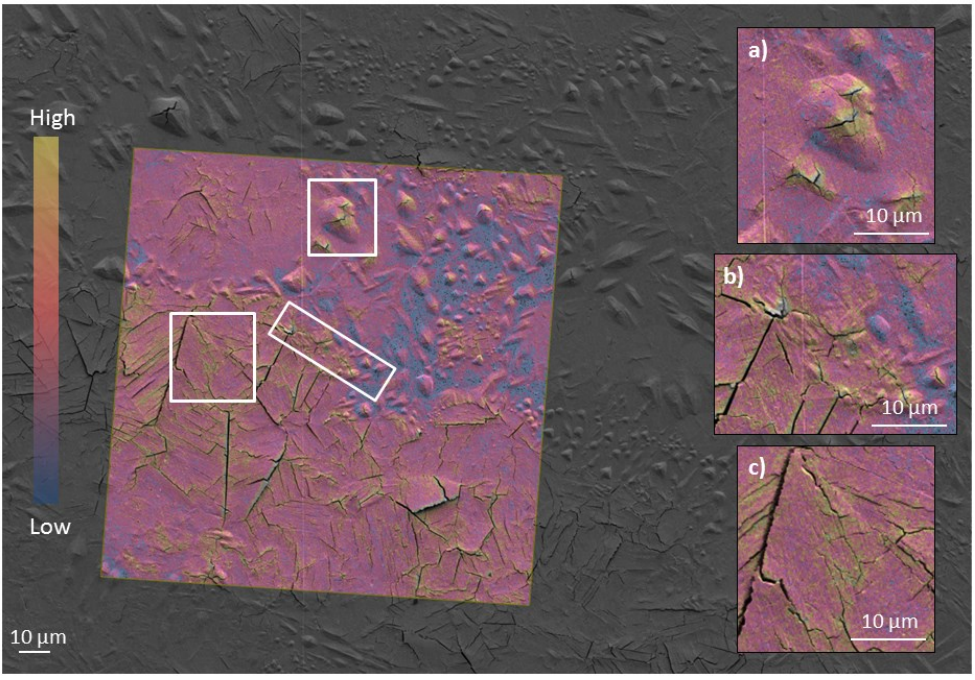

Figure 5-7: Fusion of HR-SEM topographic image with colored ToF-SIMS PCA plots of deuterium in the microstructure. The insets show the local differences in the charging effect and the deuterium concentration in the ferrite (a), ferrite-austenite interface (b), and austenite (c).

However, the data fusion images now provide considerable evidence that the severe cracking at the austenite-ferrite interface is associated with high deuterium concentrations. Furthermore, the deterioration and deuterium assisted cracking in both phases adjacent to the interface has to be taken into account, in a way that the cracks in both phases are linked via the interface [9, 123, 205] The repeatability of the results was proven by examining another sample, however this time, by ToF-SIMS imaging in BA mode. The results from this analysis are shown in figure 5-8 and indicate on the same distribution of deuterium between the phases.

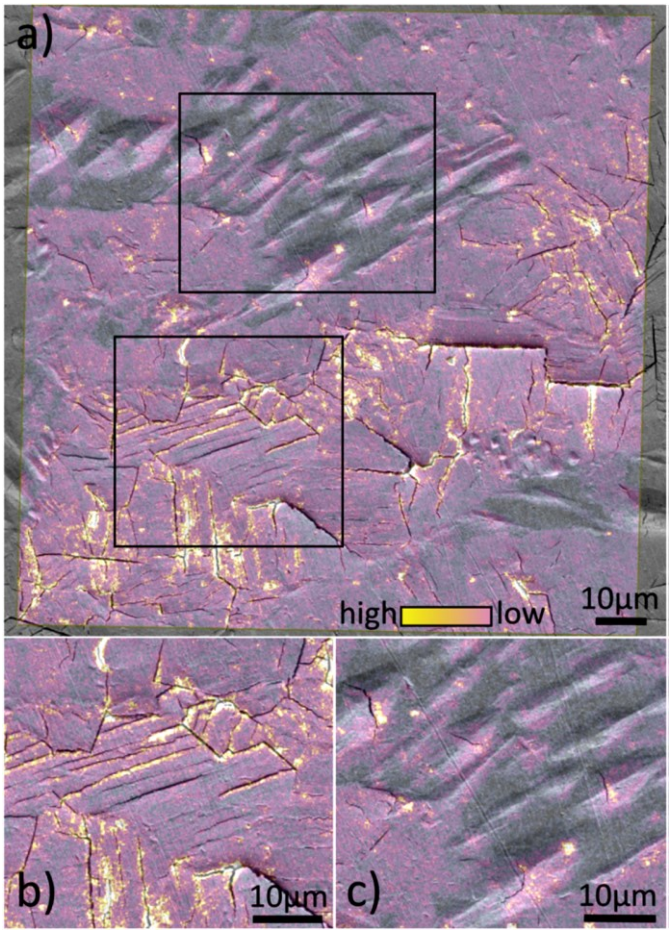

Figure 5-8: Fusion of SEM topographic image data and PC1 loadings plots obtained by principal component analysis (PCA) of ToF-SIMS image data representing deuterium in the microstructure (colored). The images show the local differences in the deuterium concentration in the austenite (b) and in the ferrite (c).

5.1.2 Lean duplex 2101

The main progress in the current experiment was the ability to elucidate the hydrogen distribution and the correlation to the induced structural changes obtained with EBSD on the same area of interest. This powerful combination was shown in this work for the first time. Figure 5-9 shows the pattern quality and the EBSD phase map before and after charging. The damage to the surface can be easily seen in the pattern quality image. The phase maps show that most of the austenitic phase has been transformed into defect rich BCC phase after charging whereas in the ferrite the damaged regions are mainly seen on and around tent shaped blisters. The formation of the blisters was followed by the formation of differently oriented regions on the blister's surface within the former ferritic grain. This process can be explained by a grain refinement or by a phase transformation of the ferritic phase due to the large deformation of the material in this area.

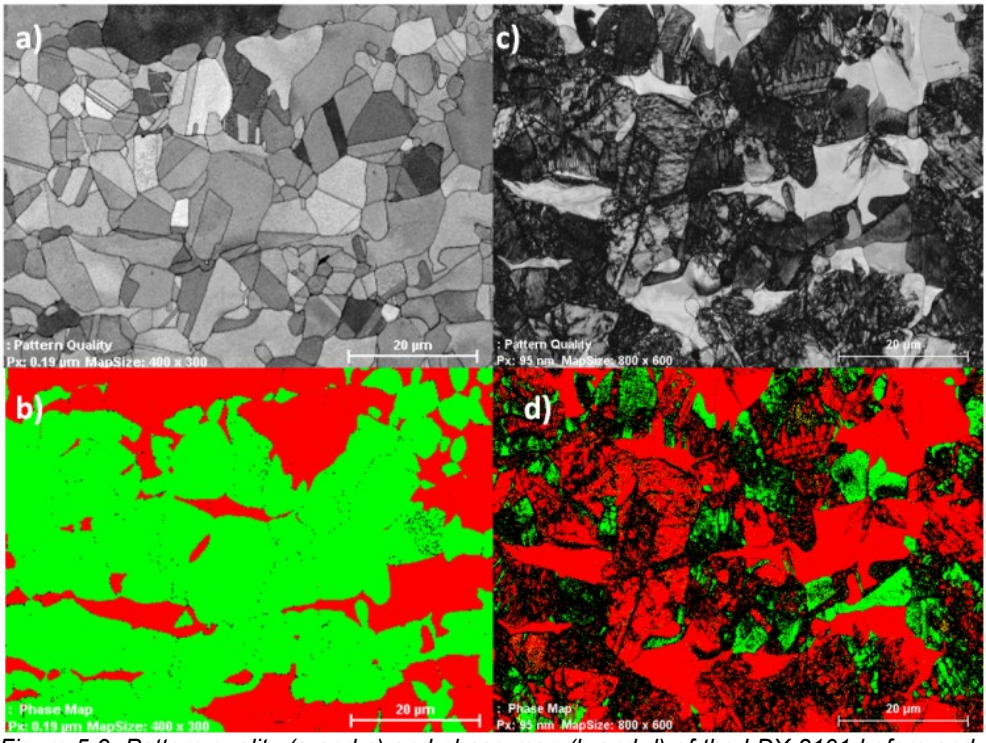

Figure 5-9: Pattern quality (a and c) and phase map (b and d) of the LDX 2101 before and after 72 hours of charging the specimen with deuterium. The red and green colors in the phase map indicate the BCC structure and FCC structure, respectively.

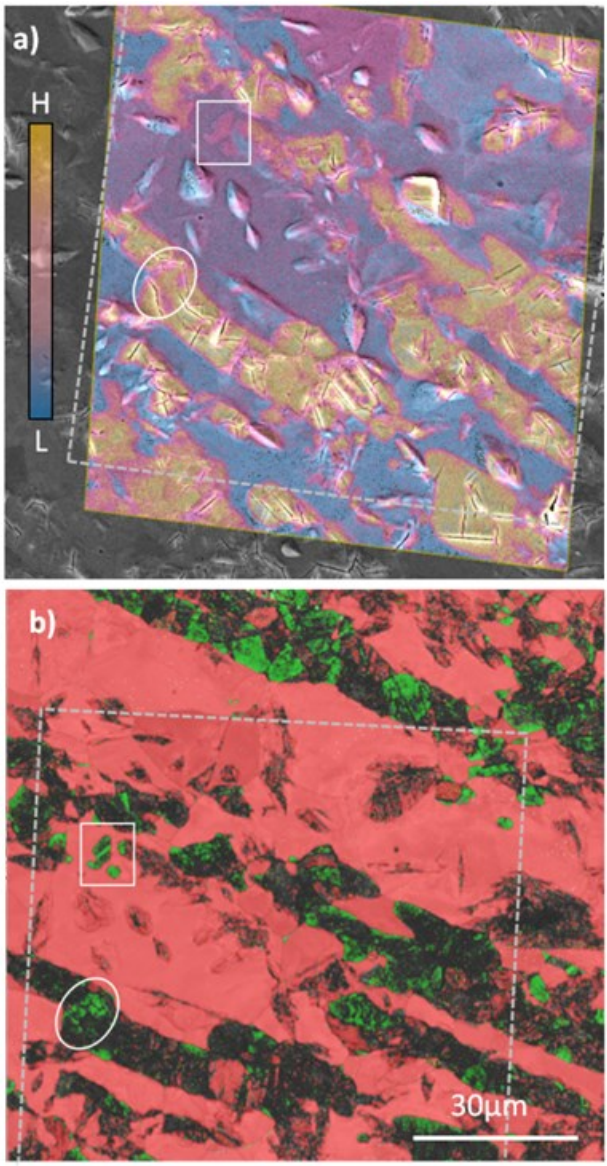

Figure 5-10: a) Data fusion of a SEM topographic image and a SIMS PC1 loadings image plot representing the deuterium distribution in the LDX 2101 after 72 hours of charging (deuterium concentration indicated by the warmer colors) and b) an overlay of the EBSD phase map (red: BCC, green: FCC) on the pattern quality image. The ToF-SIMS image was taken from an area of 100x100µm. The dashed gray lines indicate these parts of the images which can be compared one by one. The white circle and rectangle indicate regions with lower concentration of deuterium and where less austenite had been transformed into BCC martensite.

The fine grains obtained on the surface of the blister have a twin relation and therefore it is assumed that multiple twinning was leading to a grain refinement. The formation of blisters through the formation of micro twins and grain refinement in the ferrite was already reported by several authors for ferritic and DSSs.[194, 195, 205] However, in comparison to the 2205 DSS, in the LDX no cracks were observed in the ferrite-austenite interface. Noteworthy is that the cracks in the interface might be indistinguishable in this direction of analysis (TD). The higher deuterium concentration obtained on the surface of the blisters (as it is shown in the ToF-SIMS image in Figure 5-10a) is also contributed to the significant straining process of the surface during the diffusion of deuterium into the bulk.

A similar observation had been shown earlier with the standard 2205 DSS sample. It was previously shown for the 2205 DSS, that after electrochemical charging austenite has been transformed into HCP martensite only in grains and twins with a specific orientation and that the degradation was also accompanied by the formation of parallel cracks in the austenite phase.[205] However in the LDX2101 most of the phase transformed into BCC phase and almost no parallel cracks were obtained on the surface.

HCP martensite was also obtained in the former austenite but locally and in much smaller portions as it is shown in Figure 5-11. The high density of defects mainly in the austenite (indicated by the dark regions in the phase maps in Figure 5-9) is contributed to the deuterium induced high stresses in the surface layers. It is hard to figure out when most of the transformation occurred, during charging or between SIMS analysis and EBSD characterization (where deuterium was effusing from the sample). However, this transformation is followed by a loss of the mirror-quality of the sample's surface and the formation of cracks during charging. During EBSD measurements no ε↔α'↔α transformation was observed.

Figures 5-10 and 5-12 show the deuterium distribution and the related new microstructure at two different positions on the sample at different magnifications. The images suggest that no phase transformation occurred in regions of the austenite with lower concentration of deuterium whereas high concentrations of deuterium lead in most cases to a formation of the BCC phase.

In regions of the austenitic phase close to the ferrite-austenite interface, the variance in deuterium distribution was more pronounced. By the comparison of the chemical image (Figure 5-10a) and the phase map (Figure 5-10b) it can be seen that the deuterium concentration in the center of the austenitic phase is varying in the higher values (light pink to yellow) and surrounded by a kind of medium deuterium concentration (pink) strip. This

also emphasizes the relation between the deuterium distribution and the resulted phase transformation in the former austenite since most of the remaining austenite is observed mainly close to the phase boundaries.

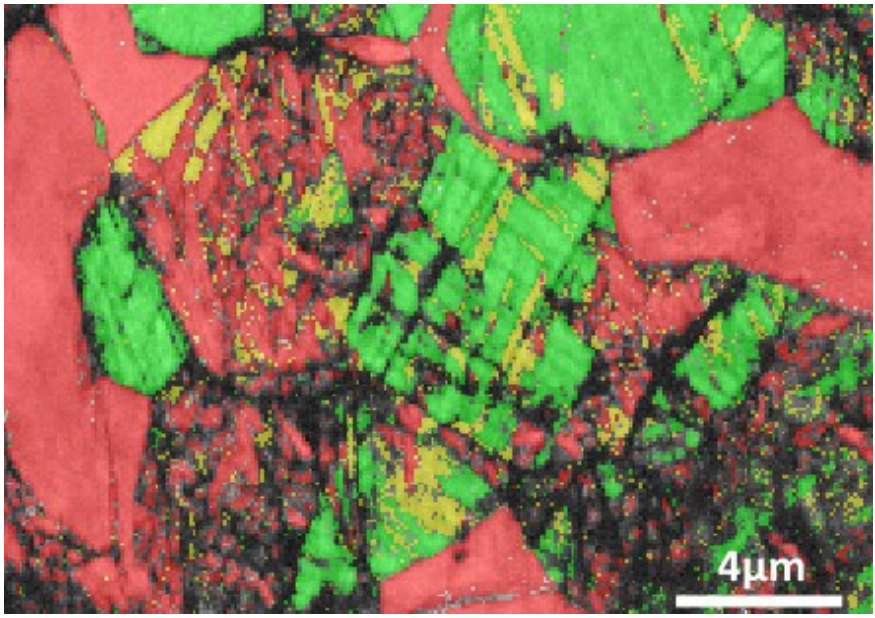

Figure 5-11: Overlay of the EBSD phase map (red: BCC, green: FCC, yellow: HCP) and the pattern quality image. The transformation of FCC into HCP and BCC was obtained in defect rich regions, the former ferrite was less affected by charging, except for the formation of blisters in this phase.

It should be highlighted that the formation of the BCC phase in the austenite was not necessarily accompanied by a massive cracking and topographic changes of the surface as it can be seen in Figure 5-12 (indicated by a white arrow). Therefore, the interpretation of the deuterium effect cannot be done only by consideration of topographic changes but must be supported by local structure characterization, too.[69] The relation between hydrogen charging and the structural changes in this grade were already shown [206] by the use of thermal desorption spectroscopy (TDS), X-ray diffraction (XRD) and optical microscopy (OM). A combination of these methods did not provide spatially resolved information about phase transformations.

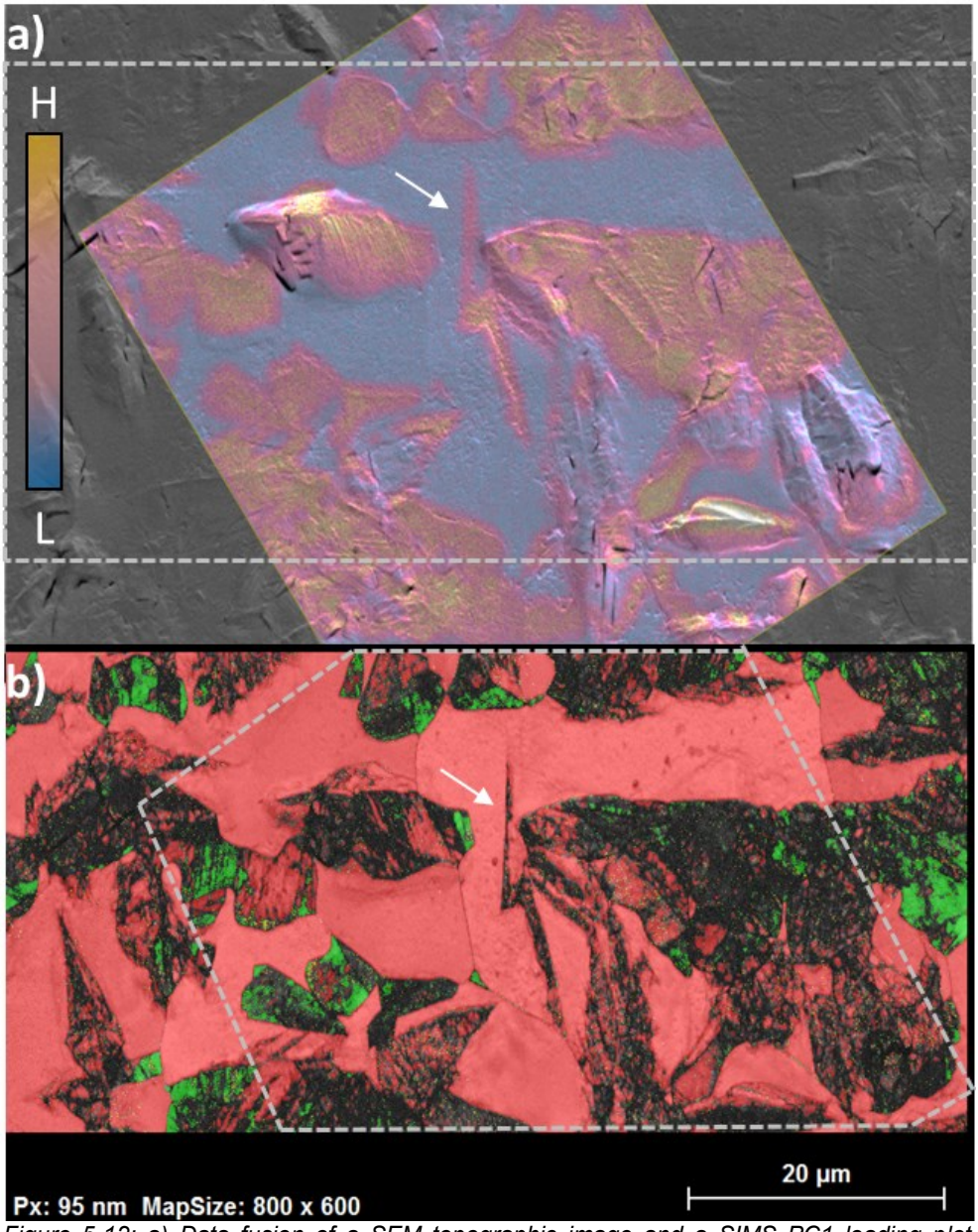

Figure 5-12: a) Data fusion of a SEM topographic image and a SIMS PC1 loading plot representing deuterium in the microstructure of a LDX 2101 after 72 hours of charging and b) phase map of the same region. The ToF-SIMS image was taken from an area of 50x50µm. The dashed gray lines indicate these parts of the images which can be compared one by one.

However, it has been demonstrated that in LDX 2101 the austenite phase was more susceptible to α'/ε transformation than DSSs with higher Ni content. The proposed mechanism for the phase transformation was:

$$\gamma \rightarrow \varepsilon \rightarrow \alpha' \tag{17}$$

The presented results support this mechanism, and the assumption that the austenitic phase become less stable as the amount of Ni is reduced.

It can be assumed that the use of hydrogen instead of deuterium might result in less BCC phase on the surface since deuterium induces higher strains in the metallic lattice. On the other hand, it was shown that with similar charging parameters mainly the HCP phase was obtained in the 2205 DSS. The repeatability of the results was examined by analyzing another sample, however this time by ToF-SIMS imaging in BA mode. The surface of this specimen exhibited less severe cracking. Figure 5-13 shows that also here the cracking is associated with significant deuterium accumulations.

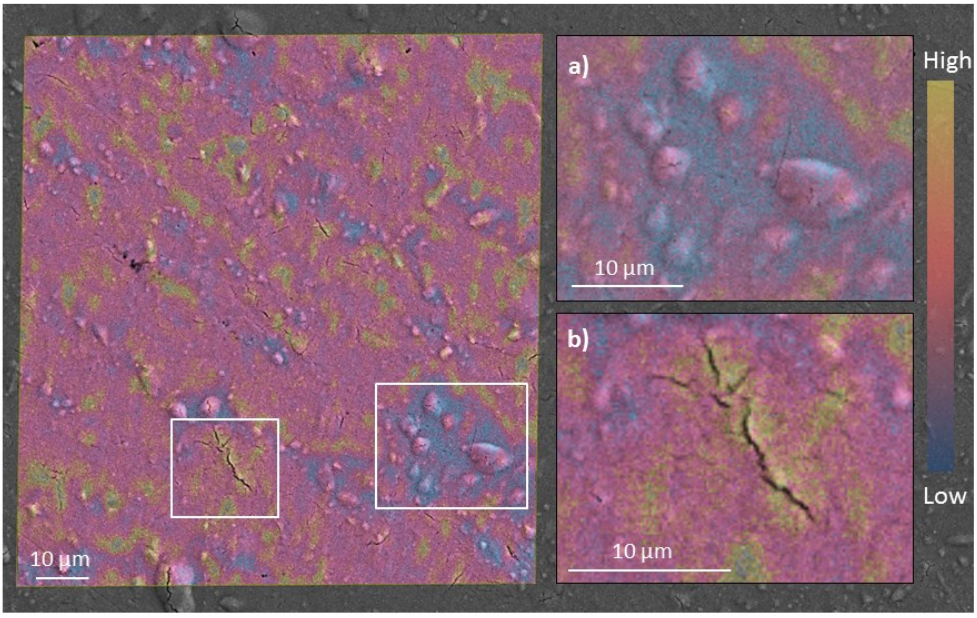

Figure 5-13: Fusion of HR-SEM imaging with colored ToF-SIMS PCA plots of deuterium in a LDX microstructure, a) Magnification of the ferritic phase showing blistering and respective cracking to a smaller extent than in DSS 2205, b) Magnification of small cracks in the austenite phase that differ from the parallel orientation observed for the DSS 2205

Such observations in a lower spatial resolution of the ToF-SIMS measurements are thus confirming again that data fusion imaging represents a valuable tool to visualize and elucidate the effects of hydrogen or deuterium on microstructural changes and cracking.

It was shown in chapter 2.6.3 that imaging of the deuterium distribution in the microscale is possible, even with better resolution, by some other methods such as silver decoration or scanning kelvin probe. However, these methods require additional preparation of the sample that in some cases does not allow further analyses by another method therefore structural characterization might not be achievable on the same ROI allowing the direct correlation between the deuterium distribution and the resulted structural changes. Moreover, the combination of structural and chemical analyses was already made by the use of dynamic SIMS before.[129] However, in this case the primary ion flux that is aggressively eroding the surface might deliver better spatial resolution but is also induces a massive change of the surface topography within very short time.

5.2 In-situ permeation experiments

For the first time an in-situ permeation and ToF-SIMS experiments have been combined The principle has been demonstrated in a previous study[128, 169, 177] (cf. Figure 4-12). The setup can be regarded as a Devanathan-Stachurski permeation cell where the cell itself is made of the investigated material. The microstructure has been imaged at the outer surface of the cell which is located within the ultra-high vacuum chamber of the ToF-SIMS instrument. This setup avoids any impact of the electrolyte on the imaged surface as it was shown for the ex-situ static experiments.

The DSS surface has been investigated with increasing time of charging: First deuterium secondary ions were detected after 28 days of charging, saturation after 37 days. The limited sensitivity of SIMS (secondary ion emission probabilities may be small as 10^{-4}) leads to an underestimation of the “break-through” time which is the time of charging required for detecting the first intentionally introduced deuterium on the analyzed surface. To gain a maximum of information from the SIMS image data acquired multivariate data analysis by Principal Component Analysis (PCA) has been performed. By using key co-variations between element and fragment secondary ions the image contrast between features is substantially increased. In comparison to a previous SIMS study of deuterium effusion from the DSS sample reported by the authors[128] the steps beyond in the present experiment are:

- The real time monitoring of the permeation, diffusion and distribution of deuterium in individual phases of the DSS microstructure and
- The multivariate treatment of SIMS image data.

Results of the in-situ permeation experiment are displayed in Figure 5-14. Figure 5-14a shows the scores image for the first principle component (PC1) obtained from the positive secondary ion data set comprising matrix related secondary ions. The related loadings plot (Figure 5-15a) indicate Ni^+, Mn^+ and Fe^+ as key secondary ions that characterize the variance captured by PC1 obtained from the positive secondary ion data set. Thus the different phases in DSS can clearly be distinguished. The ferrite appears dark and the austenite appears bright.

Figure 5-14b exhibits the PC1 scores image delivered by PCA of the negative secondary ion data set where deuterium related secondary ions contribute to. In this case the related loadings plot (cf. Figure 5-15b) indicates D- and OD- as key (fragment) secondary ions that characterize the variance captured by PC1.

By comparison of Figures 5-14a and 5-14b, a preferential deuterium accumulation in the ferrite phase becomes evident. For single grains inside austenite and ferrite phases, intensity variations in Figure 5-14b have been observed. This observation is assumed to be due to:

1. The dependency of the secondary ion emission probability of deuterium related secondary ions on the respective grain lattice plane exposed to the impinging primary ions.
2. The relation between the grain orientation and the diffusion rate of deuterium in this direction as shown by Hua et al. [69]

Based on Figures 5-14a and 5-14b, a higher permeation of deuterium and faster saturation of the ferrite phase becomes very obvious in contrast to the austenite phase. This experimental result is consistent with literature data, where deuterium in the ferrite phase is reported to have an about five orders of magnitude higher diffusivity[9, 56, 130]. By this, the current in-situ measurements provide evidence to previous statements[9, 57, 58] based on models and experiments that deuterium preferentially diffuses through the ferrite matrix. It has to be anticipated that within the time frame of the reported experiment, only a minor amount of deuterium will be diffusing into and trapped in the austenite phase grains located at the outer surface of the electrochemical DSS permeation cell considering the diffusion coefficient of deuterium in this phase.[57]

Reduction of the negative image data matrix used for score images displayed in Figure 5-14b by the use of only a mass range 20-50 m/z reveals images shown in Figures 5-14c and 5-14d. Figure 5-14c presents an image of the scores of PC1 where significant positive loadings have been found only for m/z=26, i.e. CN^- fragment ions (cf. Figure 5-15c). Comparison of Figure 5-14c with Figure 5-14a reveals that these occur in areas corresponding to the austenite phase. Moreover, the comparison of Figure 5-14c with Figure 5-14b reveals that certain regions in the ferrite phase where a brighter (or, more correct – less dark) region related to CN^- correlates with a bright area representing high deuterium concentrations. In general, carbon and nitrogen have higher solubility in the austenitic phase. Nitrogen can be hardly detected by itself whereas the CN signal is easily detected by the ToF-SIMS in the negative mode. It can be assumed that the occupation of interstitial sites with C and N in the ferritic phase increase the affinity for deuterium.

Additionally, only in this experimental setup, eliminating the exposure of the analyzed surface to the electrolyte, enables to distinguish the phases by the CN signal in the negative mode and simplifies the characterization process.

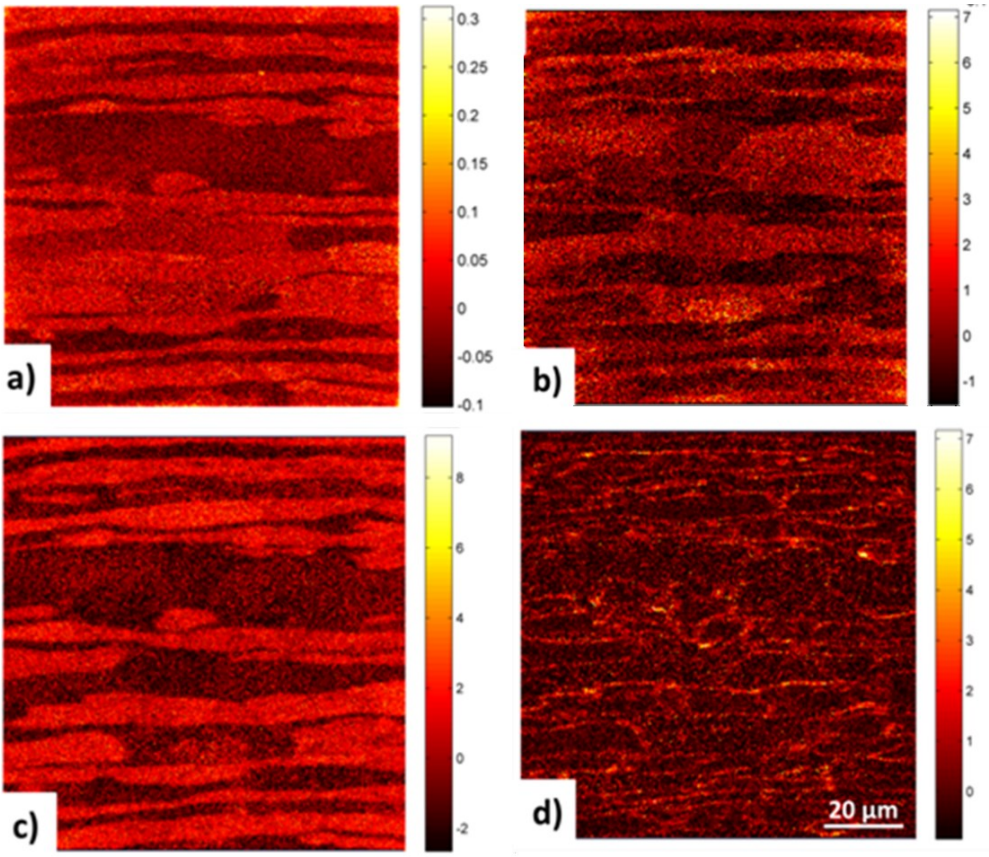

Figure 5-14: a) Principle component score images of the ToF-SIMS data sets acquired after 34 days of charging. (a) PC1 scores image for identifying phases using the positive ToF-SIMS data set acquired after 34 days of charging DSS with deuterium by using a peak list with secondary ions covering the main alloying elements. The bright regions represent the austenite phase (as proved by the loadings plot in shown Figure 5-15a. (b) PC1 scores image identifying locations rich in deuterium obtained from the negative SIMS data set acquired after 34 days and using the full peak list. Bright pixels indicate positive scores and correlate with the ferrite phase. (c) PC1 scores image obtained from the same data set but using a different peak list prepared to focus on carbides and nitrides. This image is identifying locations rich in N and C. Bright pixels indicate positive scores and correlate with the austenite phase. (d) PC2 scores image identifying locations rich in N, C and D (bright pixel means positive score) indicating graded accumulation of deuterium at the ferrite and austenite grain boundaries and at the ferrite/austenite interface (highest scores!) as well.

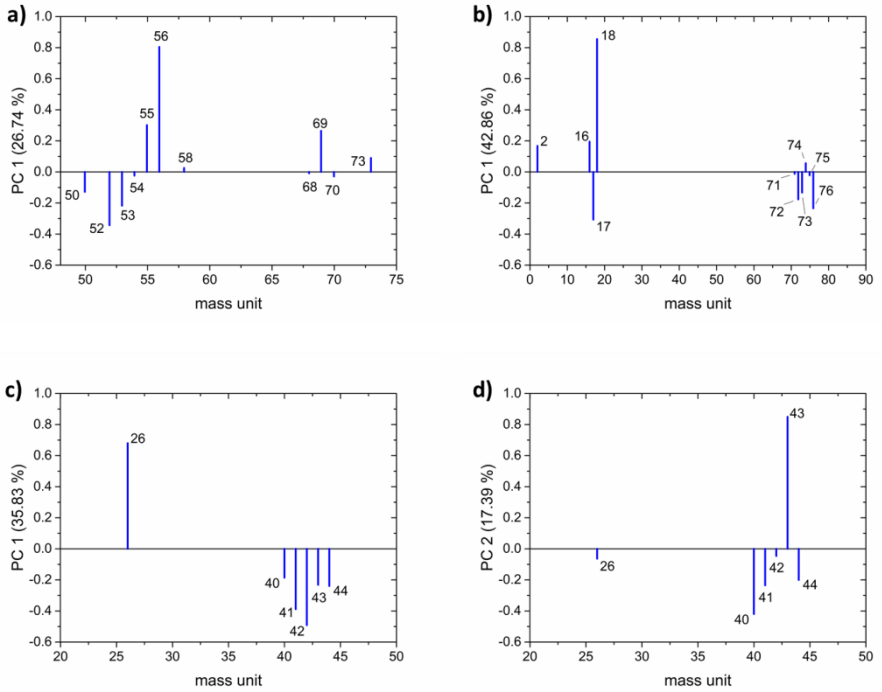

Figure 5-15: Principle component loading plots from PCA corresponding a) to the scores in Fig 5-14a and 5-16a; b) to the scores in Fig 5-14b and 5-16b; c) to the scores in Fig 5-14c; d) to the scores in Fig 5-14d. For the interpretation of the peaks the reader is referred to Table 12.

Figure 5-14d displays the PC2 scores image belonging to the PC1 image in Figure 5-14c. The loadings plot for PC2 shows strong positive loading exclusively at m/z=43 assigned to CN_2HD^- (cf. Figure 5-15d) and displays distinct positive scores at grain boundaries within a specific phase and high positive scores at ferrite-austenite interfaces. This image provides evidence that regions at the grain boundaries and interfaces contain carbon and nitrogen as well as accumulated deuterium at the same time. Such findings might indicate that grain and phase boundaries act as trapping/sink sites in the microstructure and thus attract hydrogen or deuterium ions. [71, 207, 208]

The SIMS data sets leading to images displayed in Figure 5-14 have been taken from region of interest selected at the beginning of the in-situ permeation experiment which has been analyzed many times before to identify the break-through of deuterium. To rule out any unintended measurement artifacts (e.g. due to beam damage) a fresh ROI was selected for ToF-SIMS imaging after 37 days of charging (shown in Figure 5-16).

Again, the ferrite phase appears dark and the austenite bright in Figure 5-16a (PC1 obtained from the positive secondary ion data set). Also, the significantly higher deuterium concentration in the ferrite grains in comparison to the austenite has been confirmed by Figure 5-16b (PC1 obtained from the negative secondary ion data set). Similar results to those obtained after break-through of deuterium have been found for the saturated state. Additionally an ion-induced secondary electron image (Figure 5-16c) of the DSS microstructure at the new ROI is taken where also phase and even grain boundaries can be distinguished.

Principally, the in-situ permeation experiment can enable also a determination of diffusion coefficients. Unfortunately evaluation of such values will suffer from systematic errors. The most influential uncertainty in the measurement is the detection limit of the SIMS instrument for deuterium and the tortuous effect occurring in a two phase alloy. [57, 58] However, it becomes obvious that most of the deuterium detected at the time of the break-through permeated predominantly through the ferrite phase on paths circumventing the austenitic phase (cf. ref. [57]) characterized by considerably lower diffusivity and higher solubility for deuterium.

It has been demonstrated for a technically relevant multiphase metallic microstructure, here DSS, that imaging ToF-SIMS together with subsequent image data treatment by PCA is a powerful tool for phase identification (positive SIMS mode) and in-situ visualizing the deuterium distribution (negative SIMS mode). The in-situ approach using a deuterium charging cell in the analysis chamber of a ToF-SIMS instrument provided clear experimental evidence for a preferred diffusion of deuterium through the ferrite phase, while ex-situ SIMS studies could only show preferential accumulations in the phases subsequently to charging with hydrogen or deuterium. [72, 192]

The experiment also enables an investigation of interactions of deuterium with grain and phase boundaries, carbon and nitrogen in the DSS microstructure. At this point, it addresses the diffusion and permeation of deuterium through the microstructure without any external mechanical loading on the specimen. The results shown in this experiment were supported by respective numerical simulations of hydrogen diffusion in the rolling direction (Figure 5-16d).

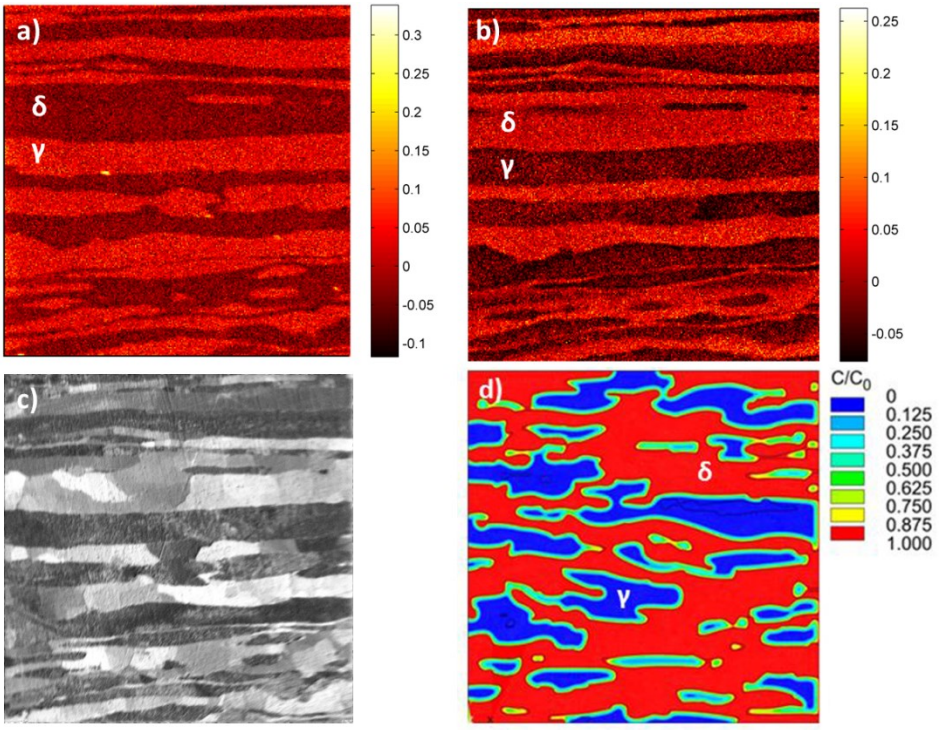

Figure 5-16: (a) PC1 scores image obtained from the positive SIMS data set acquired after 37 days of charging DSS and used to identify phases in the DSS micro structure. A fresh region of interest (ROI) has been selected. The bright regions represent the austenite phase (as shown in the loading plot in Figure 5-15a). (b) PC1 scores image related to locations rich in deuterium. The image was generated by PCA of a negative ToF-SIMS image data set obtained after loading with deuterium for 37 days. The bright deuterium-rich areas have positive scores and correspond to the ferrite phase while the dark areas have negative scores and relate to austenite grains. (c) Ion induced secondary electron (SE) image of displaying grains in the DSS microstructure at the selected region of interest. (d) Mente et al. [9] numerical simulations of hydrogen distribution in a DSS 2205 microstructure showing that an interconnected ferrite phase is acting as fast permeation track by a 2-D modelling of the diffusion of hydrogen in a DSS microstructure. Figures a-c are taken from the same area of 100x100 μm^2.

This experiment provided the motivation to develop an experiment designated to the realization of an in-situ mechanical loading of deuterium charged specimens to study the degradation of each phase in DSSs by ToF-SIMS imaging. This experiment contributed to a better understanding of hydrogen and deuterium permeation, transport and trapping in metallic microstructures. It should be mentioned that the in-situ ToF-SIMS experiment shown here is part of recent community overarching activities to develop new experiments carried out, e.g. on the big and flexible sample holder within the analysis chamber of ION TOF's ToF-SIMS instruments (e.g. microfluidic device for in situ ToF-SIMS analysis of the Liquid/Vacuum interface shown by Yang et al. [209]).

5.3 In-situ mechanical loading experiments

As another in-situ approach – Mechanical loading has been carried out while analyzing a charged 2205 DSS microstructure by ToF-SIMS. The in-situ mechanical loading experiment was conducted several times for optimizing the prototype sample holder, the sample and the acquisition parameters. The results were obtained by ToF-SIMS imaging of the deuterium distribution in the electrochemically hydrogenated standard DSS microstructure in two experiments. In both experiments the samples geometries were identical:

1. The sample was imaged before applying any load, thereafter the cooling was stopped and the sample was loaded mechanically by applying maximal voltage on the actuators at -47°C. The sample was reconnected to the cold finger and imaged 100µm ahead of the notch (Figure 5-17) after stabilizing the temperature at ~-80°C in the CBA mode of the instrument.
2. The sample was imaged before applying any load, then after applying low, medium and maximal load above -50°C (as described above). The images were taken 5µm ahead of the notch (Figure 5-19a) in the BA mode of the instrument. With identical acquisition parameters for the images taken after applying the load (time and area).

As described before, the imaging modes of the ToF-SIMS require longer acquisition time (120-240 minutes) to obtain a good signal-to-noise ratio in comparison to the high mass resolution mode (HCBU) due to the lower current of the primary ion beam in these modes. Another issue to be considered is the relatively high temperature of the sample holder during imaging that does not allow long acquisition time. The loss of deuterium during applying the load gives approximately a time window of 30-60 minutes for acquiring the images.

For these reasons, the experiments were conducted in two parts. During the development of the experimental procedure, it was realized that although there are no strain-induced detectable cracks at the surface, the data fusion of the SEM image with the images acquired before applying the maximal load is not applicable due to a large mismatch resulted by the plastic deformation of the sample. However, the distortion was reduced in larger distance from the notch enabling the data fusion as it is shown in Figure 5-17.

The images taken in the initial state where no load was applied on the sample (cf. Figure 5-17a and 5-19a) show the same distribution that was observed in the ex-situ mechanically unloaded samples. The images exhibit a higher deuterium signal in the austenitic phase (light red to yellow) than in the ferritic phase (purple to blue). Since the

samples for this experiment were charged in the same way the ex-situ static samples were charged, it is obvious that although both phases were charged, the higher concentration of deuterium in the austenitic phase is clearly in this state. After application of the maximal load on the sample a redistribution of the deuterium was observed. Figure 5-17 shows that with increasing distance from the notch the deuterium redistribution is less significant. This process can be attributed to:

1. An artifact of the imaging process due to the tilt of the sample during applying the mechanical load.
2. Significant higher mobility of deuterium atoms above ca. -58°C as described in chapter 5.1.1.1.
3. Strain-induced redistribution of deuterium that takes place as it was simulated and macroscopically described by Lufrano et al. [210, 211] and Yokobori et al. [212]

As it was described, the raw intensity delivered by ToF-SIMS is extremely sensitive to the topography of the surface and to the secondary ion yield (matrix effect). Similarly to the other experiments, in order to minimize these effects, the raw data was normalized to the total intensity and scaled. The efficiency of the data pre-processing can be easily evaluated by comparing representative masses before and after applying the mechanical load after the data processing was applied. The efficiency of the data treatment was validated for these experiments by the evaluation of O^-, FeO^- and CN^- in addition to the H^- and D^- related peaks (cf. Table 12). These masses were selected due to their varying intensities, O has the highest intensity, FeO^- has a moderate intensity and CN^- (in this type of charging due to the interaction between the electrolyte and dissolved N at the steel surface) has a relatively low intensity. The comparison of the data taken before to the data taken after applying the mechanical load have shown no changes in the CN^-, FeO^- and O^- secondary ion yield whereas the hydrogen and more intensively – the deuterium, showed significant changes. Therefore it is assumed that the redistribution occurs due to the strain induced diffusion of the deuterium.

The redistribution of deuterium is accompanied with the blurring of the phase boundaries in some regions of the SIMS images as it was shown in the ex-situ static analyses of the mechanically non-loaded samples in chapter 5.1.1.1 (Figure 5-1). However, here the intensity of the saturated austenite does not decrease and the intensity of the ferrite increases after applying the load. Therefore, it is assumed that in addition to the enrichment of the deuterium close to the crack tip also a redistribution of deuterium between the phases takes place due to the higher mobility at the temperature the mechanical load is applied.

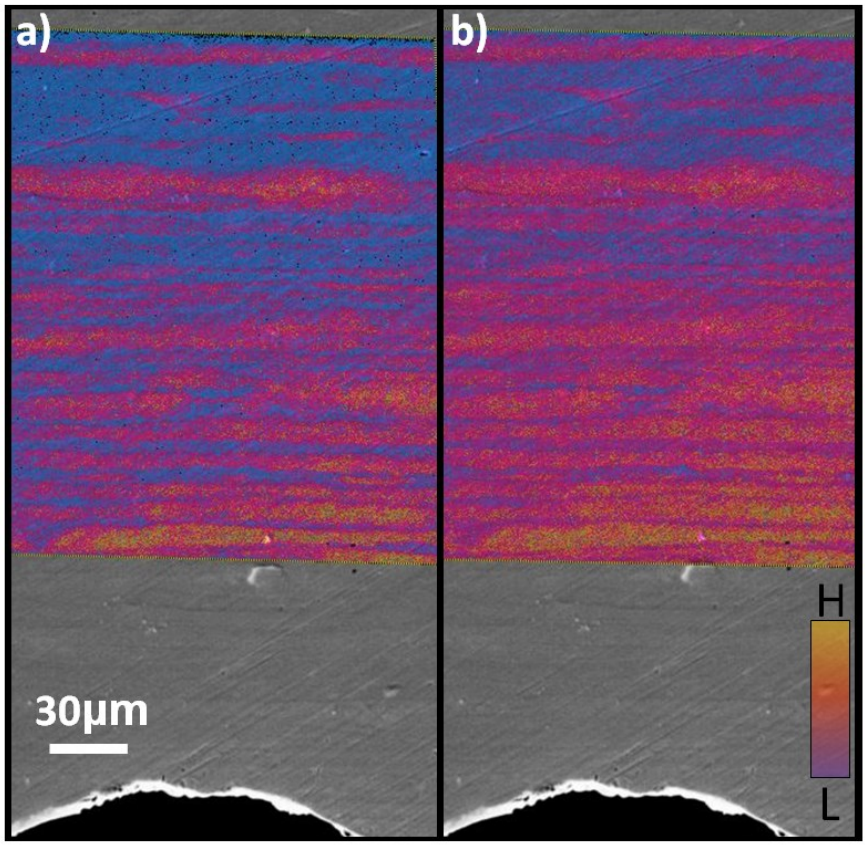

Figure 5-17: Fusion of a SEM topographic image and a SIMS PC1 scores plot representing deuterium in the microstructure (colored) of a standard 2205 DSS (a) before applying any mechanical load and (b) after applying a maximal load by the actuators. The brighter regions represent the austenite. The SEM image was taken after the SIMS analyses.

The experiment was repeated with another sample under different loads. This time a smaller area closer to the notch (~5 microns) was selected. The multiple warm-ups of the sample and a smaller area required a faster acquisition process. Therefore, the sample was imaged in the BA mode of the ToF-SIMS. Figure 5-18 shows a SEM image of the notch taken after the SIMS analyses. The identification of the phases was performed by the type of microstructural damage of each phase.

In-front of the notch there is an austenitic strip. It is assumed that the crack in the center of the notch was initiated by charging due to the high concentrations of deuterium in this phase and the degradation of the austenitic phase, as it is described in results of the ex-situ experiments. Figure 5-19 shows the scores image of PC1 representing the deuterium

related signal in different steps of the experiment (by combing Figure 4-16b). Figure 5-19b shows the deuterium distribution before applying the load. The deuterium enhancement is obtained in the closest area to the notch for the first time after applying a medium load on the sample (Figures 5-19d and 5-19f). This enrichment is observed more clearly after applying the maximal load on the sample (cf. Figure 5-19e and 5-19g). The shift in Figures b-g is due to the removal of the sample from the cold finger (and the analyzer) for warming up and applying the mechanical load.

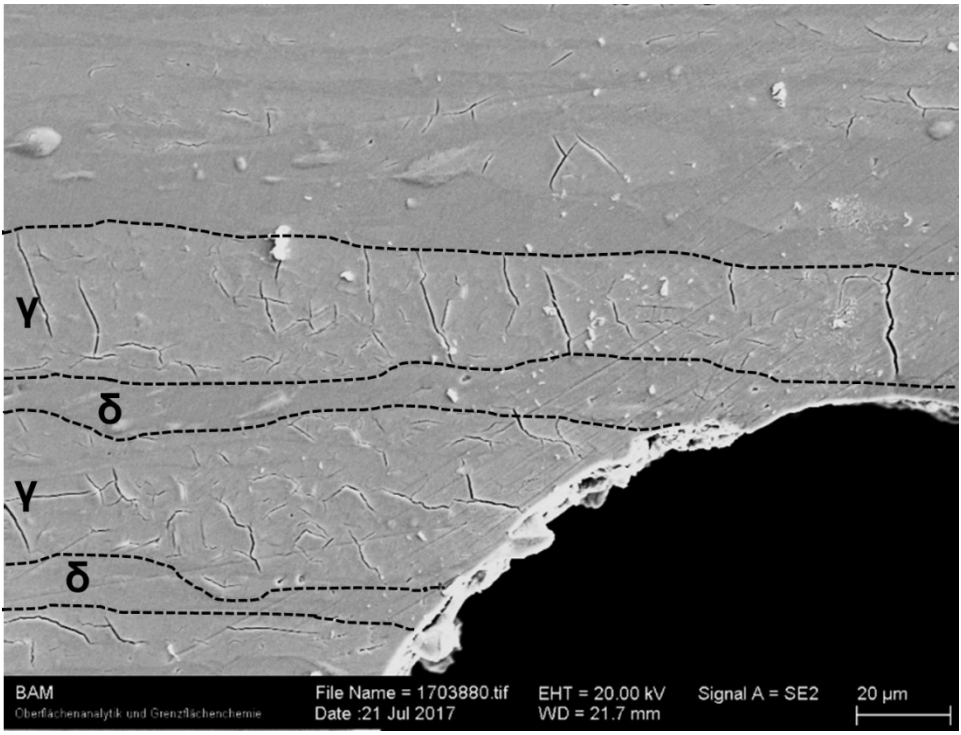

Figure 5-18: SE image of the second sample after ToF-SIMS in-situ mechanical loading experiments.

Moreover, Figure 5-19g shows the highest in-homogeneities in the first layer (austenite) in front of the notch. It can be assumed that these in-homogeneities are attributed to the enrichment of hydrogen around the cracks. In the first sample, (Figure 5-17) no cracks were observed on the analyzed surface unlike in the second sample (Figure 5-18). In addition, with decreasing distance from the notch, cracks at the surface of the sample show a preferred orientation towards the notch.

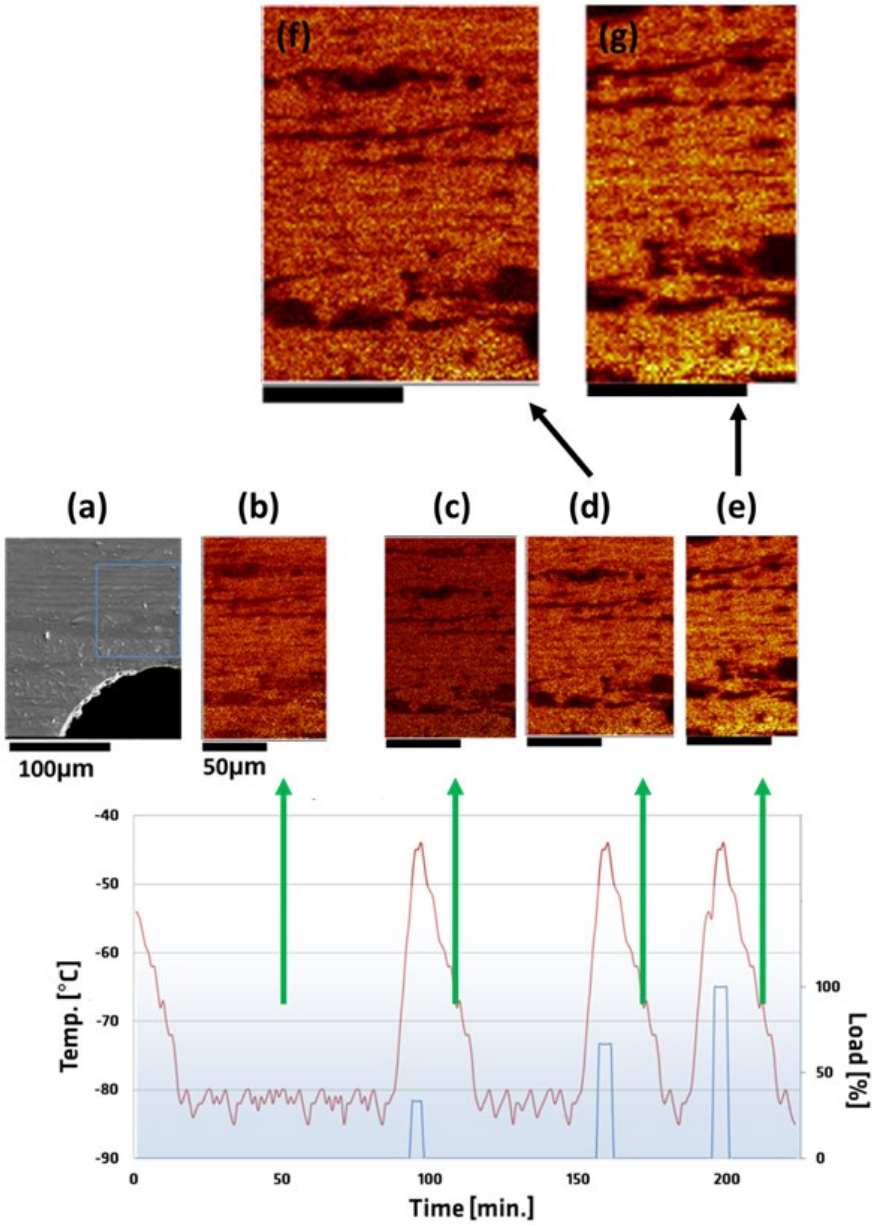

Figure 5-19: (a) SEM image of the area of interest, the region imaged by ToF-SIMS is marked by a blue square. (b) – (e) PC1 scores image obtained from the negative SIMS data related to locations rich in deuterium before applying load (b) and after applying different loads: low (c), medium (d) and high (e). Figures (d) and (e) are enlarged in Figures (f) and (g), respectively. The blue line refers to the load and the red line to the sample temperature. The black line in figures c-g represents 50µm.

The sample used in the first experiment had a thickness of 630µm whereas the second sample had a thickness of 450µm. It is anticipated that the multiple warm-ups, allowed sufficient time for more deuterium to reach regions of high stresses.

Additionally, the different thickness of the second sample resulted in higher stress and a larger deformation close to the notch. Therefore, it is assumed that some of the cracks in the region close to the notch were formed during applying the load.

The spatial resolution of the ToF-SIMS in the second experiment (BA in the SIMS instrument) did not allow to observe the formation of the cracks, however the in-homogeneities obtained close to the notch (<20µm from the notch) and within the γ layer (Figure 5-18) suggest that the combination of higher load with higher concentration of deuterium lead to the formation and propagation of cracks.[213] This assumption can be supported by macro-scale four-point bending test experiments conducted by Lofrano et al. [210]. In these experiments it was shown that under a specific strain regime, hydrogen assisted cracking takes place at tip of the notch by the formation of microcracks.

The goal of the present work was to make stress induced distribution of deuterium under mechanical load visible. Further investigations and future developments of this experiment are suggested in the perspectives.

6 Conclusions

This work enabled showing the desired unique correlation between hydrogen concentration and the resulting degradation in a two phase microstructure. The research generated key experimental evidence for some of the theories that up to the present have never been proven on this scale. To enable direct comparison, these testing methods were applied to both standard 22%Cr 5%Ni and lean 21%Cr 1%Ni DSSs. Due to the path of the research, the experimental and metallurgical conclusions are interlinked and described in the following bullets:

1. ToF-SIMS imaging together with appropriate data treatment emerged as a strong tool for understanding the interaction of hydrogen and deuterium with a dual phase metal microstructure.
2. The novel procedure of fusing the data delivered by topographic and ToF SIMS chemical imaging represents a more suitable tool for investigating deuterium and hydrogen interactions with a dual phase microstructure.
3. The temperature controlled device for the respective deuterium analyses represents a meaningful tool to account for controlled releasing of deuterium from austenite and ferrite.
4. Under UHV conditions, with no mechanical load applied to the microstructure, an activation of deuterium in the standard DSS microstructure was found to be dependent on temperature. At temperatures below ca. -60 °C, most of the charged deuterium is stable in the austenite. Above -60 °C it is increasingly activated and starts to diffuse into the ferrite.
5. The ferrite acts as a faster diffusion path due to the higher diffusivity as compared to austenite. Deuterium then might be trapped at the austenite-ferrite interface. The blistering in the ferrite can be explained by the recombination of the trapped deuterium at the interface (ex-situ analyses), notwithstanding the uptake of deuterium at the surface of the blisters due to the deformation of the ferrite underneath.
6. When the analyzed surface is not damaged due to the exposure to the electrolyte, ferrite is acting as a fast diffusion path in the rolling direction (in-situ permeation analyses) whereas the austenite acts as a barrier for deuterium.
7. Significant cracking of the austenitic phase can be explained by extensive twinning and martensitic phase transformation that was followed by high deuterium concentrations around cracks at the surface. These are attributed to the local

stresses in the lattice by the diffusion of deuterium. As further evidence, cracking at the interface between austenite and ferrite has been observed. As has been shown elsewhere[123, 200] these might be attributed to high stresses induced, in this case, by charging and distortion of the surface of the phases from both sides of the interface. These findings help to explain better the brittle failure of the austenitic phase.

8. The high chemical sensitivity of ToF-SIMS in combination with applying in-situ and ex-situ experiments enabled characterization of the nature of carbon and nitrogen at the surface, with and without exposure to the electrolyte. The high solubility of these elements in the austenite can be used as a tool to distinguish between the phases in a DSS microstructure. Up to the present, the distinction of the phases was conducted in the positive mode[72, 167, 192] whereas the CN signal is extracted in the negative mode together with the deuterium related signals and thus simplifies the acquisition and process.
9. The in-situ permeation experiment showed that locally increased concentration of the CN signal in the ferrite correlates with a higher deuterium signal in the ferrite. This might be attributed to the affinity of deuterium to nitrogen.
10. In the ex-situ experiments, the exposure of the analyzed surface to the electrolyte is expressed by a drastic reduction of the CN signal. It is anticipated that the electrolyte interacts mainly with the nitrogen to form ammonium ions in the solution.[30, 214]
11. The ex-situ post charging and in-situ permeation ToF-SIMS imaging experiments were compared. The ex-situ static experiments have indicated enrichment of the austenitic phase whereas the in-situ permeation experiment indicated enrichment of the ferritic phase. Yet, both types of experiments are proving the same point; one from the higher solubility of deuterium in the austenite point-of-view and from the higher diffusion rate of deuterium in the ferrite point-of-view.
12. The relationship between hydrogen distribution in complex microstructures and the resulting structural and microstructural changes were shown locally in the lean DSS for the first time. The degradation processes of the lean DSS are generally similar to those occurring in the standard DSS. However, the instability of the austenite was indicated by the extensive transformation of the FCC phase into mainly BCC and HCP brittle phases, unlike the standard DSS where mainly FCC-HCP transformation was obtained. It is anticipated that the susceptibility of the austenitic phase to hydrogen ductile-to-brittle transformation degradation

mechanism is directly related to the nickel content in this phase, excluding mechanical loading experiments.

13. ToF-SIMS in-situ mechanical loading experiments on standard DSS were proven to locally show strain induced diffusion of deuterium. The mechanical load must be applied above -50°C to ensure mainly ductile behavior of both phases above the DBTT of the steel[186, 215]. It is concluded that iteration of the loading process on the sample allows more deuterium to diffuse into regions of high strains (in front of the notch) and therefore induces a larger degradation of the microstructure.
14. Permeation and mechanical load must be examined in a similar way to the service conditions. However, the characterization of the damage to the phases can be examined in all directions. Therefore, the ex-situ static experiments were conducted normally to the rolling direction, allowing better observation of the formation of blisters in the ferrite as part of the degradation process.

7 Perspectives

Clearly the use of ToF-SIMS, SEM and EBSD observations help to improve the understanding of hydrogen induced degradation of DSSs when exposed to acidic environments. The present work entails some perspectives towards a better understanding of hydrogen transport and cracking of metallic materials. The main directions are outlined in the following:

1. The significant role of phase boundaries in the diffusion process has been shown extensively in this work. Thus it should be considered to adapt the approach of ex-situ static characterization and in-situ mechanical loading also to a single phase grade for the qualitative comparison. According to the composition determination measurements conducted by Straub et al. [169] the austenitic and/or ferritic grade can be selected and compared. Such work could show the different influence of deuterium on grain boundaries.
2. The selection of a comparable austenitic grade can also be based on evaluating the susceptibility of the austenite to hydrogen assisted ductile-to-brittle transformation degradation. In this way it will be possible to obtain a better understanding of the role of the alloying elements (especially Ni) in the hydrogen assisted degradation mechanisms. In addition, the transformation sequence can be locally studied and correlated to the hydrogen concentrations by analyzing shorter charging times, as was initiated in this work. It is suggested to combine the analyses with FIB milling of charged samples in order to confirm whether the HCP phase exists between the surface BCC phase and the bulk phases.
3. Since the research was conducted by deuterium charging, global quantification methods must be adjusted to allow deuterium quantification. In this way it will be possible to correlate the global amount of deuterium and the local observations on the deuterium distribution and resulting damage in the material. Also as part of this future task, the role of $NaAsO_2$ used as a recombination poison must be further studied.
4. The in-situ mechanical loading experiments have shown stress induced local enrichments above the notch. The next step should be the initiation and propagation of a crack under these conditions. For this purpose the sample should be thinned in a way that allows crack initiation. In addition, EBSD measurements must be applied to trace the local phase transformations in the highly stressed region after the mechanical load has been applied with and without charging with deuterium.

5. The combination of several methods has been shown here to contribute to a better understanding of hydrogen assisted degradation phenomena. This approach should be adapted to investigate pitting corrosion processes. The ToF-SIMS can be useful for tracing the hydrogen in the pits to obtain better understanding of the mechanisms related to crack initiation.
6. The combination of mechanical load with the ability to image the hydrogen distribution in the ToF-SIMS can be adapted to investigate the effect of a fatigue load on deuterium charged specimen in different materials (e.g. martensitic steels).
7. The combination of ToF-SIMS, HR-SEM, EBSD and FIB can be adapted to investigate hydrogen assisted degradation mechanisms in other materials (e.g. Ni based alloys) and in other microstructures and microstructural features (e.g. carbide precipitation in SMSS). This approach can also be incorporated with other testing methods such as slow strain rate testing (SSRT) and fatigue crack testing.

8 Abbreviations

AES – Auger electron spectroscopy

BA – Burst alignment

BCC – Body centered cubic

BCT – Body centered tetragonal

BSE – Backscattered electon

CBA – Collimated burst alignment

DBTT – Ductile – brittle transition temperature

DSC – Dual source column

DSS – Duplex stainless steel

EBSD – Electron back-scattered diffraction

ED – Electron diffraction

EDM – Electric discharged machining

EDX – Energy dispersive x-ray spectroscopy

FCC – Face centered cubic

FIB – Focused ion beam

HAC – Hydrogen assisted degradation

HCBU – High current burst alignment

HCP – Hexagonal close packed

HE – Hydrogen embrittlement

HEDE – Hydrogen enhanced localized plasticity

HELP – Hydrogen enhanced decohasion

HR-SEM – High resolution scanning electron microscope

LDX – Lean duplex

LMIG – Liquid metal ion gun

LDX – Lead duplex stainless steel

MVA – Multivariate data analysis

MS – Mass spectrometry

OM – Optical microscope

OES – Optical emission spectroscopy

PC – Principal component

PCA – Principal component analysis

RT – Room temperature

SDSS – Super duplex stainless steel

SE – Secondary electron

SI – Secondary ion

SSRT – Slow strain rate testing

TDS – Thermal desorption spectroscopy

TEM – Transmission electron microscope

ToF-SIMS – Time-of-Flight secondary ion mass spectrometer

UHV – Ultra high vacuum

XRD – X-ray diffraction

XPS – X-ray photoelectron spectroscopy

9 List of figures

Figure 1-1: Example of a failure in a hub with welded pipe connectors from the BP Amoco Foinaven Field.[7] The component, made of a 2507 DSS, failed during service on the hub side close to the weld (marked with a red circle). The failure was a result of stress concentration in the connection between the hub and the pipe. The microstructure of coarse elongated grains oriented through the wall thickness enabled easy access of hydrogen. 2
Figure 2-1: Standard 2205 duplex stainless steel continuous sulphate pulp digester and impregnation tower in Sodra Cell Mönsteras, Sweden. 5
Figure 2-2: The four classifications of dual-phase microstructures.[13] 9
Figure 2-3: WRC – 1992 diagram. The ferrite number (FN) prediction is only accurate for (weld) compositions that fall within the bounds of the iso-FN lines (0-100)that are drawn on the diagram. The limits of the diagram were determined by the extent of the database.[17, 18] 10
Figure 2-4: a) the formation of different phases during the solidification of the DSS alloy melt as a function of temperature and b) the Quasi-binary section through the Fe–Cr–Ni diagram at 70 wt.-% Fe.[13, 20] 12
Figure 2-5: Microstructural comparison of a) ferritic, b) austenitic, and c) ferritic–austenitic DSSs. The DSS has its unique 'sandwich' microstructure. Etchant: aqua regia/V2Apickle (ferrite, austenite) and Beraha II reagent (duplex)[13]. 13
Figure 2-6: A 3D sectioning of typical DSS after thermo-mechanical treatment. The 'sandwich' microstructure is obtained parallel and normal to the rolling direction.[20, 24] 14
Figure 2-7: Cracked oilfield tubular (Marathon Oil UK Ltd.)[11] 20
Figure 2-8: Example of (a) fill microstructure, (b) cap microstructure and (c) crack path in offshore production pipework (Exxon Production Research Company, Houston)[11] 21
Figure 2-9: The tetrahedral (T) and octahedral (O) interstitial sites in BCC lattice (top) and in FCC lattice (bottom).[60, 61] 23
Figure 2-10: The relationship between membrane thickness and actual permeation path in a 25 wt.-% *Cr DSS.[57]* 27
Figure 2-11: Various potential traps in a steel microstructure: a) dissolved in the microstructure, b) adsorbed and (c) absorbed at the surface, d) trapped in grain and\or phase boundaries, e) in stressed/strained regions (such as dislocations), f) in vacancies.[82] 29
Figure 2-12: The energy level of hydrogen around trap sites[83] 30
Figure 2-13: Influencing factors in hydrogen assisted degradation and cracking of steels. The main knowledge gaps are described as well. 31
Figure 2-14: A schematic illustration of the AIDE mechanism involves alternate-slip from crack tips facilitating coalescence of cracks with voids formed in the plastic zone ahead of cracks.[105, 115] 35
Figure 2-15: A schematic diagrams illustrating the hydrogen enhanced localized plasticity mechanism – HELP (a) and the hydrogen enhanced decohasion mechanism – HEDE (b) where the weakening interatomic bonds takes place

by (i) hydrogen in the lattice, (ii) adsorbed hydrogen, (iii) hydrogen at the precipitate-matrix interface.[70] 36
Figure 2-16: SEM images of blister in different location in a high purity iron in (a) low and (b) high magnification. (c) Cross-section of the sample showing the morphologies of internal cracks where the hydrogen was accumulating. The surface of the sample is marked by arrows. 1) Crack underneath blister showing curving of crack towards the free surface. 2) Zig-zag crack morphology. 3) Triple-point crack morphology. (d) Close-up view of a cross-section of a blister and the underlying crack.[120] 37
Figure 2-17: Schematic diagram illustrating the formation and fracture of brittle hydride at the crack tip.[70] 39
Figure 2-18: ToF-SIMS images of a) deuterium and b) hydrogen distribution at the surface of an electrochemically deuterated DSS 2205 sample and c) OM image of the same ROI (A and F stand for austenitic and ferritic grains respectively).[128] 41
Figure 2-19: Diffusivity of Isotopes in different temperature in a) bcc metals and b) FCC metals.[54] 43
Figure 2-20: Diffusivity of Isotopes in high purity Fe (open squares: H, filled squares: D)[137] 43
Figure 2-21: Dimensions of one representative tested cantilever in the In situ electrochemical microcantilever bending test[145] 46
Figure 2-22: Representative SEM images of the H free (a) and H charged (b) cantilevers bent to a displacement of maximum 5µm. SEM images of cross sections of the marked areas in (a) and (b) are shown respectively in (c) and (d). [145] 47
Figure 2-23: Barnoush in-situ experiments on AFM images form the surface of the sample during in situ electrochemical H-charging. Before H charging (a), after 1 h (b), 2.5 h (c) and higher magnification image from the surface of the austenite grain (d). On the left is a ferrite grain and on the right is an austenite grain which can be distinguished by its convex grain boundary.[146] 48
Figure 2-24: Takahashi APT experiments – 3D elemental maps of the peak-aged steel sample with deuterium charging revealing the deuterium distribution at a VC precipitate.[152] 51
Figure 2-25: Inclined view on the reconstructed 3-D model of a hydrogen-charged iron sample, the raw data is produced by neutron tomography. The surface with blisters is shown in (a). The crack distribution in the interior is presented in (b) and the additional hydrogen distribution in (c).[119] 52
Figure 2-26: Three orthogonal slices taken from arbitrarily positions in the reconstructed 3-D model: (a) xy-plane, (b) yz-plane, (c) xz-plane. The data is produced by neutron tomography.[119] 52
Figure 2-27: Collision cascade in a solid sample covered by a monolayer initiated by the impact of an energetic primary ion (red).[157] 53
Figure 2-28: The principle of the Time-of-Flight detector allowing mass dispersion in a drift path where $m_1 < m_2 < m_3 < m_4$.[158] 55
Figure 2-29: Oltra's experiments with imaging dynamic SIMS: The image (left) and the schematic overview (right) show the high concentration of deuterium in the

austenitic grains in a DSS after strain tests in deuterated environments (gaseous and aqueous).[167] 56
Figure 3-1: Survey on the existing and the new approach to build and test models on hydrogen behavior in steels 63
Figure 4-1: Directions in which the observations, for each type of steel and experiment, were conducted (figure was taken from ref.[13]). Ex-situ experiments were conducted at the normal direction (ND) for the DSS2205 and in the transverse direction (TD) for the LDX2101. In-situ permeation and in-situ mechanical loading experiments were conducted in the rolling direction (RD). 66
Figure 4-2: Overview of the liquid metal ion gun column in the ToF-SIMS instrument of IONTOF © (Muenster, Germany). 67
Figure 4-3: a) Overview of the liquid metal ion gun column in the ToF-SIMS instrument of IONTOF © (Muenster, Germany) and b) Primary ion gun scheme of the beam guidance for the BA and CBA modes used for imaging on an ION-TOF instrument.[161, 162] 70
Figure 4-4: Relative secondary negative Ion yield (M-) from Cs+ bombardment vs. atomic number of secondary ion. [181] 72
Figure 4-5: Relative secondary positive ion yield (M+) due to O- bombardment vs. atomic number of secondary ion.[181] 73
Figure 4-6: Description of the sample holder for ex-situ mechanically non-loaded experiments (IONTOF ©, Muenster, Germany). 75
Figure 4-7: Geometry and dimensions of the sample for ex-situ mechanically non-loaded experiments. 76
Figure 4-8: Schematic illustration of the Piezo actuator, a) The stack type architecture, b) Preloading technique and c) The PA/T design.[183] 77
Figure 4-9: Geometry and dimensions of the sample holder for in-situ four-point bending experiments. The sample is indicated by a red arrow. 78
Figure 4-10: Geometry and dimensions of the sample for the in-situ mechanical loading experiments and an illustration of stress concentration ahead of the notch. 80
Figure 4-11: Schematic view of the real time and in-situ deuterium permeation experiment within the ultra-high vacuum chamber of the ToF-SIMS instrument. 81
Figure 4-12: SE images taken by a) In-lens detector and b) Regular SE detector of a standard 2205 DSS after electrochemical charging. 82
Figure 4-13: Schematic illustration of the experimental setup for EBSD measurements.[185] 83
Figure 4-14: Example secondary ion image made during a FIB cut in a standard 2205 DSS after electrochemical charging. The image was made by the secondary ion signal and therefore shows the grain pattern. 85
Figure 4-15: Schematic illustration of the electrochemical charging process of the samples for ex-situ static and in-situ mechanical loading analyses. 87
Figure 4-16: Course of the in-situ mechanical loading experiments. a) Applying the maximal load by changing the potential applied on the actuators from -20V to 130V in one step and b) Applying the load stepwise by changing the potential

applied on the actuators from -20V to 130V in three steps. Imaging by ToF-SIMS took place when the sample temperature was below -75°C. All images were taken with the same parameters (acquisition time and primary ion current). The blue line refers to the load and the red line to the sample temperature. 91
Figure 4-17: Displacement-voltage diagram of a piezoelectric actuator delivered by PiezoJena. 92
Figure 4-18: The basic concept for data pre-processing and PCA of image data. 96
Figure 4-19: Example of PCA data treatment of the raw data acquired in the in-situ permeation experiment. Only the normalized D- signal images taken after 28 (a), 34 (b) and 37 (c) and the PCA enhanced loading plots (d-f) of PC1 of the images shown in a-c. 97
Figure 4-20: The basic concept of ImageLab for data processing and data fusion.[191] 99
Figure 4-21: Example of data fusion of a HR-SEM image and normalized raw image data of a) deuterium and b) hydrogen SIMS by ImageLab©. The hydrogen is distributed rather homogeneously on the surface of the analyzed sample and is attributed to the adsorbed hydrogen species from the rest gas in the analysis chamber. The increased intensities appearing around cracks are assumed to occur due to the absorption of hydrogen during the time the sample was exposed to air while transferred from the charging cell to the analysis chamber. The deuterium shows higher and more homogeneously distributed intensities in the austenite than in the ferrite. The phase mapping is shown in Figure 4-21a, where γ and δ stand for austenite and ferrite, respectively. 100
Figure 5-1: PC1 loading plots taken from the same area during sample warm-up of a DSS sample charged for 72 hours: a) -120°C – -60°C, b) -58°C – -30°C, c) -29°C – -4°C. PC1 is representative for deuterium in the microstructure. 101
Figure 5-2: Fusion of a SEM topographic image and a SIMS PC1 loadings plot representing deuterium in the microstructure (colored). The image reveals needle shaped microtwins in the ferritic phase which are oriented along the grains. The concentration of deuterium is higher in the microtwins as in the ferrite phase surrounding it. The highest concentration of deuterium is concluded around the cracks. SIMS image data was acquired after 96 hours of electrochemical charging. 103
Figure 5-3: Total SI image of a FIB cross section normal to a micro-crack observed on the surface of the charged DSS sample. The FIB cut was taken from a different area on the sample than the one displayed in Figure 5-2. The FIB cut position is shown in the inset. A separation along the interface between the phases is clearly visible. The inner pressure in the blister caused the formation of secondary cracks in the ferrite. The deposited Pt layer is necessary for FIB and the phase characterization was done by EDS. 104
Figure 5-4: Michalska polarization test of a 2205 DSS in 3.5% NaCl solution: formation of blisters in the ferritic phase (marked by red ellipses) after charging the material for 7 days with a current density of 10mA cm^{-2}. 105

Figure 5-5: Fusion of a SEM topographic image and a SIMS PC1 loadings plot representing deuterium in the microstructure (colored). The highest deuterium concentration was observed around some of the parallel cracks and more significantly around larger cracks marked by a black dashed ellipse in a) and around cracks at the phase boundaries (marked by a white dashed ellipse in a). Regions 1-3 in b) are discussed in text and are indicating on three levels of deuterium concentration in the austenite in cracked and non-cracked areas. 107
Figure 5-6: SE topographic and EBSD phase maps of the sample before (a and c) and after (b and d) charging with deuterium. The area shown in a and c is marked by a white rectangle in b and d. The changes of the surface are caused by charging. 108
Figure 5-7: Fusion of HR-SEM topographic image with colored ToF-SIMS PCA plots of deuterium in the microstructure. The insets show the local differences in the charging effect and the deuterium concentration in the ferrite (a), ferrite-austenite interface (b), and austenite (c). 109
Figure 5-8: Fusion of SEM topographic image data and PC1 loadings plots obtained by principal component analysis (PCA) of ToF-SIMS image data representing deuterium in the microstructure (colored). The images show the local differences in the deuterium concentration in the austenite (b) and in the ferrite (c). 110
Figure 5-9: Pattern quality (a and c) and phase map (b and d) of the LDX 2101 before and after 72 hours of charging the specimen with deuterium. The red and green colors in the phase map indicate the BCC structure and FCC structure, respectively. 111
Figure 5-10: a) Data fusion of a SEM topographic image and a SIMS PC1 loadings image plot representing the deuterium distribution in the LDX 2101 after 72 hours of charging (deuterium concentration indicated by the warmer colors) and b) an overlay of the EBSD phase map (red: BCC, green: FCC) on the pattern quality image. The ToF-SIMS image was taken from an area of 100x100µm. The dashed gray lines indicate these parts of the images which can be compared one by one. The white circle and rectangle indicate regions with lower concentration of deuterium and where less austenite had been transformed into BCC martensite. 112
Figure 5-11: Overlay of the EBSD phase map (red: BCC, green: FCC, yellow: HCP) and the pattern quality image. The transformation of FCC into HCP and BCC was obtained in defect rich regions, the former ferrite was less affected by charging, except for the formation of blisters in this phase. 114
Figure 5-12: a) Data fusion of a SEM topographic image and a SIMS PC1 loading plot representing deuterium in the microstructure of a LDX 2101 after 72 hours of charging and b) phase map of the same region. The ToF-SIMS image was taken from an area of 50x50µm. The dashed gray lines indicate these parts of the images which can be compared one by one. 115
Figure 5-13: Fusion of HR-SEM imaging with colored ToF-SIMS PCA plots of deuterium in a LDX microstructure, a) Magnification of the ferritic phase showing blistering and respective cracking to a smaller extent than in DSS

2205, b) Magnification of small cracks in the austenite phase that differ from the parallel orientation observed for the DSS 2205 116
Figure 5-14: a) Principle component score images of the ToF-SIMS data sets acquired after 34 days of charging. (a) PC1 scores image for identifying phases using the positive ToF-SIMS data set acquired after 34 days of charging DSS with deuterium by using a peak list with secondary ions covering the main alloying elements. The bright regions represent the austenite phase (as proved by the loadings plot in shown Figure 5-15a. (b) PC1 scores image identifying locations rich in deuterium obtained from the negative SIMS data set acquired after 34 days and using the full peak list. Bright pixels indicate positive scores and correlate with the ferrite phase. (c) PC1 scores image obtained from the same data set but using a different peak list prepared to focus on carbides and nitrides. This image is identifying locations rich in N and C. Bright pixels indicate positive scores and correlate with the austenite phase. (d) PC2 scores image identifying locations rich in N, C and D (bright pixel means positive score) indicating graded accumulation of deuterium at the ferrite and austenite grain boundaries and at the ferrite/austenite interface (highest scores!) as well. 120
Figure 5-15: Principle component loading plots from PCA corresponding a) to the scores in Fig 5-14a and 5-16a; b) to the scores in Fig 5-14b and 5-16b; c) to the scores in Fig 5-14c; d) to the scores in Fig 5-14d. For the interpretation of the peaks the reader is referred to Table 12. 121
Figure 5-16: (a) PC1 scores image obtained from the positive SIMS data set acquired after 37 days of charging DSS and used to identify phases in the DSS micro structure. A fresh region of interest (ROI) has been selected. The bright regions represent the austenite phase (as shown in the loading plot in Figure 5-15a). (b) PC1 scores image related to locations rich in deuterium. The image was generated by PCA of a negative ToF-SIMS image data set obtained after loading with deuterium for 37 days. The bright deuterium-rich areas have positive scores and correspond to the ferrite phase while the dark areas have negative scores and relate to austenite grains. (c) Ion induced secondary electron (SE) image of displaying grains in the DSS microstructure at the selected region of interest. (d) Mente et al. [9] numerical simulations of hydrogen distribution in a DSS 2205 microstructure showing that an interconnected ferrite phase is acting as fast permeation track by a 2-D modelling of the diffusion of hydrogen in a DSS microstructure. Figures a-c are taken from the same area of 100x100 µm^2. 123
Figure 5-17: Fusion of a SEM topographic image and a SIMS PC1 scores plot representing deuterium in the microstructure (colored) of a standard 2205 DSS (a) before applying any mechanical load and (b) after applying a maximal load by the actuators. The brighter regions represent the austenite. The SEM image was taken after the SIMS analyses. 127
Figure 5-18: SE image of the second sample after ToF-SIMS in-situ mechanical loading experiments. 128
Figure 5-19: (a) SEM image of the area of interest, the region imaged by ToF-SIMS is marked by a blue square. (b) – (e) PC1 scores image obtained from

the negative SIMS data related to locations rich in deuterium before applying load (b) and after applying different loads: low (c), medium (d) and high (e). Figures (d) and (e) are enlarged in Figures (f) and (g), respectively. The blue line refers to the load and the red line to the sample temperature. The black line in figures c-g represents 50μm. 129

10 List of tables

Table 1: Basic composition in wt.-% and mechanical properties of three types of stainless steels 14
Table 2: Typical ranges of alloying elements of the different grades in the DSS given in wt.-%.[11, 12, 27] 17
Table 3: Physical properties of hydrogen isotopes[54] 40
Table 4: Summary of direct methods for hydrogen mapping[82] 50
Table 5: Summary of SIMS analyses for investigations of hydrogen enhanced degradation 57
Table 6: Nomenclature and nominal chemical composition of the tested DSSs (wt.-%).[27] 65
Table 7: Chemical composition of the tested DSSs (wt.-%) measured by optical emission spectroscopy (OES).[177-179] 65
Table 8: The achievable spatial and mass resolutions and the typical voltages applied on the different lenses for the HCBU, BA and CBA.[161] 69
Table 9: Components used in conventional and current permeation and charging experiments in the ToF-SIMS 87
Table 10: Summary of the different processes in the ToF-SIMS before deuterium charging or after the warm-up of the sample. 89
Table 11: Summary of the different processes in the ToF-SIMS in the time frame where the sample contains deuterium. 89
Table 12: The delivered peak list (m/z ratio) acquired in the HCBU and the interpretation of the mases 94

11 References

1. Johnson, W.H., *On some remarkable changes produced in iron and steel by the action of hydrogen and acids.* Proceedings of the Royal Society of London, 1874. **23**(156-163): p. 168-179.
2. Furtado, J. and F. Barbier. *Hydrogen Embrittlement-Related Issues and Needs in the Hydrogen Value Chain*. in *International Hydrogen Conference (IHC 2012)*. 2012. Grand Teton National Park, Jackson Lake Lodge, Wyoming, USA: ASME press.
3. Lo, K.H., C.H. Shek, and J.K.L. Lai, *Recent developments in stainless steels.* Materials Science & Engineering R-Reports, 2009. **65**(4-6): p. 39-104.
4. Oriani, R.A., *Hydrogen Embrittlement of Steels.* Annual Review of Materials Science, 1978. **8**: p. 327-357.
5. Barnoush, A. and H. Vehoff, *Recent developments in the study of hydrogen embrittlement: Hydrogen effect on dislocation nucleation.* Acta Materialia, 2010. **58**(16): p. 5274-5285.
6. Robertson, I.M., et al., *Hydrogen Embrittlement Understood.* Metallurgical and Materials Transactions a-Physical Metallurgy and Materials Science, 2015. **46A**(6): p. 2323-2341.
7. Taylor, T.S., T. Pendlington, and R. Bird. *Foinaven super duplex materials cracking investigation*. in *Offshore Technology Conference*. 1999. Houston, Texas: Offshore Technology Conference.
8. Mente, T. and T. Boellinghaus, *Mesoscale modeling of hydrogen-assisted cracking in duplex stainless steels.* Welding in the World, 2014. **58**(2): p. 205-216.
9. Mente, T. and T. Boellinghaus, *Modeling of Hydrogen Distribution in a Duplex Stainless Steel.* Welding in the World, 2012. **56**(11-12): p. 66-78.
10. *ASM Metals HandBook Volume 1 - Properties and Selection Irons Steels and High Performance Alloys*. ASM Metals Handbook - Desk Edition, ed. **J.R. Davis**. Vol. 1. 1990: ASM International.
11. Gunn, R.N., *Duplex Stainless Steel: Microstructure, properties and applications*. 1997: Elsevier.
12. Alvares-Armas, I., *Duplex Stainless Steels: Brief History and Some Recent Alloys.* Recent Patents on Mechanical Engineering, 2008. **1**: p. 51-57.
13. Knyazeva, M. and M. Pohl, *Duplex Steels: Part I: Genesis, Formation, Structure.* Metallography, Microstructure, and Analysis 2, 2013. **2**: p. 113-121.
14. Ogawa, T. and T. Koseki, *Weldability of Newly Developed Austenitic Alloys for Cryogenic Service: Part 1 — Up-to-date Overview of Welding Technology.* Welding Research, 1987. **67**(1): p. 332-341.

15. Hammar, O. and U. Svensson. *Influence of steel composition on segregation and microstructure during solidification of austenitic stainless steels*. in *Solidification and Casting of Metals*. 1977. Sheffield, England: The Metal Society, London.
16. DeLong, W.T. *Ferrite in austenitic stainless steel weld metal*. in *55. AWS Annual Meeting*. 1974. Houston, Texas: Weld. J.
17. Lippold, J.C. and D.J. Kotecki, *Welding metallurgy and weldability of stainless steels*. 2005, USA: Wiley-Interscience.
18. Kotecki, D.J. and T.A. Siewert, *WRC-1992 constitution diagram for stainless steel weld metals: a modification of the WRC-1988 diagram.* Welding Journal, 1992. **71**(5): p. 171-178.
19. Ogawa, T., T. Koseki, and H. Inoue, *Weld Phase Chemistries of Duplex Stainless Steels.* Weldability of Materials, 1990.
20. Nilsson, J.O. and G. Chai, *The physical metallurgy of duplex stainless steels*. 1992, Sandvik Materials Technology: Sandvik Materials Technology, R&D Centre, S-81181 Sandviken, Sweden.
21. Berns, H. and W. Theisen, *Ferrous materials: steel and cast iron*. 2008, Berlin: Springer Science & Business Media.
22. *ASM Metals HandBook Volume 4 - Heat Treating*. ASM Metals Handbook - Desk Edition, ed. **J.R. Davis**. 1991: ASM International.
23. Pohl, M., O. Storz, and T. Glogowski, *Effect of intermetallic precipitations on the properties of duplex stainless steel.* Materials Characterization, 2007. **58**(1): p. 65-71.
24. ElYazgi, A.A. and D. Hardie, *The embrittlement of a duplex stainless steel by hydrogen in a variety of environments.* Corrosion Science, 1996. **38**(5): p. 735-744.
25. Olsson, C.O.A. and D. Landolt, *Passive films on stainless steels - chemistry, structure and growth.* Electrochimica Acta, 2003. **48**(9): p. 1093-1104.
26. Nagano, H., et al., *Highly Corrosion Resistant Duplex Stainless Steel.* Metaux-Corrosion-Industrie, 1981. **56**(667): p. 81-88.
27. TMR Stainless, P., PA, USA, *Practical Guidelines for the Fabrication of Duplex Stainless Steels*, in *IMOA - International Molybdenum Association*, I.-I.M. Association, Editor. 2014, IMOA: London, UK.
28. Miura, M., et al., *The effects of nickel and nitrogen on the microstructure and corrosion resistance of duplex stainless steel weldments.* Welding International, 1990. **4**(3): p. 200-206.
29. Vehovar, L., et al., *Investigations into the stress corrosion cracking of stainless steel alloyed with nitrogen.* Materials and Corrosion-Werkstoffe Und Korrosion, 2002. **53**(5): p. 316-327.
30. Grabke, H.J., *The role of nitrogen in the corrosion of iron and steels.* Isij International, 1996. **36**(7): p. 777-786.

31. Sedriks, A.J., *Role of sulphide inclusions in pitting and crevice corrosion of stainless steels.* International metals reviews, 1983. **28**(1): p. 295-307.
32. Westin, E.M., *Microstructure and properties of welds in the lean duplex stainless steel LDX 2101®*, in *Department of Materials Science and Engineering*. 2010, Royal Institute of Technology Stockholm, Sweeden.
33. Kim, Y.H., K.Y. Kim, and Y.D. Lee, *Nitrogen-alloyed, Metastable Austenitic Stainless Steel for Automotive Structural Applications.* Materials and Manufacturing Processes, 2004. **19**(1): p. 51-59.
34. Narita, N., C.J. Altstetter, and H.K. Birnbaum, *Hydrogen-Related Phase-Transformations in Austenitic Stainless-Steels.* Metallurgical Transactions a-Physical Metallurgy and Materials Science, 1982. **13**(8): p. 1355-1365.
35. Rozenak, P. and D. Eliezer, *Nature of the Gamma-Phase and Gamma-Star-Phase in Austenitic Stainless-Steels Cathodically Charged with Hydrogen.* Metallurgical Transactions a-Physical Metallurgy and Materials Science, 1988. **19**(3): p. 723-730.
36. Kruml, T., J. Polak, and S. Degallaix, *Microstructure in 316LN stainless steel fatigued at low temperature.* Materials Science and Engineering a-Structural Materials Properties Microstructure and Processing, 2000. **293**(1-2): p. 275-280.
37. Das, A., et al., *Morphologies and Characteristics of Deformation Induced Martensite During Tensile Deformation of 304LN Stainless Steel.* Materials Science and Engineering A, 2008. **486**(1-2): p. 283-286.
38. Humbert, M., et al., *Analysis of the γ-ε-α' Variant Selection Induced by 10%Plastic Deformation in 304 Stainless Steel at -60.* Materials Science and Engineering A, 2007. **454-455**: p. 508-517.
39. Hedstrom, P., et al., *Stepwise transformation behavior of the strain-induced martensitic transformation in metastable stainless steel.* Scripta Materialia 56 (2007) 213., 2007. **56**(3): p. 213-216.
40. Spencer, K., et al., *The strain induced martensite transformation in austenitic stainless steels: part-1 Influence of temperature and strain history.* Materials Science and Technology, 2009. **25**(1): p. 7-17.
41. Choi, J.-Y. and W. Jin, *Strain induced martensite formation and its effect on strain hardening behavior in the cold drawn 304 austenitic stainless steel.* Scripta Materialia, 1997. **36**(1): p. 99-104.
42. Murr, L.E., K.P. Staudhammer, and S.S. Hecker, *Effects of strain state and strain rate on deformation-induced transformation in 304 stainless steel: Part II. Microstructural study.* Metallurgical Transactions A 1982. **13**(4): p. 627-635.
43. Varma, S.K., et al., *Effect of grain size on deformation-induced martensite formation in 304 and 316 stainless steels during room temperature*

tensile testing. Journal of Materials Science Letters, 1994. **13**(2): p. 107-111.
44. Kireeva, I.V. and Y.I. Chumlyakov, *The orientation dependence of γ-α' martensitic transformation in austenitic stainless steel single crystals with low stacking fault energy* Materials Science and Engineering A, 2008. **481-482**: p. 737-741.
45. Raman, S.G.S. and K.A. Padmanabhan, *Tensile deformation-induced martensitic transformation in AISI 304LN austenitic stainless steel.* Journal of Materials Science Letters, 1994. **13**(5): p. 389-392.
46. Mirzadeh, H. and A. Najafizadeh, *Correlation between processing parameters and strain-induced martensitic transformation in cold worked AISI 301 stainless steel.* Materials Characterisation, 2008. **59**(11): p. 1650-1654.
47. Fukuda, T., T. Kakeshita, and K. Kindo, *Magneto-mechanical evaluation for twinning plane movement driven by magnetic field in ferromagnetic shape memory alloys.* Materials Science and Engineering A, 2006. **438**: p. 12-17.
48. Charles, J. *10 Years Later, Obviously Duplex Grades in Industrial Applications Look Like a Success Story*. in *Proc. of 6th World Duplex Conf. & Expo.* 2000. Venice, Italy: AIM.
49. Zucchi, F., et al., *Hydrogen embrittlement of duplex stainless steel under cathodic protection in acidic artificial sea water in the presence of sulphide ions.* Corrosion Science, 2006. **48**(2): p. 522-530.
50. Francis, R. *Conf. Proc. Duplex Stainless Steels '94 - Paper K4*. 1994. Glasgow, Scotland: TWI.
51. Sentance, P., *Conf. proc. Duplex Stainless Steels' 91.* Beaune, Les editions de physique, 1991. **2**: p. 895-903.
52. Beeson, D.L. *Conf. Proc. Corrosion Resistant Alloys*. 1995. Kuala Lumpur, Malaysia: Institute of Engineers Malaysia.
53. Punter, A., *Sem proc Aspects of welding duplex stainless steel UNS S31803*. 1986, AB Sandvik Steel: London, UK.
54. Fukai, Y., *The Metal-Hydrogen System - Basic Bulk Properties*. Science. Vol. 261. 1993. 1063-1064.
55. Fukai, Y. and H. Sugimoto, *Diffusion of hydrogen in metals.* Advances in Physics, 1985. **34**(2): p. 263-326.
56. Olden, V., C. Thaulow, and R. Johnsen, *Modelling of hydrogen diffusion and hydrogen induced cracking in supermartensitic and duplex stainless steels.* Materials & Design, 2008. **29**(10): p. 1934-1948.
57. Owczarek, E. and T. Zakroczymski, *Hydrogen transport in a duplex stainless steel.* Acta Materialia, 2000. **48**(12): p. 3059-3070.

58. Turnbull, A. and R.B. Hutchings, *Analysis of Hydrogen-Atom Transport in a 2-Phase Alloy.* Materials Science and Engineering a-Structural Materials Properties Microstructure and Processing, 1994. **177**(1-2): p. 161-171.
59. Turnbull, A., *Perspectives on hydrogen uptake, diffusion and trapping.* International Journal of Hydrogen Energy, 2015. **40**(47): p. 16961-16970.
60. King, H.W. *Structure of the pure metals*. in *Physical Metallurgy*. 1965. North-Holland Publishing Company, Amsterdam.
61. Śmiałowski, M., *Hydrogen in steels*. 1962, Pergamon Press, Oxford.
62. Barnoush, A., *Hydrogen embrittlement, revisited by in situ electrochemical nanoindentation*, in *NT - Materialwissenschaft und Werkstofftechnik*. 2008, Saarland University: Saarbruecken, Germany. p. 288.
63. Robinson, S.L., et al., *The Effects of Current-Density and Recombination Poisons on Electrochemical Charging of Deuterium into Austenite.* Journal of the Electrochemical Society, 1987. **134**(8B): p. C424-C424.
64. Turnbull, A., E. Lembach-Beylegaard, and R. Hutchings. *Hydrogen transport in duplex stainless steels*. in *Proc. Duplex Stainless Steels*. 1994.
65. turnbull, A., *Factors Affecting the Reliability of Hydrogen Permeation Measurments.* Materials Science Forum, 1995. **192-194**: p. 63-78.
66. Zakroczymski, T. and E. Owczarek, *Electrochemical investigation of hydrogen absorption in a duplex stainless steel.* Acta Materialia, 2002. **50**(10): p. 2701-2713.
67. Dadfarnia, M., et al., *Recent advances on hydrogen embrittlement of structural materials.* International Journal of Fracture, 2015.
68. Dadfarnia, M., et al., *Recent Advances in the Study of Structural Materials Compatibility with Hydrogen.* Advanced Materials, 2010. **22**(10): p. 1128-1135.
69. Hua, Z., et al., *The finding of crystallographic orientation dependence of hydrogen diffusion in austenitic stainless steel by scanning Kelvin probe force microscopy.* Scripta Materialia, 2017. **131**: p. 47-50.
70. Lynch, S.P. *Progress towards understanding mechanisms of hydrogen embrittlement and stress corrosion cracking*. in *CORROSION 2007*. 2007. NACE International.
71. Ichitani, K. and M. Kanno, *Visualization of hydrogen diffusion in steels by high sensitivity hydrogen microprint technique.* Science and Technology of Advanced Materials, 2003. **4**(6): p. 545-551.
72. Tanaka, T., K. Kawakami, and S.-i. Hayashi, *Visualization of deuterium flux and grain boundary diffusion in duplex stainless steel and Fe-30 % Ni alloy, using secondary ion mass spectrometry equipped with a Ga focused ion beam.* Journal of Materials Science, 2014. **49**(11): p. 3928-3935.

73. Yazdipour, N., et al., *2D modelling of the effect of grain size on hydrogen diffusion in X70 steel.* Computational Materials Science, 2012. **56**: p. 49-57.
74. Oudriss, A., et al., *Grain size and grain-boundary effects on diffusion and trapping of hydrogen in pure nickel.* Acta Materialia, 2012. **60**(19): p. 6814-6828.
75. Mine, Y., K. Tachibana, and Z. Horita, *Grain-boundary diffusion and precipitate trapping of hydrogen in ultrafine-grained austenitic stainless steels processed by high-pressure torsion.* Materials Science and Engineering a-Structural Materials Properties Microstructure and Processing, 2011. **528**(28): p. 8100-8105.
76. Bastien, P. and P. Azou. *Effect of hydrogen on the deformation and fracture of iron and steel in simple tension*. in *First World Metallurgical Congress*. 1951.
77. Tien, J.K., et al., *Hydrogen Transport by Dislocations.* Metallurgical Transactions a-Physical Metallurgy and Materials Science, 1976. **7**(6): p. 821-829.
78. Robertson, I.M., *The effect of hydrogen on dislocation dynamics.* Engineering Fracture Mechanics, 2001. **68**(6): p. 671-692.
79. Ferreira, P.J., I.M. Robertson, and H.K. Birnbaum, *Hydrogen effects on the interaction between dislocations.* Acta Materialia, 1998. **46**(5): p. 1749-1757.
80. Brass, A.M. and C. J., *Influence of deformation on the hydrogen behavior in iron and nickel base alloys: a review of experimental data.* Materials Science and Engineering: A, 1998. **242**: p. 210-221.
81. McNabb, A. and P. Foster, *A new analysis of the diffusion of hydrogen in iron and ferritic steels.* Trans. Metall. Soc. AIME, 1963. **227**(3): p. 618-627.
82. Koyama, M., et al., *Recent progress in microstructural hydrogen mapping in steels: quantification, kinetic analysis, and multi-scale characterisation.* Materials Science and Technology, 2017: p. 1-16.
83. Song, E.J., *Hydrogen Desorption in Steels*, in *Graduate Institute of Ferrous Technology*. 2015, Pohang University of Science and Technology. p. 106.
84. Seita, M., et al., *The dual role of coherent twin boundaries in hydrogen embrittlement.* Nature communications, 2015. **6**: p. 6.
85. Shipilov, S.A., *Catastrophic failures due to environment-assisted cracking of metals: Case histories*. Environmental Degradation of Materials and Corrosion Control in Metals, ed. M. Elboujdaini and E. Ghali. 1999, Montreal: Canadian Inst Mining, Metallurgy and Petroleum. 225-241.
86. Hirth, J.P., *Effects of Hydrogen on the Properties of Iron and Steel.* Metallurgical Transactions a-Physical Metallurgy and Materials Science, 1980. **11**(6): p. 861-890.

87. Oriani, R.A., *Mechanistic Theory of Hydrogen Embrittlement of Steels.* Berichte Der Bunsen-Gesellschaft Fur Physikalische Chemie, 1972. **76**(8): p. 848-857.
88. Birnbaum, H.K. and P. Sofronis, *Hydrogen-Enhanced Localized Plasticity - a Mechanism for Hydrogen-Related Fracture.* Materials Science and Engineering a-Structural Materials Properties Microstructure and Processing, 1994. **176**(1-2): p. 191-202.
89. Lufrano, J., P. Sofronis, and H.K. Birnbaum, *Modeling of hydrogen transport and elastically accommodated hydride formation near a crack tip.* Journal of the Mechanics and Physics of Solids, 1996. **44**(2): p. 179-205.
90. Oudriss, A., et al., *Meso-scale anisotropic hydrogen segregation near grain-boundaries in polycrystalline nickel characterized by EBSD/SIMS.* Materials Letters, 2016. **165**: p. 217-222.
91. Furtado, J. and F. Barbier. *Hydrogen Embrittlement-Related Issues and Needs in the Hydrogen Value Chain*. in *International Hydrogen Conference (IHC 2012)*. 2014. ASME Press.
92. Gangloff, R.P. and B.P. Somerday, *Gaseous Hydrogen Embrittlement of Materials in Energy Technologies, Vol 2: Mechanisms, Modelling and Future Developments*. Gaseous Hydrogen Embrittlement of Materials in Energy Technologies, Vol 2: Mechanisms, Modelling and Future Developments, ed. R.P. Gangloff and B.P. Somerday. 2012, Cambridge: Woodhead Publ Ltd. 1-500.
93. Gerberich, W., *Gaseous hydrogen embrittlement of materials in energy technologies*, R.P. Gangloff and B. Somerday, Editors. 2012, Woodhead Publishing Limited, Cambridge, UK: Cambridge, UK.
94. Troiano, A.R., *The role of hydrogen and other interstitials in the mechanical behavior of metals.* Transactions of the ASM, 1960. **53**: p. 54-80.
95. John, C.S. and W.W. Gerberich, *The effect of loading mode on hydrogen embrittlement.* Metallurgical Transactions, 1973. **4**(2): p. 589-594.
96. Oriani, R.A., *Whitney Award Lecture 1987 - Hydrogen - the Versatile Embrittler.* Corrosion, 1987. **43**(7): p. 390-397.
97. Tabata, T. and H.K. Birnbaum, *Direct observations of hydrogen enhanced crack propagation in iron.* Scripta Metallurgica, 1984. **18**(3): p. 231-236.
98. Robertson, I.M. and H.K. Birnbaum, *An HVEM study of hydrogen effects on the deformation and fracture of nickel.* Acta Metallurgica, 1986. **34**(3): p. 353-366.
99. Robertson, I.M., H.K. Birnbaum, and P. Sofronis, *Hydrogen effects on plasticity.* Dislocations in solids, 2009. **15**: p. 249-293.

100. Beachem, C.D., *New Model for Hydrogen-Assisted Cracking (Hydrogen Embrittlement).* Metallurgical Transactions, 1972. **3**(2): p. 437-451.
101. Zapffe, C. and C. Sims, *Hydrogen Embrittlement, Internal Stress and Defects in Steel.* Trans. AIME, 1941. **145**(1941): p. 225-261.
102. Tetelman, A.S. and W.D. Robertson, *Direct observation and analysis of crack propagation in iron-3% silicon single crystals.* Acta Metallurgica, 1963. **11**(5): p. 415-426.
103. Petch, N.J., *The lowering of fracture-stress due to surface adsorption.* Philosophical magazine, 1956. **1**(4): p. 331-337.
104. Tromans, D., *On surface energy and the hydrogen embrittlement of iron and steels.* Acta metallurgica et materialia, 1994. **42**(6): p. 2043-2049.
105. Lynch, S.P., *Hydrogen embrittlement phenomena and mechanisms.* Corrosion Reviews, 2012.
106. Nagumo, M., *Function of hydrogen in embrittlement of high-strength steels.* ISIJ international, 2001. **41**(6): p. 590-598.
107. Song, J. and W.A. Curtin, *A nanoscale mechanism of hydrogen embrittlement in metals.* Acta Materialia, 2011. **59**(4): p. 1557-1569.
108. Song, J. and W.A. Curtin, *Atomic mechanism and prediction of hydrogen embrittlement in iron.* Nature Materials, 2013. **12**: p. 145-151.
109. Westlake, D.G., *The habit planes of zirconium hydride in zirconium and zircaloy.* Journal of Nuclear Materials, 1968. **26**(2): p. 208-216.
110. Birnbaum, H.K., *Mechanical Properties of Metal Hydrides.* Journal of the Less Common Metals, 1984. **104**(1): p. 31-41.
111. Eliezer, D., et al., *The influence of austenite stability on the hydrogen embrittlement and stress-corrosion cracking of stainless steel.* Metallurgical and Materials Transactions A, 1979. **10**(7): p. 935-941.
112. Hobson, J.D. and J. Hewitt, *The effect of hydrogen on the tensile properties of steel.* Journal of the Iron and Steel Institute, 1953. **173**(2): p. 131-140.
113. Kirchheim, R., *On the solute-defect interaction in the framework of a defactant concept.* International Journal of Materials Research, 2009. **100**(4): p. 483-487.
114. Lynch, S.P., *Environmentally Assisted Cracking - Overview of Evidence for an Adsorption-Induced Localized-Slip Process.* Acta Metallurgica, 1988. **36**(10): p. 2639-2661.
115. Lynch, S.P., *Mechanisms of hydrogen assisted cracking - A review.* Hydrogen Effects on Material Behavior and Corrosion Deformation Interactions, 2003: p. 449-466.
116. Clum, J.A., *The Role of Hydrogen in Dislocation Generation in Iron Alloys.* Scripta Metallurgica, 1975. **9**: p. 51-58.

117. Nelson, H.G., *Hydrogen Embrittlement*. Treatise on Materials Science and Technology, ed. B. C.L. and B. S.K. Vol. 25. 1983, New York: Academic Press.
118. Sirois, E. and H.K. Birnbaum, *Effects of hydrogen and carbon on thermally activated deformation of nickel. .* Parkins Symposium on Fundamentals Aspects of Stress Corrosion Cracking, The Minerals, Metals and Materials Society, 1992: p. 173-190.
119. Griesche, A., et al., *Three-dimensional imaging of hydrogen blister in iron with neutron tomography.* Acta Materialia, 2014. **78**: p. 14-22.
120. Tiegel, M.C., et al., *Crack and blister initiation and growth in purified iron due to hydrogen loading.* Acta Materialia, 2016. **115**: p. 24-34.
121. Lublinska, K., A. Szummer, and K.J. Kurzydlowski, *Hydrogen Induced Microtwins in Cr Alloyed Ferrite*, in *Carbon Nanomaterials in Clean Energy Hydrogen Systems*, B. Baranowski, et al., Editors. 2008. p. 757-764.
122. Luu, W.C., P.W. Liu, and J.K. Wu, *Hydrogen transport and degradation of a commercial duplex stainless steel.* Corrosion Science, 2002. **44**(8): p. 1783-1791.
123. Marchi, C.S., et al., *Mechanical properties of super duplex stainless steel 2507 after gas phase thermal precharging with hydrogen.* Metallurgical and Materials Transactions a-Physical Metallurgy and Materials Science, 2007. **38a**(11): p. 2763-2775.
124. Han, G., et al., *Hydrogen environment embrittlement of austenitic stainless steels at low temperatures (study on low temperature materials used in WE-NET 7).* Hydrogen Energy Progress Xii, Vols 1-3, 1998: p. 1863-1872.
125. Uhlig, H.H. *An Evaluaton of Stress Corrosion Cracking Mechanisms*. in *International Conference on Fundamental Aspects of Stress Corrosion Cracking*. 1967. Ohio State University, US.
126. Tarzimoghadam, Z., et al., *Multi-scale and spatially resolved hydrogen mapping in a Ni-Nb model alloy reveals the role of the δ phase in hydrogen embrittlement of alloy 718.* Acta Materialia, 2016. **109**: p. 69-81.
127. Rhode, M., et al., *Effect of hydrogen on mechanical properties of heat affected zone of a reactor pressure vessel steel grade.* Welding in the World, 2016. **60**(4): p. 623-638.
128. Straub, F., et al. *In-situ Detection of Deuterium in Duplex Stainless Steels by Time-of-Flight Secondary Ion Mass Spectrometry (TOF-SIMS)*. in *International Hydrogen Conference (IHC 2012)*. 2012. ASME press.
129. Saintier, N., et al., *Analyses of hydrogen distribution around fatigue crack on type 304 stainless steel using secondary ion mass spectrometry.* International Journal of Hydrogen Energy, 2011. **36**(14): p. 8630-8640.

130. Marchi, C.S., B.P. Somerday, and S.L. Robinson, *Permeability, solubility and diffusivity of hydrogen isotopes in stainless steels at high gas pressures.* International Journal of Hydrogen Energy, 2007. **32**(1): p. 100-116.
131. Louthan, M.R. and R.G. Derrick, *Permeability of nickel to high pressure hydrogen isotopes.* Scripta Metallurgica, 1976. **10**: p. 53-55.
132. Quick, N.R. and H.H. Johnson, *Permeation and Diffusion of Hydrogen and Deuterium in 310 Stainless-Steel, 472-K to 779-K.* Metallurgical Transactions a-Physical Metallurgy and Materials Science, 1979. **10**(1): p. 67-70.
133. Swansiger, W.A. and R. Bastasz, *Tritium and deuterium permeation in stainless steels: influence of thin oxide films.* Journal of Nuclear Materials, 1979. **85-86**: p. 335-339.
134. Forcey, K.S., et al., *Hydrogen transport and solubility in 316L and 1.4914 steels for fusion reactor applications.* journal of Nuclear Materials, 1988. **160**: p. 117-124.
135. Shiraishi, T., et al., *Permeation of multi-component hydrogen isotopes through austenitic stainless steels.* Journal of Nuclear Materials, 1999. **273**: p. 60-65.
136. Voelkl, J. and G. Alefeld, *Hydrogen diffusion in metals*, in *Diffusion in solids: recent developments: Materials science and technology*, A.S. Nowick and J.J. Burton, Editors. 1975, New York: Academic Press: New York.
137. Kumnick, A.J. and H.H. Johnson, *Hydrogen and deuterium in iron, 9-73°C.* Acta Metallurgica, 1977. **25**(8): p. 891-895.
138. Raczynski, W., *Permeability, diffusivity and solubility of hydrogen and deuterium in pure iron at 10 to 60°C* Physica Status Solidi (a), 1978. **48**(1): p. 27-30.
139. Standardization, I.-I.O.f., *Determination of hydrogen content in arc weld metal*, in *ISO 3690 - Welding and allied processes*. 2012.
140. Park, Y.D., I.S. Maroef, and D.L. Olson, *Retained austenite as a hydrogen trap in steel welds.* Welding Journal, 2002. **81**(2): p. 27s-35s.
141. Hassel, A.W., et al., *Methodology of hydrogen measurements in coated steels*. 2013, European Commission: Brussels. p. 155.
142. Devanathan, M.A.V. and Z. Stachurski, *Adsorption and Diffusion of Electrolytic Hydrogein in Palladium.* Proceedings of the Royal Society of London Series a-Mathematical and Physical Sciences, 1962. **270**(1340): p. 90-102.
143. Lee, T.C., et al., *An environmental cell transmission electron microscope.* Review of scientific instruments, 1991. **62**(6): p. 1438-1444.

144. Bond, G.M., I.M. Robertson, and H.K. Birnbaum, *On the determination of the hydrogen fugacity in an environmental cell tem facility.* Scripta metallurgica, 1986. **20**(5): p. 653-658.
145. Hajilou, T., et al., *In situ electrochemical microcantilever bending test: A new insight into hydrogen enhanced cracking.* Scripta Materialia, 2017. **132**: p. 17-21.
146. Barnoush, A., M. Zamanzade, and H. Vehoff, *Direct observation of hydrogen-enhanced plasticity in super duplex stainless steel by means of in situ electrochemical methods.* Scripta Materialia, 2010. **62**(5): p. 242-245.
147. Chen, Y.S., et al., *Direct observation of individual hydrogen atoms at trapping sites in a ferritic steel.* Science, 2017. **355**(6330): p. 1196-1199.
148. Choo, W.Y. and J.Y. Lee, *Hydrogen trapping phenomena in carbon steel.* Journal of materials Science, 1982. **17**(7): p. 1930-1938.
149. Eliezer, D. and T. Boellinghaus, *Hydrogen Trapping Mechanisms in Structural Materials.* Effects of Hydrogen on Materials, 2009: p. 438-+.
150. Sekiba, D., et al., *Development of micro-beam NRA for hydrogen mapping: Observation of fatigue-fractured surface of glassy alloys.* Nuclear Instruments & Methods in Physics Research Section B-Beam Interactions with Materials and Atoms, 2011. **269**(7): p. 627-631.
151. Fukutani, K., *Below-surface behavior of hydrogen studied by nuclear reaction analysis.* Current opinion in solid state and materials science, 2002. **6**(2): p. 153-161.
152. Takahashi, J., K. Kawakami, and T. Tarui, *Direct observation of hydrogen-trapping sites in vanadium carbide precipitation steel by atom probe tomography.* Scripta Materialia, 2012. **67**(2): p. 213-216.
153. Momotani, Y., et al., *Hydrogen embrittlement behavior at different strain rates in low-carbon martensitic steel*, in *Materials Today: Proceedings 2*. 2015. p. 735-738.
154. Haley, D., et al., *Atomprobe tomography observation of hydrogen in high-Mn steel and silver charged via an electrolytic route.* international Journal of Hydrogen Energy, 2014. **39**(23): p. 12221-12229.
155. Takahashi, J., et al., *The first direct observation of hydrogen trapping sites in TiC precipitation-hardening steel through atom probe tomography.* Scripta Materialia, 2010. **63**(3): p. 261-264.
156. Unger, W.E.S. and V.D. Hodoroaba, *Surface Chemical Analysis at the Micro-and NanoScale*. 2013, Berlin: Springer.
157. Senoner, M. and W.E.S. Unger, *SIMS imaging of the nanoworld: applications in science and technology.* Journal of Analytical Atomic Spectrometry, 2012. **27**(7): p. 1050-1068.

158. Izawa, C., *Extended TOF-SIMS analysis on low-nickel austenitic stainless steels: The influence of oxide layers on hydrogen embrittlement*, in *Georg-August University School of Science (GAUSS)*. 2015, Georg-August-Universität Göttingen: Universität Göttingen. p. 190.
159. Vickerman, J.C. and D. Briggs, *TOF SIMS: Surface Analysis by Mass Spectrometry*. 2001, IM Publications; SurfaceSpectra Ltd.: Manchester, UK. p. 789.
160. Sodhi, R.N.S., *Time-of-flight secondary ion mass spectrometry (TOF-SIMS): versatility in chemical and imaging surface analysis.* Analyst, 2004. **129**(6): p. 483-487.
161. Holzlechner, G., et al., *A novel ToF-SIMS operation mode for improved accuracy and lateral resolution of oxygen isotope measurements on oxides.* Journal of Analytical Atomic Spectrometry, 2013. **28**(7): p. 1080-1089.
162. Kubicek, M., et al., *A novel ToF-SIMS operation mode for sub 100 nm lateral resolution: Application and performance.* Applied Surface Science, 2014. **289**: p. 407-416.
163. Fukushima, H. and H.K. Birnbaum, *Scanning Auger and Sims Studies of H, S, and Cl-Segregation at Grain-Boundaries in Nickel.* Journal of Metals, 1982. **34**(8): p. 41-41.
164. Fukushima, H. and H.K. Birnbaum, *High-Resolution Saes and Sims Studies of Grain-Boundary Segregation of S and Cl in Ni.* Scripta Metallurgica, 1982. **16**(6): p. 753-757.
165. Fukushima, H. and H.K. Birnbaum, *Surface and Grain-Boundary Segregation of Deuterium in Nickel.* Acta Metallurgica, 1984. **32**(6): p. 851-859.
166. Ladna, B., C.M. Loxton, and H.K. Birnbaum, *Surface Segregation of Deuterium in A Nb-V Alloy.* Acta Metallurgica, 1986. **34**(5): p. 899-904.
167. Oltra, R. and C. Bouillot, *Experimental investigation of the role of hydrogen in stress corrosion cracking of duplex stainless steels.* Hydrogen Transport and Cracking in Metals, 1994: p. 17-26.
168. Izawa, C., et al., *SIMS analysis on austenitic stainless steel: The influence of type of oxide surface layer on hydrogen embrittlement.* Journal of Alloys and Compounds, 2013. **580**: p. S13-S17.
169. Straub, F., et al., *Imaging the microstructure of duplex stainless steel samples with TOF-SIMS.* Surface and Interface Analysis, 2010. **42**(6-7): p. 739-742.
170. Frank, R.C., J.E. Baker, and C.J. Altstetter, *A Sims Study of the Diffusion and Trapping of Deuterium in 302 Stainless-Steel.* Metallurgical Transactions a-Physical Metallurgy and Materials Science, 1982. **13**(4): p. 581-584.

171. Gao, H., et al., *Analysis of Crack-Tip Hydrogen Distribution under I/Ii Mixed-Mode Loads.* Fatigue & Fracture of Engineering Materials & Structures, 1994. **17**(10): p. 1213-1220.
172. Takai, K., J. Seki, and Y. Homma, *Observation of Trapping Sites of Hydrogen and Deuterium in High-Strength Steels by Using Secondary-Ion Mass-Spectrometry.* Materials Transactions Jim, 1995. **36**(9): p. 1134-1139.
173. Takai, K., et al., *Visualization of the hydrogen desorption process from ferrite, pearlite, and graphite by secondary ion mass spectrometry.* Metallurgical and Materials Transactions a-Physical Metallurgy and Materials Science, 2002. **33**(8): p. 2659-2665.
174. Kawamoto, K., et al., *Investigation of Local Hydrogen Distribution Around Fatigue Crack Tip of a Type 304 Stainless Steel with Secondary Ion Mass Spectrometry and Hydrogen Micro-Print Technique.* Journal of Solid Mechanics and Materials Engineering, 2009. **3**(6): p. 898-909.
175. Awane, T., et al., *Highly Sensitive Secondary Ion Mass Spectrometric Analysis of Time Variation of Hydrogen Spatial Distribution in Austenitic Stainless Steel at Room Temperature in Vacuum.* International Journal of Hydrogen Energy, 2014. **39**(2): p. 1164-1172.
176. Katsuta, H. and K. Furukawa, *Hydrogen and Deuterium Transport through Type-304 Stainless-Steel at Elevated-Temperatures.* Journal of Nuclear Science and Technology, 1981. **18**(2): p. 143-151.
177. Sobol, O., et al., *Real Time Imaging of Deuterium in a Duplex Stainless Steel Microstructure by Time-of-Flight SIMS.* Scientific Reports, 2016. **6**(19929): p. 1-7.
178. Sobol, O., et al., *Time-of-Flight Secondary Ion Mass Spectrometry (ToF-SIMS) imaging of deuterium assisted cracking in a 2205 Duplex stainless steel microstructure.* Materials Science and Engineering A - In press, 2016.
179. Sobol, O., et al., *Novel approach to image hydrogen distribution and related phase transformation in duplex stainless steels at the sub-micron scale.* international Journal of Hydrogen Energy, 2017. **42**(39): p. 25114-25120.
180. Straif, C.J., *The interaction of Bi cluster ions with molecular compounds*, in *Fakultät für Technische Chemie - Institut für Chemische Technologien und Analytik*. 2009, Technischen Universität Wien.
181. Storms, H.A., K.F. Brown, and J.D. Stein, *Evaluation of a cesium positive ion source for secondary ion mass spectrometry.* Analytical Chemistry, 1977. **49**(13): p. 2023-2030.
182. www.iontof.com.
183. www.piezosystem.com. *PiezosystemJena: incredibly precise*. Available from: www.piezosystem.com.

184. *ASM Metals HandBook Volume 8 - Mechanical Testing and Evaluation*. ASM Metals Handbook - Desk Edition. Vol. 8. 2000: ASM International.
185. Schwartz, A.J., et al., *Electron backscatter diffraction in materials science*. Vol. 2. 2009, Berlin: Springer Verlag.
186. Sieurin, H. and R. Sandstrom, *Fracture toughness of a welded duplex stainless steel.* Engineering Fracture Mechanics, 2006. **73**(4): p. 377-390.
187. Sieurin, H., R. Sandstrom, and E.M. Westin, *Fracture Toughness of the Lean Duplex Stainless Steel LDX 2101.* METALLURGICAL AND MATERIALS TRANSACTIONS A, 2006. **37a**: p. 2975-2981.
188. Benninghoven, A., *Surface analysis by secondary ion mass spectrometry (SIMS).* Surface Science, 1994. **299**: p. 246-260.
189. Lee, J., et al., *Multivariate image analysis strategies for ToF-SIMS images with topography.* Surface and Interface Analysis, 2009. **41**(8): p. 653-665.
190. Graham, D.J. and D.G. Castner, *Multivariate analysis of ToF-SIMS data from multicomponent systems: the why, when, and how.* Biointerphases, 2012. **7**(1): p. 10.
191. Lohninger, H. and J. Ofner, *Multisensor hyperspectral imaging as a versatile tool for image-based chemical structure determination.* SPECTROSCOPY EUROPE 2014. **26**(5): p. 5.
192. Oltra, R., C. Bouillot, and T. Magnin, *Localized hydrogen cracking in the austenitic phase of a duplex stainless steel.* Scripta Materialia, 1996. **35**(9): p. 1101-1105.
193. Lublinska, K., A. Szummer, and K.J. Kurzydlowski. *Hydrogen Induced Cracking in Duplex 00H18N5M3S Stainless Steel*. in *17th European Conference on Fracture*. 2008. Brno, Czech Republic.
194. Glowacka, A. and W.A. Swiatnicki, *Effect of hydrogen charging on the microstructure of duplex stainless steel.* Journal of Alloys and Compounds, 2003. **356**: p. 701-704.
195. Szummer, A., E. Jezierska, and K. Lublinska, *Hydrogen surface effects in ferritic stainless steels.* Journal of Alloys and Compounds, 1999. **293**: p. 356-360.
196. Michalska, J. *Corrosion induced by cathodic hydrogen in 2205 duplex stainless steel*. in *IOP Conf. Series: Materials Science and Engineering*. 2011. IOP Publishing Ltd.
197. Minkovitz, E. and D. Eliezer, *TEM Study on the Formation of Microcracks in Connection with Alpha'-Martensite.* Journal of Materials Science Letters, 1982. **1**(5): p. 192-194.
198. Glowacka, A., et al., *Hydrogen induced phase transformations in austenitic-ferritic steel*, in *Materials in Transition, Proceedings*, L. Dobrzynski and K. Perzynska, Editors. 2006. p. 133-139.

199. Rozenak, P., *Stress Induce Martensitic Transformations in Hydrogen Embrittlement of Austenitic Stainless Steels.* Metallurgical and Materials Transactions a-Physical Metallurgy and Materials Science, 2014. **45A**(1): p. 162-178.
200. Mente, T. and T. Boellinghaus, *Numerical investigations on hydrogen-assisted cracking in duplex stainless steel microstructures*, in *Cracking Phenomena in Welds IV*, T. Boellinghaus, J.C. Lippold, and C.E. Cross, Editors. 2016, Springer. p. 329-359.
201. Yang, Q. and J.L. Luo, *Martensite transformation and surface cracking of hydrogen charged and outgassed type 304 stainless steel.* Materials Science and Engineering a-Structural Materials Properties Microstructure and Processing, 2000. **288**(1): p. 75-83.
202. Luo, H., et al., *Characterization of hydrogen charging of 2205 duplex stainless steel and its correlation with hydrogen-induced cracking.* Materials and Corrosion-Werkstoffe Und Korrosion, 2013. **64**(1): p. 26-33.
203. Olden, V., L. Jemblie, and R. Johnsen. *FE Simulation of Hydrogen Diffusion in a Duplex Stainless Steel-Influence of Phase Shape and Size and Embedded Defects*. in *The Twenty-third International Offshore and Polar Engineering Conference*. 2013. International Society of Offshore and Polar Engineers.
204. Zakroczymski, T., A. Glowacka, and W. Swiatnicki, *Effect of hydrogen concentration on the embrittlement of a duplex stainless steel.* Corrosion Science, 2005. **47**(6): p. 1403-1414.
205. Sobol, O., et al., *Time-of-Flight Secondary Ion Mass Spectrometry (ToF-SIMS) imaging of deuterium assisted cracking in a 2205 duplex stainless steel microstructure.* Materials Science and Engineering a-Structural Materials Properties Microstructure and Processing, 2016. **676**: p. 271-277.
206. Silverstein, R. and D. Eliezer, *Hydrogen trapping mechanism of different duplex stainless steels alloys.* Journal of Alloys and Compounds, 2015. **644**: p. 280-286.
207. Au, J. and H.K. Birnbaum, *On the Formation of Interstitial - Hydrogen Clusters in Iron.* Scripta Metallurgica, 1981. **15**(8): p. 941-943.
208. Hannula, S.P., H. Hanninen, and S. Tahtinen, *Influence of Nitrogen Alloying on Hydrogen Embrittlement in Aisi 304-Type Stainless-Steels.* Metallurgical Transactions a-Physical Metallurgy and Materials Science, 1984. **15**(12): p. 2205-2211.
209. Yang, L., et al., *Performance of a microfluidic device for in situ ToF-SIMS analysis of selected organic molecules at aqueous surfaces.* Analytical Methods, 2013. **5**(10): p. 2515-2522.

210. Lufrano, J. and P. Sofronis, *Enhanced hydrogen concentrations ahead of rounded notches and cracks - competition between plastic strain and hydrostatic stress.* Acta Materialia, 1998. **46**(5): p. 1519-1526.
211. Lufrano, J., P. Sofronis, and D. Symons, *Hydrogen transport and large strain elastoplasticity near a notch in alloy X-750.* Engineering Fracture Mechanics, 1998. **59**(6): p. 827-845.
212. Yokobori, A.T., et al., *Numerical analysis on hydrogen diffusion and concentration in solid with emission around the crack tip.* Engineering Fracture Mechanics, 1996. **55**(1): p. 47-60.
213. Boellinghaus, T. and H. Hoffmeister, *Numerical model for hydrogen-assisted cracking.* Corrosion, 2000. **56**(6): p. 611-622.
214. Lothongkum, G., et al., *Effect of nitrogen on corrosion behavior of 28Cr-7Ni duplex and microduplex stainless steels in air-saturated 3.5 wt% NaCl solution.* Corrosion Science, 2006. **48**(1): p. 137-153.
215. Sieurin, H., *Fracture toughness properties of duplex stainless steels*, in *Materials Science and Engineering, Royal Institute of Technology*. 2006, Royal Institute of Technology: Stockholm, Sweden. p. 46.

List of Publications

Sobol, Oded et al. "Novel approach to image hydrogen distribution and related phase transformation in duplex stainless steels at the sub-micron scale" Int. J. Hydrogen Energy, 2017, 25114-25120.

Sobol, Oded et al. "High Resolution ToF-SIMS Imaging of Deuterium Permeation and Cracking in Duplex Stainless Steels" International Hydrogen Conference (IHC 2016), Eds B. Somerday & P. sofronis, ASME Press, 2017, 407-415.

Silverstein, Ravit et al. "Hydrogen behavior in SAF 2205 duplex stainless steel" J. Alloys and Compounds, 2017, 2689-2695.

Sobol, Oded et al. "Time-of-Flight Secondary Ion Mass Spectrometry (ToFSIMS) imaging of deuterium assisted cracking in a 2205 duplex stainless steel micro-structure" J. Mat. Science and engineering, 2016, 271-277.

Sobol, Oded et al. "Real Time Imaging of Deuterium in a Duplex Stainless Steel Microstructure by Time-of-Flight SIMS." Scientific reports 6 (2016).

Sobol, Oded et al. "First use of data fusion and multivariate analysis of ToF-SIMS and SEM image data for studying deuterium-assisted degradation processes in duplex steels." Surface and Interface Analysis (2016).

Holzlechner, Gerald et al. "Imaging ToF-SIMS as a Chemical Metrology Tool to Support Material and Analytical Science."Materials for Energy Infrastructure. Springer Singapore, 2016. 63-72.

Sobol, Oded et al. "Addressing a “Black Box” of Bottom-Up Synthesis: Revealing the Structures of Growing Colloidal-Nanocrystal Nuclei." Inorganic chemistry 54.22 (2015): 10521-10523.

Foxman, Zvi et al. "Microstructural Evolution of Cr-Rich ODS Steels as a Function of Heat Treatment at 475° C." J. Metallography, Microstructure, and Analysis, 2012, 158-164.

Curriculum Vitae

Name: Sobol, Oded

Born: 27th of November 1983 in Kiryat Tivon, Israel

Nationality: Israeli

Education:

09/1994 – 06/2001	Ort-Grinberg middle and high school in Kiryat Tivon, Israel
10/2007 – 09/2011	Bachelor of Science in materials engineering in Ben-Gurion University in Beer-Sheva, Israel
10/2011 – 12/2013	Master of Science in materials engineering in Ben-Gurion University in Beer-Sheva, Israel
02/2014 – 01/2018	Federal Institute for Materials Research and Testing in Berlin, Germany

Other:

04/2002 – 08/2007	Military service
09/2011 – 10/2013	Teaching assistant at the department of material engineering, Ben-Gurion University